

Vector-boson scattering - Impact of a concrete new-physics model versus its EFT realization

Master's Thesis of

Jannis Lang

at the Department of Physics
Institute for Theoretical Physics (ITP)

Reviewer: Prof. D. Zeppenfeld
Second reviewer: Prof. M. M. Mühlleitner
Advisor: Dr. S. Liebler
Second advisor: M.Sc. H. Schäfer-Siebert

16th March 2019 – 16th March 2020

This electronic version for the ITP website has been corrected for minor mistakes and therefore does not fully resemble the exam copy.

Last modification date: **July 16, 2020**

I declare that I have developed and written the enclosed thesis completely by myself, and have not used sources or means without declaration in the text.

Karlsruhe, 16th March 2020

.....
(Jannis Lang)

Ich versichere wahrheitsgemäß, die Arbeit selbstständig verfasst, alle benutzten Hilfsmittel vollständig und genau angegeben und alles kenntlich gemacht zu haben, was aus Arbeiten anderer unverändert oder mit Abänderungen entnommen wurde sowie die Satzung des KIT zur Sicherung guter wissenschaftlicher Praxis in der jeweils gültigen Fassung beachtet zu haben.

Karlsruhe, 16. März 2020

.....
(Jannis Lang)

Abstract

After 10 years of data taking at the Large Hadron Collider and the discovery of a Higgs boson in 2012, vector-boson scattering is more than ever a promising class of processes for the search of effects from physics beyond the Standard Model. It is very common to parametrize the effects of new physics in a model independent way using an effective field theory approach.

In this thesis, we construct a complete effective field theory basis including operators up to energy dimension 8 after imposing some simplifying assumptions of the underlying model in order to limit the discussion to the relevant features. We propose a toy-model that includes new fermion and scalar multiplets that transform under a representation of $SU(2)_L$ in the $SU(2)_L$ limit of the Standard Model and derive its effective field theory description by calculating its Wilson coefficients in a low-energy approximation of the one-loop corrections. The one-loop calculation of the toy-model, its effective field theory and several subsets of effective field theory operators are compared in on-shell vector-boson scattering, and the effects are investigated at different levels of the calculation, i.e. at the level of the matrix element, differential and fiducial cross sections. With an approximation of using a finite partial-wave expansion of the new-physics contribution in the dominant helicity amplitudes, the contributions are implemented in VBFNLO. After performing necessary cross checks, VBFNLO is used to predict $W^\pm Z$ and ZZ production processes at a proton-proton collider in the toy-model and its effective field theory realization and a comparison of the results with experimental analysis is carried out. Implications for future studies, both theoretical and experimental, are formulated.

Zusammenfassung

Nachdem über 10 Jahre lang Messungen am Large Hadron Collider durchgeführt wurden und ein Higgs Boson 2012 entdeckt wurde, entwickelt sich Vektor-Boson-Streuung mehr denn je zu einer vielversprechenden Klasse von Prozessen für die Suche nach Physik jenseits des Standard Modells. Üblicherweise wird der Effekt von neuer Physik in einer modelunabhängigen Weise mit der Methode der effektiven Feldtheorie parametrisiert.

In dieser Thesis wird eine komplette Basis der effektiven Feldtheorie einschließlich der Operatoren mit Energiedimension 8 konstruiert, nachdem im Voraus einige vereinfachende Annahmen über das zugrundeliegende Modell getroffen werden. Damit soll die Diskussion auf die relevanten Eigenschaften reduziert werden. Wir beschränken uns weiterhin auf den $SU(2)_L$ Limes des Standard Modells bei unseren Berechnungen. Wir führen ein Toy-Modell ein, welches neue fermionische und skalare Multipletts beinhaltet, die sich unter einer Repräsentation der $SU(2)_L$ transformieren. Die effektive feldtheoretische Beschreibung des Toy-Modells wird aus der Berechnung der Wilson Koeffizienten durch eine Niedrigenergie-Näherung der Einschleifen-Korrekturen bestimmt. Die Einschleifen-Rechnung des Toy-Modells, die davon abgeleitete effektive Feldtheorie und verschiedene Teilmengen der Operatoren der effektiven Feldtheorie werden in Vektor-Boson-Streuung für Bosonen auf der Massenschale verglichen. Die Effekte werden dabei in verschiedenen Ebenen der Rechnung untersucht, z.B. auf der Ebene des Matrix Elements, des differentiellen und des inklusiven Wirkungsquerschnitts. Mit der Näherung des Anteils der neuen Physik in den dominanten Helizitätsamplituden durch eine begrenzte Partialwellenzerlegung werden die Beiträge in VBFNLO implementiert. Nachdem notwendige Überprüfungen durchgeführt werden, wird die Implementation des vollen Toy-Modells und der effektiven feldtheoretischen Beschreibung in VBFNLO genutzt, um Vorhersagen für die $W^\pm Z$ und ZZ Produktion in einem Proton-Proton Collider zu treffen. Ein Vergleich der Resultate mit experimentellen Untersuchungen wird vollzogen. Die Auswirkungen auf zukünftige Studien, sowohl theoretische als auch experimentelle, werden formuliert.

Contents

Abstract	i
Zusammenfassung	iii
1. Introduction	1
2. Quantum field theory and the Standard Model	3
2.1. Quantum field theory basics	3
2.2. The Standard Model and its $SU(2)_L$ limit	7
2.3. One-loop corrections	8
3. Effective field theory	11
3.1. Constructing the effective field theory basis	12
3.1.1. Techniques and strategy	12
3.1.2. Dimension 4 operators	13
3.1.3. Dimension 6 operators	13
3.1.4. Dimension 8 operators	14
3.2. Partial waves and unitarity	17
4. Ultraviolet complete toy-model	23
4.1. One-loop vertex corrections	24
4.2. Renormalization	27
4.3. Matching of Wilson coefficients	30
5. On-shell vector-boson scattering	35
5.1. Process definition	35
5.2. Kinematics	37
5.3. Perturbative counting in the EFT cross-section calculation	38
5.4. On-shell cross section	41
5.5. Angular dependence of the amplitudes	46
5.6. Partial wave analysis	49
5.7. Validity of the $j \leq 2$ partial wave approximation	55
6. Vector-boson scattering at the LHC	61
6.1. VBFNLO and the implementation of the new-physics model	61
6.2. VBFNLO settings	63
6.3. Monte Carlo cross checks	64
6.4. Results for $W^\pm Z$ and ZZ production	67
6.5. Implications for experimental analysis	72

7. Summary and conclusion	79
A. Appendix	81
A.1. One-loop calculations	81
A.1.1. Master integral prescription	81
A.1.2. Passarino-Veltman decomposition	84
A.2. Feynman rules	86
A.3. Identities for the $\mathfrak{su}(2)_L$ algebra	88
A.3.1. Calculation of traces with four $\mathfrak{su}(n)$ generators	91
A.4. Definitions for helicity eigenvectors	92
A.5. VeBoS program	93
A.5.1. Input settings	94
A.5.2. Output	96
A.6. Partial-wave analysis of the concrete scalar model	97
Bibliography	99

1. Introduction

In the last 60 years particle physicists developed a consistent quantum-field theory (QFT) which describes a plethora of experimental phenomena from low to very high energies. With the discovery of a Higgs boson [1, 2] at the Large Hadron Collider (LHC) the last fundamental constituent of the Standard Model of particle physics (SM) likely has been observed by experimental collaborations. Thus, the time has come to engage in precision measurements of various observables and to search for discrepancies to predictions in the SM which emerge from new physics (NP) beyond the SM.

With the current available data of the Large Hadron Collider and the upcoming high-luminosity phase [3], precision experiments of proton-proton collisions reach the next level. This gives us the unique opportunity to gain deeper insight in processes that could not be studied in great detail in the past. Vector-boson scattering (VBS) forms such a promising class of processes and attracts rising interest among particle physicists. It is expected that corrections to the weak-boson couplings, arising from NP contributions, cause sizable deviations from the SM cross section in VBS, even if the underlying models enter at a high energy scale [4, 5]. The common practice is to parametrize those NP contributions with an effective field theory (EFT) approach, which in general introduces a large number of parameters. Hence, current experimental analysis on anomalous couplings described by EFT operators [6, 7] often provide their results based on one single EFT operator at a time. Since any underlying model does not only introduce one single EFT operator, this procedure often does not fit to the expectation of NP models. In addition, any EFT, by definition, is only applicable in a finite region of validity, which is typically unknown if the underlying model is not further specified. Therefore, the aim of the thesis is to compare the impact on VBS of a concrete NP model with its EFT realization. We also study subsets of the derived EFT operators in order to determine the relevant contributions of our underlying model. Finally, we compare with experimental analyses and formulate implications for future investigations.

In Chapter 2 this thesis begins with a review on some necessary principles and techniques of QFT and we give a brief introduction of the SM and its $SU(2)_L$ limit to which we restrict our calculations. In Chapter 3 we discuss the general topic of EFT, and construct a complete basis up to energy dimension 8 which will be used in the effective description of VBS. Additionally, we derive the unitarity bounds which any theory has to fulfill. We introduce our concrete NP model in Chapter 4 and calculate the vertex corrections and associated renormalization in the minimal subtraction (\overline{MS}) scheme. The low-energy approximation of the vertex corrections leads to the matching of the Wilson coefficients of the EFT.

In Chapter 5 we investigate the phenomenology of our NP model and its derived EFT realization in on-shell VBS. After discussing the adequate perturbative counting of the EFT calculation, we compare the cross section predictions and examine angular dependencies of the dominant helicity amplitudes. We determine the first coefficients of the partial-wave

(PW) expansion of the dominant helicity amplitudes, which we verify as an accurate approximation of on-shell VBS. Furthermore, we probe our concrete model for unitarity with the derivation of the dominant eigenvalue of the PW coefficients. In Chapter 6 we use VBFNL0[8–10] for predictions of VBS occurring in proton-proton collisions with the implementation of an approximate version of our model. We perform necessary cross checks for consistency, and investigate the predictions for $W^\pm Z$ and ZZ production with our NP model. Thereafter, we compare our predictions with current experimental analysis and propose implications for future studies. We conclude in Chapter 7.

2. Quantum field theory and the Standard Model

In this chapter we recapitulate the basic concepts and definitions relevant for a quantum field theory (QFT) and in particular for the Standard Model of particle physics (SM). As it is common in theoretical particle physics, all formulas will be presented in natural units throughout this thesis. That means we set the fundamental constants of nature equal to one:

$$\hbar = 1, \quad c = 1, \quad \epsilon_0 = 1. \quad (2.1)$$

In this way all quantities which stay dimensionfull will be expressed in terms of energy, e.g. time and length are measured in inverse units of energy. When comparing predicted observables with actual measurement we only have to multiply by powers of the fundamental constants in SI units which are needed to get the right unit dimension.

2.1. Quantum field theory basics

In QFT, a specific model living in d dimensions with all its properties and symmetries gets formulated in the language of a local Lagrangian density $\mathcal{L}(\phi(x), \partial_\mu \phi(x))$ which enters the action action in the form

$$S[\phi] = \int d^d x \mathcal{L}(\phi(x), \partial_\mu \phi(x)). \quad (2.2)$$

As intended with the notation of Eq.(2.2), S acts as a functional of the quantum fields ϕ which describe the degrees of freedom of the underlying theory. In order to allow a propagation of the fields we include kinetic terms with partial derivatives acting on the fields. Those kinetic terms look different for scalar fields φ and fermion fields ψ in order to take care of their different spin statistics. We therefore write the kinetic terms as follows:

$$(D_\mu \varphi)^\dagger D^\mu \varphi, \quad (2.3a)$$

$$\bar{\psi} \gamma^\mu D_\mu \psi. \quad (2.3b)$$

Here the covariant derivative D_μ differs from the usual partial derivative ∂_μ in order to allow for a local gauge transformation. A short explanation will be given in the following:

Assume we have a field ϕ that transforms locally under a representation r of the unitary group $U(n)$, meaning

$$\phi' = U \phi, \quad (2.4a)$$

$$\phi'^\dagger = \phi^\dagger U^\dagger, \quad (2.4b)$$

with $U := U(x) \in U(n)$. So at each point in space time, ϕ transforms covariantly by the unitary matrix U . Thus if we want to construct a theory that is symmetric under $U(n)$, terms in powers of $\phi^\dagger \phi$ can be added to the Lagrangian, as

$$\phi'^\dagger \phi' = \phi^\dagger U^\dagger U \phi = \phi^\dagger \phi \quad (2.5)$$

forms an invariant. But the partial derivative acting on the field will not transform covariantly, since it yields

$$\partial_\mu \phi' = U \partial_\mu \phi + (\partial_\mu U) \phi. \quad (2.6)$$

In order to cure the transformation properties of the derivative the covariant D_μ derivative comes into place, that by definition transforms as

$$D'_\mu = U D_\mu U^\dagger, \quad (2.7)$$

leading again to a covariant transformation of the derivative term

$$D'_\mu \phi' = U D_\mu U^\dagger U \phi = U D_\mu \phi. \quad (2.8)$$

In this way we ensure to build a symmetric Lagrangian also using derivative terms, which can now form kinetic terms of the fields. There is still one further point to discuss, as we introduced new degrees of freedom to our theory by demanding the covariant derivative D_μ to have the local transformation properties shown in Eq. (2.7). This will become more clear when we write down D_μ explicitly and describe its space time dependence by introducing the gauge fields $A_\mu^a := A_\mu^a(x)$. We obtain

$$D_\mu = \partial_\mu - ig A_\mu^a t_r^a, \quad (2.9)$$

with the gauge coupling parameter g and the traceless group generators $t_r^a \in \mathfrak{u}(n)$. Those generators follow the commutation relation

$$[t_r^a, t_r^b] = i f^{abc} t_r^c, \quad (2.10)$$

with the usual commutator $[\bullet, \bullet]$ and structure constants f^{abc} of the Lie algebra of $U(n)$. Therefore this relation is to be satisfied for all representations.

In principle we can now evaluate the transformation behavior of A_μ^a , such that Eq. (2.7) gets fulfilled. But for our purpose it is enough that A_μ^a can be chosen to satisfy this condition.

We need to add kinetic terms of the gauge fields. For this purpose we define the field-strength tensor¹

$$\hat{F}^{\mu\nu} := \frac{1}{-ig} [\hat{D}^\mu, \hat{D}^\nu] = t^a \left(\partial^\mu A^{a\nu} - \partial^\nu A^{a\mu} + g f^{abc} A^{b\mu} A^{c\nu} \right) =: t^a F^{a\mu\nu} \quad (2.11)$$

¹In this thesis, \hat{D}_μ will refer to the covariant derivative in the defining (also called fundamental) representation in contrast to D_μ which will be used for a general representation.

where t^a are now the generators in the n dimensional defining representation of $U(n)$. Although the definition of the field-strength tensor holds for the commutator of covariant derivatives in a general representation, we choose the defining representation such that the kinetic terms get the usual canonical normalization. $\hat{F}^{\mu\nu}$ is now an object including derivative terms of the gauge bosons, but no derivatives acting on following fields. The transformation properties are known from the covariant derivative and read

$$\hat{F}'^{\mu\nu} = \frac{1}{-ig} [\hat{D}'^\mu, \hat{D}'^\nu] = U \frac{1}{-ig} [\hat{D}^\mu, \hat{D}^\nu] U^\dagger = U \hat{F}^{\mu\nu} U^\dagger. \quad (2.12)$$

Thus by taking the trace of a product of field-strength tensors we automatically ensure gauge invariance in the Lagrangian. Therefore

$$-\frac{1}{2} \text{Tr} \left(\hat{F}^{\mu\nu} \hat{F}_{\mu\nu} \right) = -\frac{1}{2} \partial_\mu A^a_\nu (\partial^\mu A^{a\nu} - \partial^\nu A^{a\mu}) - \dots \quad (2.13)$$

will be the gauge kinetic term in the Lagrangian. This concludes the basic principles of local gauge theory that are relevant for the purpose of this thesis.

At this point we are ready to do some dimensional analysis. In the chosen natural units convention S is dimensionless, as $[S] = [\hbar] = 0$.² As $d^d x$ has dimension $-d$ and each derivative carries a dimension of 1, the dimension of the fields are fixed by their kinetic term. Hence, we get for the fields

$$[\psi] = \frac{d-1}{2}, \quad (2.14a)$$

$$[\phi] = \frac{d-2}{2}, \quad (2.14b)$$

$$[A] = \frac{d-2}{2}. \quad (2.14c)$$

As we usually work in $d = 4$ space-time dimensions, the dimensions are $[\psi] = \frac{3}{2}$, $[\phi] = 1 = [A]$. With this information, we can determine the energy dimension of each operator constructed of fields and derivatives that may appear in the Lagrangian. If the operator dimension differs from 4, it needs a parameter with an energy scale in order to form a proper term in the Lagrangian. As it turns out when analyzing the renormalization behavior of the terms in the Lagrangian³, we can only construct a consistent theory containing finite terms in the Lagrangian if we limit the maximum operator dimension to 4. This is a desired feature, as all the parameters of such a theory can be accessed by a finite number of experiments. However, there are also reasons for doing phenomenology with theories including higher-dimensional operators, as will be discussed in Chapter 3.

We now want to give the basic principles on calculations of predictions of observables using perturbative QFT. We start with the least-action principle, already known from classical mechanics. We demand a vanishing variation of the action with respect to the configuration of ϕ , namely

$$0 = \delta S = \int dx^d \left(\frac{\partial \mathcal{L}}{\partial \phi} - \partial_\mu \frac{\partial \mathcal{L}}{\partial (\partial_\mu \phi)} \right) \delta \phi, \quad (2.15)$$

²[...] meaning the power in dimension of energy, i.e. $[M] = 1$.

³This topic is discussed in all the standard textbooks on QFT, e.g. in Refs.[11, 12].

in order to find the equation of motion (EoM)

$$\frac{\partial \mathcal{L}}{\partial \phi} - \partial_\mu \frac{\partial \mathcal{L}}{\partial (\partial_\mu \phi)} = 0. \quad (2.16)$$

Terms in the Lagrangian that only involve products of two fields can be solved exactly by free field solutions. Therefore, we may separate the Lagrangian into

$$\mathcal{L} = \mathcal{L}_{free} + \mathcal{L}_I, \quad (2.17)$$

where \mathcal{L}_{free} denotes the free field part and \mathcal{L}_I the interaction part of the Lagrangian involving products of more than two fields. The free theory gets solved in terms of a second quantization procedure.

In particle physics we most commonly perform scattering experiments to probe the interaction Lagrangian \mathcal{L}_I . From the theoretical point of view the scattering process can be understood as a transition from an initial state in the distant past $|i, t \rightarrow -\infty\rangle$ to a far future final state $|f, t \rightarrow \infty\rangle =: |f\rangle$ and the states at times $t \rightarrow \pm\infty$ are seen as asymptotically free. We define the \mathcal{S} -matrix which denotes the transition from initial state to final state including the time evolution with respect to the interaction part

$$\mathcal{S}_{fi} = \langle f | \mathcal{S} | i \rangle = \langle f, t \rightarrow \infty | | i, t \rightarrow -\infty \rangle. \quad (2.18)$$

The elements of the non-trivial part of the \mathcal{S} -matrix $i\mathcal{T}_{fi} = \mathcal{S}_{fi} - \delta_{fi}$ can be brought to a more useful form

$$\mathcal{T}_{fi} = (2\pi)^4 \delta^{(4)}(q_f - p_i) \mathcal{M}_{fi}, \quad (2.19)$$

where we extracted the energy-momentum conservation. \mathcal{M}_{fi} is commonly known as the Feynman amplitude of the process $i \rightarrow f$. If the interaction part of the Lagrangian has a suppression due to a small coupling, we can apply the framework of perturbation theory. In that sense, the \mathcal{S} -matrix can be expanded in an infinite series of powers of the coupling constant, whilst the quantum fields used in the expressions are taken as free fields. Likewise, this allows to use Feynman rules in order to calculate the amplitude \mathcal{M}_{fi} up to the desired order in perturbation theory.

In order to have a measure of the scattering probability, we introduce the cross section σ for a process $p_1 p_2 \rightarrow q_1, \dots, q_n$. The differential cross section is defined as

$$d\sigma = \frac{1}{(2E_1)(2E_2)|\vec{v}_1 - \vec{v}_2|} |\mathcal{M}_{fi}|^2 d\Phi_n(p_1, p_2; q_1 \dots q_n), \quad (2.20)$$

where

$$d\Phi_n(p_1, p_2; q_1 \dots q_n) = \frac{d^3 q_1}{2E_{q_1}(2\pi)^3} \dots \frac{d^3 q_n}{2E_{q_n}(2\pi)^3} (2\pi)^4 \delta^{(4)}(q_1 + \dots + q_n - p_1 - p_2) \quad (2.21)$$

is the n -particle Lorentz-invariant phase space. In the center of mass (COM) frame of a $2 \rightarrow 2$ scattering of particles with the same mass, the differential cross section formula above reduces to [13]

$$d\sigma = \frac{1}{64\pi^2 s} |\mathcal{M}_{fi}|^2 d\Omega. \quad (2.22)$$

This is the form we will use in Section 5.4 for the cross section calculation.

2.2. The Standard Model and its $SU(2)_L$ limit

The Standard Model of particle physics (SM) is the by now well-established theory describing a broad spectrum of particle physics phenomenology. It is constructed as a local gauge theory that includes three of the four fundamental interactions of nature, only missing gravity. The other three interactions form the gauge group of the SM

$$SU(3)_{QCD} \times SU(2)_L \times U(1)_Y, \quad (2.23)$$

where the $SU(3)_{QCD}$ is the gauge group of Quantum Chromodynamics (QCD) which is the underlying theory of the strong interaction, and $SU(2)_L \times U(1)_Y$ the gauge group of electroweak (EW) interactions. The index L represents the maximally parity-violating coupling of the weak bosons W^a to the SM fermions and the $U(1)_Y$ is the hypercharge gauge group of the B -boson. The coupling parameters are denoted with g_s for $SU(3)_{QCD}$, g for the $SU(2)_L$ and g' for $U(1)_Y$, leading to the covariant derivative

$$D_\mu = \partial_\mu - ig_s T^{a_s} G_\mu^{a_s} - ig \frac{\tau^a}{2} W_\mu^a - ig' Y B_\mu, \quad (2.24)$$

where T^{a_s} are the generators of the $SU(3)_{QCD}$, $\frac{\tau^a}{2}$ are half the Pauli matrices that form the generators of $SU(2)_L$ in the defining representation and Y is the hypercharge operator.

The full Lagrangian of the SM can be decomposed as

$$\mathcal{L}_{SM} = \mathcal{L}_{Gauge} + \mathcal{L}_{Matter} + \mathcal{L}_{Higgs} + \mathcal{L}_{Yukawa}. \quad (2.25)$$

The gauge part of the Lagrangian \mathcal{L}_{Gauge} involves the gauge-kinetic terms for the three gauge groups, as already discussed in the previous section. \mathcal{L}_{Matter} consists of the kinetic terms for the SM fermion species, which can be aligned in three families of quarks, i.e. strongly interacting fermions, and leptons. Only the left-chiral fermions form doublets transforming under $SU(2)_L$, whereas the right-chiral fermions are singlets, and each field has its individual hypercharge eigenvalue Y assigned. \mathcal{L}_{Higgs} contains the kinetic term for the scalar SM Higgs doublet and its potential, and \mathcal{L}_{Yukawa} describes the Yukawa interaction between the Higgs field and the fermions. As the naive insertion of mass terms of the SM fields would not allow for a gauge interaction, a dynamical process involving the Higgs boson comes into place. For a detailed description we refer to common textbooks, like Refs. [11, 12].

The parameters in the Higgs potential are configured in a way, that the Higgs doublet acquires a non-vanishing vacuum expectation value (VEV) after so-called electroweak symmetry breaking, i.e. when the universe has cooled down to temperatures below TeV. As the Higgs field forms a $SU(2)_L$ doublet and also has a hypercharge, this VEV spontaneously breaks the $SU(2)_L$ and $U(1)_Y$ simultaneously, leaving only the residual electromagnetic $U(1)_{em}$ as an exact symmetry. The Goldstone theorem now states that the theory has three massless bosonic degrees of freedom in the Higgs doublet, which can be absorbed as longitudinal degrees of freedom of the weak bosons. A practical implementation of this absorption is the unitary gauge. The remaining Higgs field is identified as the massive physical Higgs boson. At the same time the Higgs VEV can now serve in the Lagrangian as a parameter of energy dimension, giving a mass-term to the weak bosons through the

Higgs kinetic term and to fermion fields through Yukawa interaction. The physical gauge bosons W^\pm , Z and the photon (A) are then obtained from W^a and B by

$$W^\pm = \frac{1}{\sqrt{2}} (W^1 \mp iW^2) , \quad (2.26a)$$

$$Z = \frac{g}{\sqrt{g^2 + g'^2}} W^3 - \frac{g'}{\sqrt{g^2 + g'^2}} B , \quad (2.26b)$$

$$A = \frac{g'}{\sqrt{g^2 + g'^2}} W^3 + \frac{g}{\sqrt{g^2 + g'^2}} B . \quad (2.26c)$$

In the subsequent work of the thesis, we restrict the discussion to the electroweak sector in the $SU(2)_L$ limit of the SM. This effectively means to set $g' \rightarrow 0$. As there is no $U(1)_Y$, we will not find a residual electromagnetic symmetry after symmetry breaking. Therefore, there will be no appearance of the photon A and the physical Z -boson is identified as the W^3 of the $SU(2)_L$ gauge boson triplet, having the mass $m_Z = m_W$ after electroweak symmetry breaking.

The reason for working in the $SU(2)_L$ limit is that it drastically simplifies the subsequent discussions and still allows for enough freedom to analyze some of the the basic properties in vector-boson scattering.⁴ Including the photon in the calculation of vector-boson scattering would complicate all calculations substantially without gaining a deeper insight. In the on-shell scattering of charged vector bosons we would have a pole in the t -channel exchange of photons for small angles. This is the well-known Rutherford pole, that appears due to the long-range interaction of quantum electrodynamics (QED). Having a long-range interaction spoils the convergence of the partial wave expansion and the projection on its coefficients which is introduced in Section 3.2. In addition, in the $SU(2)_L$ limit we do not have to consider processes with external photons in the $SU(2)_L$ limit. Also having equal masses for the W^\pm and Z bosons further simplifies the kinematics in the calculation of vector-boson scattering.

2.3. One-loop corrections

It is part of any introductory course on QFT, that a naive calculation of one-loop integrals does not work and leads to infinities that originate from integrating over loop momenta up to infinity. But during the last century clever theoretical physicist developed prescriptions that help us to deal with such ultraviolet (UV) infinities. One common prescription is dimensional regularization (DimReg) which is particularly of interest, as it conserves gauge symmetries. In this prescription the theory is analytically continued from 4 to d space-time dimension for all the calculations and in the end the limit $d \rightarrow 4 - 2\epsilon$ for infinitesimal ϵ is performed which allows to make ultraviolet divergences explicit in the form of inverse

⁴Including new particles that transform under a representation of the $SU(2)_L$ suffices for loop-induced corrections to the vector-boson scattering processes. Hence, we are also able to parametrize vector-boson scattering in the effective field theory approach by deriving the low-energy limit of the vertex corrections. All that is carried out in the subsequent chapters.

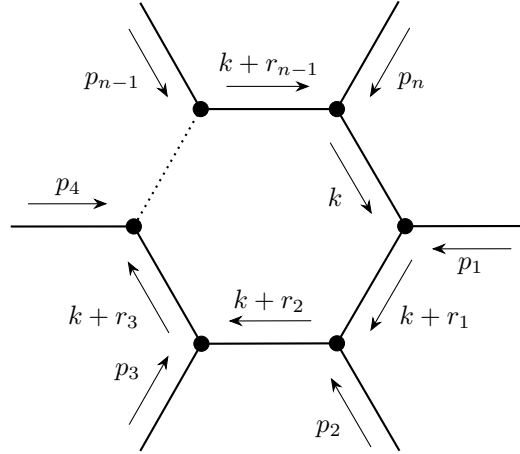


Figure 2.1.: Definition of an example one-loop diagram.

powers in ϵ . Therefore, we can absorb those terms in a proper renormalization procedure such that resulting physical quantities are UV finite.

In a general DimReg one-loop calculation we have to deal with loop Feynman diagrams of the form of Fig. 2.1.⁵ The corresponding analytic expressions will result in tensor integrals that take the form⁶

$$T^{\mu_1 \dots \mu_p} = \frac{\mu^{4-d}}{(2\pi)^d} \int d^d k \frac{k^{\mu_1} \dots k^{\mu_p}}{D_0 D_1 \dots D_{n-1}}, \quad (2.27)$$

where μ is the renormalization scale which appears in order to keep the energy dimension of the coupling parameters in the Lagrangian fixed as the integral measure of the action and the energy dimension of the fields change, as is shown in Eqs. (2.2) and (2.14), respectively. The denominators D_i are of the form $D_i = (k + r_i)^2 - M_i^2$. The momenta r_i are defined as the sum of incoming momenta $r_i = \sum_{j=0}^i p_j$ and the special case $r_0 = r_n$ vanishes from energy-momentum conservation $r_0 = r_n = \sum_{j=0}^n p_j = 0$.

In Appendix A.1 we will highlight how such one-loop integrals are calculated. There is a generic approach based on a few master integrals which will be part of Appendix A.1.1. This is only in some occasions a practical way to calculate, e.g. for the field renormalization, and, in this thesis, it was used in the matching procedure of the Wilson coefficients for the effective description of the new physics contribution which is discussed in Section 4.3. But as calculations tend to get very lengthy in a full loop calculation t'Hooft, Veltman and Passarino developed an algorithm [15, 16] to decompose complicated tensor integrals in a basis of scalar integrals (PV loop functions) which can be systematically reconstructed and easily numerically calculated. The basic idea will be presented in Appendix A.1.2. Built on this procedure there are programs for a numerical calculation available like `LoopTools` [17], which was used in this thesis to obtain expressions for the one-loop amplitude of the full model.

⁵All Feynman diagrams in this thesis were created with `TikZ-Feynman` [14].

⁶Notice that scalar integrals are meant to be included as a specific type of tensor.

3. Effective field theory

Even though the SM shows perfect agreement with often high accuracy for almost all of the current experiments in high energy physics, we do not expect it to be the final answer, since it fails to describe a number of phenomena that appear in astrophysics, cosmology and low-energy physics. Some prominent features are baryon asymmetry or the abundance of invisible matter in the universe, so-called dark matter, which is indicated by the rotation of galaxies or by gravitational lensing. So theoretical particle physicists continue to develop extensions of the SM in order to give a more complete description of nature. At colliders the common search strategies are either a direct search for new degrees of freedom, i.e. particles, or an indirect search through precision observables. The first strategy in form of “bump” events is experimentally simple, but limited by collider energy. The second strategy needs precise predictions of observables in many kinematic regions. With (almost) infinite possibilities of SM extensions at hand this poses the problem in which direction of model building to go.

Therefore a description of new physics (NP) by introducing effective couplings of the SM fields can be a powerful tool, because possible signals of NP can be modeled without being restricted to a specific SM extension. This type of effective field theory (EFT) framework is usually called a *bottom-up* approach, because we parameterize still unknown NP of high energies with the methods and fields present at the lower energy regime. The EFT Lagrangian can be represented as a series of higher dimensional operators $O_i^{(n+4)}$ expanded in powers of a suppression parameter characteristic for the (energy) regime of NP. Note that the $O_i^{(n+4)}$ are constructed from the fields of the low-energy regime only and are restricted to satisfy the symmetries expected by NP models.

From the perspective of a known high-energy physics model, it is often more useful to express effects on low-energy processes by using the EFT description. For that *top-down* point of view the low-energy EFT operators and Wilson coefficients are understood to follow from integrating out the heavy degrees of freedom of the underlying theory. This can also be used to extract bounds from experiment on the parameter space of the EFT parameters in order to disfavor specific SM extensions. But such statements have to be done with care, which will be pointed out in the following discussions of the thesis.

Combining both perspectives, we can study the basic principles of an EFT in a specific application. In the case of VBS that is the aim of our work.

We write down the EFT series explicitly in the form

$$\mathcal{L}_{EFT} = \mathcal{L}_0 + \sum_{n=1}^{\infty} \sum_i \frac{f_i^{(n)}}{\Lambda^n} O_i^{(n+4)}, \quad (3.1)$$

where the expansion parameter Λ denotes the characteristic energy scale of the underlying NP and $f_i^{(n)}$ are the resulting dimensionless Wilson coefficients describing the coupling strength. \mathcal{L}_0 is the ultraviolet (UV) complete part of the Lagrangian which contains the SM alone. Here we can clearly see the suppression of higher-order terms for low energies $\sqrt{s} \ll \Lambda$. The energy dependence comes from external kinematics or momentum dependence of the operators themselves. Hence, for probing at low energies a finite sum of all operators up to a given order of $\frac{1}{\Lambda}$ should give a reasonable description of residual effects of NP. Up to which order in $\frac{1}{\Lambda}$ the EFT is taken into account is a matter of desired precision, pursuit of a most general description and affordable computation power.

3.1. Constructing the effective field theory basis

First we have to specify our assumptions on the NP which we want to parameterize using an EFT, in order to get a reasonable, but not too blown up basis of our EFT Lagrangian. Thus we want to make sure to work with a model that is complete enough to get a deeper insight into the validity regions of EFTs in VBS without being dragged away into all the possibilities we could think of.

In our work we want to describe VBS for the $SU(2)_L$ limit of the SM. We restrict the underlying NP to couple to the $SU(2)_L$ gauge bosons only and, therefore, it only modifies the gauge boson couplings in the low energy regime. Also we do not want to introduce any new symmetry breaking. So our operators have to be manifestly invariant under $SU(2)_L$ and it makes sense to construct them out of field-strength tensors and covariant derivatives only, thus, we only have to take into account operators with even dimension, as otherwise Lorentz invariance would be broken. And, as already mentioned in Section 2.1, all terms will then arise with a trace in $SU(2)_L$ space. For describing VBS with an EFT using only gauge fields, we have to describe vacuum polarization effects, anomalous triple-gauge couplings (aTGC) and anomalous quartic-gauge couplings (aQGC). As was pointed out in Ref. [18], it is reasonable to include operators up to dimension 8, as dimension 6 operators are rather measured in aTGCs obtained from other processes, like vector boson pair production ($q\bar{q}' \rightarrow V_1 V_2$). In a real physical environment like the LHC, VBS usually occurs with a comparably small cross section. On top of that the aQGCs induced by dimension 6 operators does not give enough freedom to parametrize all possible VBS processes. We will later point out, that the dimension 6 operators of our basis are lacking a tree level induced $ZZ \rightarrow ZZ$ process. Those tree level processes will be only introduced by the T-Operators mentioned in Eqs. (3.8).

So, as we formulated our goals, we continue with a strategy on how to construct a complete basis.

3.1.1. Techniques and strategy

Our strategy is to fill all linearly independent operators for each energy dimension starting from the lowest energy dimension. Following the definition of Ref. [19], linear dependence in this context means that there exists a set of constants $k_i \neq 0$ for the operators $\{O_i\}$,

such that

$$\sum_i k_i O_i = 0, \quad (3.2)$$

where the equation means, that all contributions vanish for perturbative calculations. This allows us to neglect the surface terms coming from integration by parts (IBP). We will use the following relations¹ in order to check for linear dependence:

- IBP for the covariant derivative

$$\text{Tr} \left([\hat{D}_\mu, \hat{\Phi}_1] \hat{\Phi}_2 \dots \hat{\Phi}_n \right) = \partial_\mu \text{Tr} \left(\hat{\Phi}_1 \hat{\Phi}_2 \dots \hat{\Phi}_n \right) - \text{Tr} \left(\hat{\Phi}_1 [\hat{D}_\mu, \hat{\Phi}_2 \dots \hat{\Phi}_n] \right), \quad (3.3)$$

- Jacobi identity (JI) for covariant derivatives

$$[\hat{D}_\mu, \hat{W}_{\nu\rho}] + [\hat{D}_\nu, \hat{W}_{\rho\mu}] + [\hat{D}_\rho, \hat{W}_{\mu\nu}] = 0, \quad (3.4)$$

- Commutator of covariant derivatives in adjoint representation (CA)

$$[\hat{D}_{[\mu}, [\hat{D}_{\nu]}, \hat{\Phi}] = g \epsilon^{abc} t^a W_{\mu\nu}^b \Phi^c. \quad (3.5)$$

For each dimension we start with adding all combinations composed of field-strength tensors solely, and then subsequently construct the linear independent combinations with rising amount of covariant derivatives. We ensure in this way, that all relevant combinations are going to be taken into account.

3.1.2. Dimension 4 operators

For the sake of completeness, we will also consider here the dimension 4 operator

$$O_{WW} = \text{Tr} \left(\hat{W}^{\mu\nu} \hat{W}_{\mu\nu} \right), \quad (3.6)$$

which is already part of the SM Lagrangian \mathcal{L}_0 . It also receives contributions in the matching of our NP model, but through renormalization this contribution can be set to zero.

3.1.3. Dimension 6 operators

In the class of dimension 6 operators we can construct one operator of three field-strength tensors, but there is also one independent possibility for two field-strength tensors combined with two covariant derivatives. Here the following combination is chosen:

$$O_{WWW} = \text{Tr} \left(\hat{W}^\mu_\nu \hat{W}^\nu_\rho \hat{W}^\rho_\mu \right), \quad (3.7a)$$

$$O_{DW} = \text{Tr} \left([\hat{D}_\alpha, \hat{W}^{\mu\nu}] [\hat{D}^\alpha, \hat{W}_{\mu\nu}] \right). \quad (3.7b)$$

Those operators are commonly used in the literature, e.g. in Ref. [20].

¹The derivations are shown in Appendix A.3.

3.1.4. Dimension 8 operators

Constructing a full basis with dimension 8 operators for all SM fields poses a big obstacle, because the number of possible operators is huge. But fortunately, for the analysis of a lot of phenomenological processes we need not to consider all operators, as their contribution would enter only at higher loop order. For our case the operators used in VBS are even further reduced, as we only include the W field in our discussion. Following the notation of Refs. [4, 18, 21, 22] the operators involving four field-strength tensors are given by

$$O_{T_0} = \text{Tr} \left(\hat{W}^{\mu\nu} \hat{W}_{\mu\nu} \right) \text{Tr} \left(\hat{W}^{\alpha\beta} \hat{W}_{\alpha\beta} \right), \quad (3.8a)$$

$$O_{T_1} = \text{Tr} \left(\hat{W}^{\mu\nu} \hat{W}_{\alpha\beta} \right) \text{Tr} \left(\hat{W}^{\alpha\beta} \hat{W}_{\mu\nu} \right), \quad (3.8b)$$

$$O_{T_2} = \text{Tr} \left(\hat{W}^{\mu\nu} \hat{W}_{\nu\alpha} \right) \text{Tr} \left(\hat{W}^{\alpha\beta} \hat{W}_{\beta\mu} \right), \quad (3.8c)$$

$$O_{T_3} = \text{Tr} \left(\hat{W}^{\mu\nu} \hat{W}^{\alpha\beta} \right) \text{Tr} \left(\hat{W}_{\nu\alpha} \hat{W}_{\beta\mu} \right), \quad (3.8d)$$

where O_{T_3} is a non-vanishing linear independent operator which was missing in previous discussions in the theory literature[4, 18, 21, 22], and therefore is also not experimentally constrained [23].² We will refer to operators of the set in Eq. (3.8) as T-operators throughout the thesis.

For three field-strength tensors combined with covariant derivatives acting on them we can construct the following dimension 8 operators

$$O_0 = \text{Tr} \left([\hat{D}_\alpha, \hat{W}_\nu^\mu] [\hat{D}^\alpha, \hat{W}_\rho^\nu] \hat{W}_\mu^\rho \right), \quad (3.10a)$$

$$O_{1,0} = \text{Tr} \left([\hat{D}_\alpha, \hat{W}^{\mu\nu}] [\hat{D}_\beta, \hat{W}_{\mu\nu}] \hat{W}^{\alpha\beta} \right), \quad (3.10b)$$

$$O_{1,1} = \text{Tr} \left([\hat{D}_\alpha, \hat{W}^{\mu\nu}] \hat{W}_{\mu\nu} [\hat{D}_\beta, \hat{W}^{\alpha\beta}] \right), \quad (3.10c)$$

$$O_{2,1} = \text{Tr} \left([\hat{D}_\alpha, \hat{W}^{\mu\nu}] [\hat{D}_\beta, \hat{W}_\mu^\alpha] \hat{W}_\nu^\beta \right), \quad (3.10d)$$

$$O_{2,2} = \text{Tr} \left([\hat{D}_\beta, \hat{W}^{\mu\nu}] [\hat{D}_\alpha, \hat{W}_\mu^\alpha] \hat{W}_\nu^\beta \right), \quad (3.10e)$$

$$O_{2,3} = \text{Tr} \left([\hat{D}_\beta, \hat{W}_\mu^\alpha] [\hat{D}_\alpha, \hat{W}_\nu^\beta] \hat{W}^{\mu\nu} \right), \quad (3.10f)$$

$$O_{2,4} = \text{Tr} \left([\hat{D}_\alpha, \hat{W}_\mu^\alpha] [\hat{D}_\beta, \hat{W}_\nu^\beta] \hat{W}^{\mu\nu} \right). \quad (3.10g)$$

We do not need to include operators with both derivatives acting on one tensor, as they are connected via IBP to a linear combination of the above mentioned operators.

²In the same way, the operators called O_{T_5} , O_{T_6} and O_{T_7} in Ref. [21] do not take into account all possible Lorentz index contractions, therefore the operator

$$O_{T_X} = \text{Tr} \left(\hat{W}^{\mu\nu} \hat{W}^{\alpha\beta} \right) \hat{B}_{\nu\alpha} \hat{B}_{\beta\mu} \quad (3.9)$$

should be added to future EFT bases which include the hypercharge boson.

In the following, we are looking for relations between those operators using JI and IBP. Starting with $O_{1,1}$ we have

$$\begin{aligned} O_{1,1} &\stackrel{\text{IBP}}{=} -\text{Tr} \left([\hat{D}_\alpha, \hat{W}^{\mu\nu}] [\hat{D}_\beta, \hat{W}_{\mu\nu}] \hat{W}^{\alpha\beta} \right) - \text{Tr} \left([\hat{D}_\beta, [\hat{D}_\alpha, \hat{W}^{\mu\nu}]] \hat{W}_{\mu\nu} \hat{W}^{\alpha\beta} \right) \\ &= -O_{1,0} + O_T, \end{aligned} \quad (3.11)$$

where in the last line we used the fact that contracting the Lorentz indices from the covariant derivatives with $\hat{W}^{\alpha\beta}$ forces antisymmetrization which results in an additional field-strength tensor. Hence, the notation O_T was used for any combination of the already considered T-operators.

Rewriting the operators $O_{1,0}$, $O_{2,1}$ and $O_{2,2}$ leads to

$$\begin{aligned} O_{1,0} &\stackrel{\text{JI}}{=} -\text{Tr} \left([\hat{D}_\mu, \hat{W}^{\nu\alpha}] [\hat{D}_\beta, \hat{W}_\nu^\mu] \hat{W}_\alpha^\beta \right) - \text{Tr} \left([\hat{D}_\nu, \hat{W}^{\alpha\mu}] [\hat{D}_\beta, \hat{W}_\mu^\nu] \hat{W}_\alpha^\beta \right) \\ &= 2 \text{Tr} \left([\hat{D}_\alpha, \hat{W}^{\mu\nu}] [\hat{D}_\beta, \hat{W}_\mu^\alpha] \hat{W}_\nu^\beta \right) = 2O_{2,1}, \end{aligned} \quad (3.12)$$

$$\begin{aligned} O_{2,1} &\stackrel{\text{JI}}{=} -\text{Tr} \left([\hat{D}_\alpha, W^{\mu\nu}] [\hat{D}^\alpha, W_{\mu\beta}] W_\nu^\beta \right) - \text{Tr} \left([\hat{D}_\alpha, W^{\mu\nu}] [\hat{D}_\mu, W_\beta^\alpha] W_\nu^\beta \right) \\ &= O_0 + \text{Tr} \left([\hat{D}_\alpha, W_\nu^\beta] [\hat{D}_\beta, W_\mu^\alpha] W^{\mu\nu} \right) = O_0 - O_{2,3}, \end{aligned} \quad (3.13)$$

$$\begin{aligned} O_{2,2} &\stackrel{\text{JI}}{=} -\text{Tr} \left([\hat{D}_\mu, W^{\nu\beta}] [\hat{D}_\alpha, W^{\alpha\mu}] W_{\beta\nu} \right) - \text{Tr} \left([\hat{D}_\nu, W^{\beta\mu}] [\hat{D}_\alpha, W_\mu^\alpha] W_\nu^\beta \right) \\ &= -\text{Tr} \left([\hat{D}_\alpha, W^{\nu\mu}] [\hat{D}_\beta, W^{\beta\alpha}] W_{\mu\nu} \right) - \text{Tr} \left([\hat{D}_\beta, W^{\nu\mu}] [\hat{D}_\alpha, W_\mu^\alpha] W_\nu^\beta \right) \\ &= O_{1,1} - O_{2,2} = \frac{1}{2} O_{1,1}, \end{aligned} \quad (3.14)$$

where we renamed contracted indices after using JI to identify them with operators of the set presented in Eq. (3.10).

For the last relation we start with rewriting operators of two derivatives acting on one field-strength tensor, such that

$$\begin{aligned} &\text{Tr} \left(W^{\mu\nu} [\hat{D}_\alpha, [\hat{D}_\beta, W_\mu^\alpha]] W_\nu^\beta \right) \\ &\stackrel{\text{IBP}}{=} -\text{Tr} \left([\hat{D}_\alpha, W^{\mu\nu}] [\hat{D}_\beta, W_\mu^\alpha] W_\nu^\beta \right) - \text{Tr} \left(W^{\mu\nu} [\hat{D}_\beta, W_\mu^\alpha] [\hat{D}_\alpha, W_\nu^\beta] \right) \\ &= -O_{2,1} - O_{2,3}, \end{aligned} \quad (3.15)$$

$$\begin{aligned} &\text{Tr} \left(W^{\mu\nu} [\hat{D}_\beta, [\hat{D}_\alpha, W_\mu^\alpha]] W_\nu^\beta \right) \\ &\stackrel{\text{IBP}}{=} -\text{Tr} \left([\hat{D}_\beta, W^{\mu\nu}] [\hat{D}_\alpha, W_\mu^\alpha] W_\nu^\beta \right) - \text{Tr} \left(W^{\mu\nu} [\hat{D}_\alpha, W_\mu^\alpha] [\hat{D}_\beta, W_\nu^\beta] \right) \\ &= -O_{2,2} - O_{2,4}. \end{aligned} \quad (3.16)$$

And as the combination of both operators on the left-hand side of Eqs. (3.15) and (3.16) equals

$$\text{Tr} \left(W^{\mu\nu} [\hat{D}_\alpha, [\hat{D}_\beta, W_\mu^\alpha]] W_\nu^\beta \right) - \text{Tr} \left(W^{\mu\nu} [\hat{D}_\beta, [\hat{D}_\alpha, W_\mu^\alpha]] W_\nu^\beta \right) \stackrel{\text{CA}}{=} O_T, \quad (3.17)$$

we found the following 5 relations between our 7 operators shown in Eq. (3.10)

$$O_{1,1} = -O_{1,0} + O_T, \quad (3.18a)$$

$$O_{1,0} = 2O_{2,1}, \quad (3.18b)$$

$$O_{2,1} = O_0 - O_{2,3}, \quad (3.18c)$$

$$O_{2,2} = \frac{1}{2}O_{1,1}, \quad (3.18d)$$

$$O_{2,1} + O_{2,3} = O_{2,2} + O_{2,4} + O_T. \quad (3.18e)$$

Hence, there are only two linearly independent operators in the set shown in eq. 3.10, which we are free to choose. One legitimate choice are the operators O_0 and $O_{1,0}$, which will be used in the following thesis under the naming O_{DWWW_0} and D_{DWWW_1} , respectively.

For the case of two field-strength tensors we may pick

$$O_{D2W} = \text{Tr} \left([\hat{D}_\alpha, [\hat{D}^\alpha, \hat{W}^{\mu\nu}]] [\hat{D}_\beta, [\hat{D}^\beta, \hat{W}_{\mu\nu}]] \right), \quad (3.19)$$

as any other combination would not be independent. For example

$$\begin{aligned} \text{Tr} \left([\hat{D}_\alpha, [\hat{D}_\beta, \hat{W}^{\mu\nu}]] [\hat{D}^\alpha, [\hat{D}^\beta, \hat{W}_{\mu\nu}]] \right) &\stackrel{\text{CA}}{=} \text{Tr} \left([\hat{D}_\beta, [\hat{D}_\alpha, \hat{W}^{\mu\nu}]] [\hat{D}^\alpha, [\hat{D}^\beta, \hat{W}_{\mu\nu}]] \right) + O_{3W} \\ &\stackrel{\text{IBP}}{=} -\text{Tr} \left([\hat{D}^\alpha, [\hat{D}_\beta, [\hat{D}_\alpha, \hat{W}^{\mu\nu}]]] [\hat{D}^\beta, \hat{W}_{\mu\nu}] \right) + O_{3W} \\ &\stackrel{\text{CA}}{=} -\text{Tr} \left([\hat{D}_\beta, [\hat{D}^\alpha, [\hat{D}_\alpha, \hat{W}^{\mu\nu}]]] [\hat{D}^\beta, \hat{W}_{\mu\nu}] \right) + O_{3W} \\ &\stackrel{\text{IBP}}{=} O_{D2W} + O_{3W} \end{aligned} \quad (3.20)$$

will not give a linear independent contribution.³

Now our complete set of effective operators up to dimension 8 results in the following Lagrangian

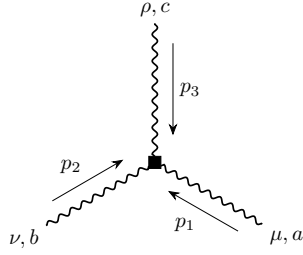
$$\begin{aligned} \mathcal{L}_{EFT} = & f_{WW} \text{Tr} \left(\hat{W}^{\mu\nu} \hat{W}_{\mu\nu} \right) + \frac{f_{DW}}{\Lambda^2} \text{Tr} \left([\hat{D}_\alpha, \hat{W}^{\mu\nu}] [\hat{D}^\alpha, \hat{W}_{\mu\nu}] \right) + \frac{f_{WWW}}{\Lambda^2} \text{Tr} \left(\hat{W}^\mu_\nu \hat{W}^\nu_\rho \hat{W}^\rho_\mu \right) \\ & + \frac{f_{D2W}}{\Lambda^4} \text{Tr} \left([\hat{D}_\alpha, [\hat{D}^\alpha, \hat{W}^{\mu\nu}]] [\hat{D}_\beta, [\hat{D}^\beta, \hat{W}_{\mu\nu}]] \right) + \frac{f_{DWWW_0}}{\Lambda^4} \text{Tr} \left([\hat{D}_\alpha, \hat{W}^\mu_\nu] [\hat{D}^\alpha, \hat{W}^\nu_\rho] \hat{W}^\rho_\mu \right) \\ & + \frac{f_{DWWW_1}}{\Lambda^4} \text{Tr} \left([\hat{D}_\alpha, \hat{W}^{\mu\nu}] [\hat{D}_\beta, \hat{W}^{\mu\nu}] \hat{W}^{\alpha\beta} \right) + \frac{f_{T_0}}{\Lambda^4} \text{Tr} \left(\hat{W}^{\mu\nu} \hat{W}_{\mu\nu} \right) \text{Tr} \left(\hat{W}^{\alpha\beta} \hat{W}_{\alpha\beta} \right) \\ & + \frac{f_{T_1}}{\Lambda^4} \text{Tr} \left(\hat{W}^{\mu\nu} \hat{W}_{\alpha\beta} \right) \text{Tr} \left(\hat{W}^{\alpha\beta} \hat{W}_{\mu\nu} \right) + \frac{f_{T_2}}{\Lambda^4} \text{Tr} \left(\hat{W}^\mu_\nu \hat{W}^\nu_\alpha \right) \text{Tr} \left(\hat{W}^\alpha_\beta \hat{W}^\beta_\mu \right) \\ & + \frac{f_{T_3}}{\Lambda^4} \text{Tr} \left(\hat{W}^{\mu\nu} \hat{W}^{\alpha\beta} \right) \text{Tr} \left(\hat{W}_{\nu\alpha} \hat{W}_{\beta\mu} \right). \end{aligned} \quad (3.21)$$

With the complete basis at hand we can now determine the Feynman rules for the effective propagator correction

$$\mu, a \text{ wavy line } \blacksquare \text{ wavy line } \nu, b =: i\delta^{ab} (p^2 g^{\mu\nu} - p^\mu p^\nu) \Pi_{EFT}(p, f_{WW}, f_{DW}, f_{D2W}, \Lambda), \quad (3.22)$$

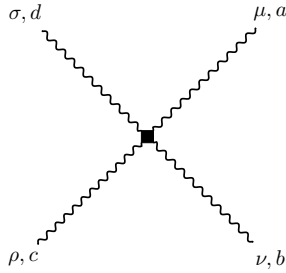
³ O_{3W} is a short-hand notation for a combination of already considered operators involving at least three field-strength tensors.

the three boson vertex



$$=: \epsilon^{abc} \Gamma_{3,EFT}^{\mu\nu\rho}(p_1, p_2, p_3, f_{WW}, f_{DW}, f_{WWW}, f_{D2W}, f_{DWWW1}, f_{DWWW2}, \Lambda), \quad (3.23)$$

and the four boson vertex



$$=: \Gamma_{4,EFT}^{\mu\nu\alpha\beta,abcd}(p_1, p_2, p_3, p_4, f_{WW}, f_{DW}, f_{WWW}, f_{D2W}, f_{DWWW1}, f_{DWWW2}, f_{T_0}, f_{T_1}, f_{T_2}, f_{T_3}, \Lambda). \quad (3.24)$$

The analytic expressions are obtained with the use of FeynCalc [24–26] in Mathematica, and implemented in the VeBoS code which is described in Appendix A.5. The result for the effective propagator correction, for example, is given by

$$\Pi_{EFT}(p, f_{WW}, f_{DW}, f_{D2W}, \Lambda) = 2 \left(f_{WW} + \frac{f_{DW}}{\Lambda^2} p^2 + \frac{f_{D2W}}{\Lambda^4} p^4 \right). \quad (3.25)$$

We expect, that the accuracy of this description will break down when we reach higher energies than the order of the energy scale Λ or beyond. At this point subsequent terms in the full series presented in Eq. (3.1) will become relevant, as the rough estimation of the finite expansion will not be enough to describe the complexity of the process anymore. At such high energies we left the validity region of the EFT. A formal way using the unitarity requirement for the definition of the validity region will be given in the following section.

3.2. Partial waves and unitarity

We will first start with basic unitarity considerations and follow hereby closely the derivation from Refs. [12, 18]. In order to ensure probability conservation, the scattering matrix \mathcal{S} , which describes the transition from an initial to a final state, has to be unitary, i.e.

$$\mathcal{S}^\dagger \mathcal{S} = 1, \quad (3.26)$$

where 1 represents the identity operator. By separating the non-trivial part of the \mathcal{S} -matrix in the common way

$$\mathcal{S} = 1 + i\mathcal{T}, \quad (3.27)$$

3. Effective field theory

we can rewrite the unitarity condition as

$$2\text{Im } \mathcal{T} = -i \left(\mathcal{T} - \mathcal{T}^\dagger \right) = \mathcal{T}^\dagger \mathcal{T} = \mathcal{T} \mathcal{T}^\dagger. \quad (3.28)$$

For a VBS process it will be sufficient to restrict the discussion to the subspace of two scattering bosons. To get a useful relation, we express the elements of the \mathcal{T} -matrix with the matrix elements \mathcal{M}_{fi}

$$\langle f | \mathcal{T} | i \rangle = (2\pi)^4 \delta^{(4)}(p_1 + p_2 - q_1 - q_2) \mathcal{M}_{fi}, \quad (3.29)$$

by using energy-momentum conservation. Inserting a sum over all intermediate two boson states

$$1 = \sum_n \int \frac{d^3 k_{n,1} d^3 k_{n,2}}{(2\pi)^3 2k_{n,1}^0 (2\pi)^3 2k_{n,2}^0} |k_{n,1}, k_{n,2}\rangle \langle k_{n,1}, k_{n,2}| \quad (3.30)$$

on the right hand side of Eq. (3.28), the resulting equation reads

$$2\text{Im } \mathcal{M}_{fi} = \sum_n \frac{\lambda^{\frac{1}{2}}(s, k_{n,1}^2, k_{n,2}^2)}{8\pi s} S_n \int \frac{d\Omega}{4\pi} \mathcal{M}_{nf}^* \mathcal{M}_{ni}, \quad (3.31)$$

where the Källén function

$$\lambda(x, y, z) = x^2 + y^2 + z^2 - 2xy - 2xz - 2yz \quad (3.32)$$

appeared from the phase-space integration of Eq. (3.30) and S_n is the statistical factor of the process, being $S_n = \frac{1}{2}$ if identical bosons in the state $|n\rangle$ are involved. If the initial and the final state are chosen to be identical, Eq. (3.31) is commonly called the optical theorem.

With the argument of angular momentum conservation and applying the Wigner-Eckart-Theorem, as demonstrated in Ref. [27], the amplitude in terms of helicity eigenstates $\mathcal{M}_{fi} = \mathcal{M}_{\lambda_1 \lambda_2 \lambda_3 \lambda_4}$ can be expanded in partial waves (PW) [18]

$$\mathcal{M}_{\lambda_1 \lambda_2 \lambda_3 \lambda_4}(s, \theta, \phi) = 8\pi \mathcal{N}_{fi} \sum_{j=\max(|\lambda_{12}|, |\lambda_{34}|)}^{\infty} (2j+1) \mathcal{A}_{\lambda_1 \lambda_2 \lambda_3 \lambda_4}^j(s) d_{\lambda_{12} \lambda_{34}}^j(\theta) e^{i\lambda_{34}\phi}. \quad (3.33)$$

Therein we define $\lambda_{kl} = \lambda_k - \lambda_l$ and $d_{\lambda_{12} \lambda_{34}}^j$ describes the Wigner d-matrix and the normalization factor \mathcal{N}_{fi} is given by

$$\mathcal{N}_{fi} = \frac{s}{\lambda^{\frac{1}{4}}(s, p_1^2, p_2^2) \lambda^{\frac{1}{4}}(s, q_1^2, q_2^2)} \frac{1}{\sqrt{S_f S_i}}. \quad (3.34)$$

This normalization factor reduces in the on-shell scattering of particles with same masses in the center of mass frame (COM) to

$$\mathcal{N}_{fi} = \frac{1}{\beta} \frac{1}{\sqrt{S_f S_i}}, \quad (3.35)$$

where the relativistic beta-factor $\beta = \sqrt{1 - \frac{4m^2}{s}}$ was introduced. Exploiting the orthogonality relation of the Wigner d-function

$$\int_{-1}^1 d \cos \theta d_{\lambda\kappa}^j(\theta) d_{\lambda\kappa}^{j'}(\theta) = \frac{2}{2j+1} \delta^{jj'}, \quad (3.36)$$

we can project out the PW coefficients by integrating over θ in the form

$$\mathcal{A}_{\lambda_1 \lambda_2 \lambda_3 \lambda_4}^j(s) = \frac{\beta \sqrt{S_f S_i}}{16\pi} \int_{-1}^1 d \cos \theta \mathcal{M}_{\lambda_1 \lambda_2 \lambda_3 \lambda_4}(s, \theta) d_{\lambda_{12} \lambda_{34}}^j(\theta). \quad (3.37)$$

Inserting Eq. (3.33) into Eq. (3.31), this orthogonality relation also results in

$$2\text{Im} \left(\mathcal{A}_{\lambda_1 \lambda_2 \lambda_3 \lambda_4}^j \right) = \sum_n \sum_{\lambda'_1, \lambda'_2} \mathcal{A}_{\lambda_3 \lambda_4 \lambda'_1 \lambda'_2}^{j*} \mathcal{A}_{\lambda_1 \lambda_2 \lambda'_1 \lambda'_2}^j, \quad (3.38)$$

where we directly used the full form of the normalization factor \mathcal{N}_{f_i} .⁴ To extract the unitarity bound, the matrices \mathcal{A}^j have to be diagonalized in the $(2s_1 + 1)(2s_2 + 1) \times (2s_1 + 1)(2s_2 + 1)$ helicity space and also, in the case of VBS, in the isospin base of the product space of two isospin $J = 1$ vector bosons⁵. The number of helicities is given by the particles' spin s_i , so we have to consider three helicities for each boson. For the eigenvalues a^j Eq. (3.38) then reads

$$2\text{Im} (a^j) = |a^j|^2, \quad (3.39)$$

which represents an equation for the Argand circle of unit radius centered around $(0, 1)$ in the complex plane, as is depicted in Fig. 3.1.

Up to now, we are talking about unitarity conditions a full theory has to obey. But, as we perturbatively calculate our matrix elements and, therefore, also the PW coefficients, the eigenvalues will not precisely lie on the Argand circle. This is especially true if we discuss tree level contributions, e.g. in EFT calculations, which will lie solely on the real axis. Hence, the unitarity bound gets rather expressed as

$$|\text{Re} (a^j)| \leq 1, \quad |a^j| \leq 2, \quad 0 \leq \text{Im} (a^j) \leq 2. \quad (3.40)$$

On the one hand those inequalities give us a measure, if we stay in a region of perturbative unitarity, meaning unitarity is sufficiently respected for the perturbative calculation. In this region we can well trust predictions based on a perturbative expansion. On the other hand, if one of those conditions is clearly exceeded, we potentially violate unitarity within our calculation and we should not trust the finite perturbative expansion anymore.

If the latter case arises at a certain high energy scale in a tree level calculation, there are two ways to fix this problem.

⁴Actually, the normalization is just chosen to exactly cancel the kinematic factor in Eq. (3.31), as was demonstrated in Ref. [18].

⁵We will perform this procedure in the analysis of Section 5.6.

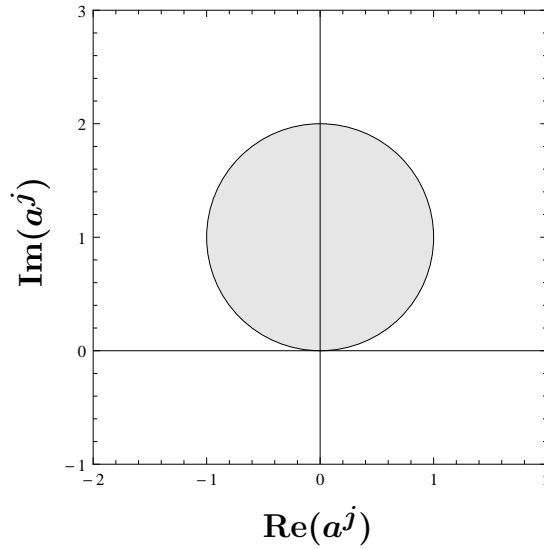


Figure 3.1.: This diagram shows the Argand circle on the complex plane for an eigenvalue a^j of the PW amplitude.

- First, we can think of a ultraviolet (UV) completion of the model that will give a more accurate description at the high energy scale or incorporates interactions that compensate the unphysical behavior. One historical example of this application is the prediction of the mass of the Higgs boson, that compensates the rising matrix element in longitudinal vector boson scattering. This example is discussed in many textbooks, e.g. see Ref. [12] for the case of longitudinal WZ scattering.⁶
- Another technique, especially used for EFT predictions, is to implement an unitarization procedure. The idea is to project the perturbatively calculated eigenvalues of the PW coefficients back on the Argand circle, if the unitarity bound in Eq. (3.40) is not satisfied. Using the projected PWs for the calculation we can at least ensure not to predict anything that clearly violates basic scattering principles like probability conservation. We do not want to go into more detail on this topic and instead refer the interested reader to the literature, e.g. see Ref. [29] for a nice review or Ref. [18] for a current application.

If we go back to our chosen EFT, we expect the dominant helicity amplitudes to rise with $\frac{s^2}{\Lambda^4}$, since we include operators of dimension 8. Using only the operator O_{T_0} , for example, the helicity amplitude \mathcal{M}_{11-1-1} for WZ scattering can be decomposed into contributions in the $j = 0$, $j = 1$ and $j = 2$ PW, which leads to

$$\begin{aligned} \mathcal{M}_{11-1-1;T_0}(WZ \rightarrow WZ) &= \frac{f_{T_0}}{8} (\cos \theta - 1)^2 (\beta^2 + 1)^2 \frac{s^2}{\Lambda^4} \\ &= 8\pi \frac{1}{\beta} \left(d_{00}^0 \frac{4}{3} \frac{f_{T_0}}{64\pi} \beta (\beta^2 + 1)^2 \frac{s^2}{\Lambda^4} + \dots \right). \end{aligned} \quad (3.41)$$

⁶Lee, Quigg and Thacker used the partial wave analysis to give a maximal bound on the mass of the physical Higgs boson, as they pointed out in their renowned paper Ref. [28].

Since the quadratic rise in $\frac{s^2}{\Lambda^4}$ will not be cured after a diagonalization with respect to the helicity space and isospin channel, this naive EFT description will not reproduce the correct high energy physical behavior of order $\sqrt{s} \gtrsim \Lambda$ using the unitarity argument in Eq. (3.40). This bound on the validity region is the expected result for our EFT, as we outlined at the end of the last section.

In order to analyze the transition from the validity region of the EFT to the regime where a more complete model gets necessary, we will in the next chapter introduce our UV complete model, which we will use for comparison in different energy regimes.

4. Ultraviolet complete toy-model

In this chapter we will introduce our ultraviolet (UV) complete model which we use to calculate the Wilson coefficients in a top-down matching of vertex corrections to the W boson vertices. The idea is to parametrize the Wilson coefficients by only a few underlying model parameters in a manner that automatically respect the necessary correlations arising from integrating out the fields. Also we are interested in the comparison of the EFT of the underlying model with the explicit one-loop vertex corrections due to new physics (NP) in the physical processes of VBS.

Historic examples, like the Euler-Heisenberg Lagrangian [30], describing effective light-by-light scattering, and the EFT description of the Hgg vertex [31], show that EFT operators involving multiple field-strength tensors are naturally obtained by integrating out corrections due to charged loop particles. This motivates us to use a model which includes new heavy particles that couple to the weak bosons through gauge interactions. Neglecting extensions of the gauge group, we propose a generic NP extension of the SM in the $SU(2)_L$ limit which serves as the underlying model of our EFT in the following.

We consider additional fermion fields Ψ with mass M_F and complex scalar fields Φ with mass M_S that transform only under a (generic) $SU(2)_L$ representation F or S respectively. We do not include any additional interaction or mixing with SM fields in order to keep our description of the relevant aspects in VBS as straight forward as possible. Therefore it is sufficient to restrict ourselves to the $SU(2)_L$ limit of the electroweak (EW) sector of the SM. As a consequence, the covariant derivative reduces to $D_\mu = \partial^\mu -igt_R^a W_\mu^a$ and the subscript R relates to the $SU(2)_L$ representation of the field on which the covariant derivative is acting. The representation R is specified by the isospin J_R , hence the multiplet comprises $2J_R + 1$ components. In principle the partial derivative ∂_μ comes along with a unit matrix in the $2J_R + 1$ -dimensional $SU(2)_L$ isospin space. We will also use the unitary limit $\xi \rightarrow \infty$ of the more general R_ξ gauge, which is valid since we are only interested in the new physics contribution at one-loop level. Thus our Lagrangian can be written as follows

$$\begin{aligned} \mathcal{L} = & \frac{1}{2} (\partial_\mu H)^2 - \frac{m_H^2}{2} H^2 - \frac{1}{2} \text{Tr} \left(\hat{W}^{\mu\nu} \hat{W}_{\mu\nu} \right) + \frac{m_W^2}{2} \left(\sum_{a=1}^3 W_\mu^a W^{a\mu} \right) \left(1 + \frac{H}{v} \right)^2 \\ & + \bar{\Psi} (i\gamma_\mu D^\mu - M_F) \Psi + (D^\mu \Phi)^\dagger D_\mu \Phi - M_S^2 \Phi^\dagger \Phi. \end{aligned} \quad (4.1)$$

The first line of Eq. (4.1) shows the relevant SM part for the physical Higgs field H and the weak boson field W . The mass term for the W and the coupling to the Higgs field follow from the Higgs mechanism. The second line involves the new fermion and scalar fields of our NP model.

Notice that we do not consider a chiral fermion coupling, but only vector coupling, so the mass term of the fermion does not break the $SU(2)_L$ symmetry and, therefore, can be

added to the Lagrangian without a dynamic process involved. Also the model can easily be generalized to multiple fermion and scalar multiplets without mass mixing.

Expanding the Lagrangian and neglecting surface terms we get

$$\begin{aligned}
\mathcal{L} = & -\frac{1}{2}H(\partial^2 + m_H^2)H + \frac{1}{2}W^a{}_\mu(g^{\mu\nu}\partial^2 - \partial^\mu\partial^\nu + m_W^2)W^a{}_\nu \\
& -\frac{1}{2}g\epsilon^{abc}(\partial_\mu W^a{}_\nu - \partial_\nu W^a{}_\mu)W^{b\mu}W^{c\nu} - \frac{1}{4}g^2\epsilon^{abn}\epsilon^{cdn}W^a{}_\mu W^b{}_\nu W^{c\mu}W^{d\nu} \\
& + \frac{m_W^2}{v}H\left(\sum_{a=1}^3 W^a{}_\mu W^{a\mu}\right) + \frac{m_W^2}{2v}H^2\left(\sum_{a=1}^3 W^a{}_\mu W^{a\mu}\right) \\
& + \bar{\Psi}(i\gamma_\mu\partial^\mu - M_F)\Psi + g\bar{\Psi}\gamma_\mu t_F^a\Psi W^{a\mu} \\
& - \Phi^\dagger(\partial^2 + M_S^2)\Phi - ig\left(\Phi^\dagger t_S^a\partial_\mu\Phi - (\partial_\mu\Phi^\dagger)t_S^a\Phi\right)W^{a\mu} + \frac{g^2}{2}\Phi^\dagger\{t_S^a, t_S^b\}\Phi W^{a\mu}W^b{}_\mu. \quad (4.2)
\end{aligned}$$

Written in this way, the Feynman rules in momentum space can be directly read of and are shown in Appendix A.2. Having the Feynman rules at hand, we are prepared to calculate one-loop corrections using the NP fields.

We note that both the fermionic and the scalar degrees of freedom are fully specified by the masses M_F and M_S and the isospin J_F and J_S , respectively.

4.1. One-loop vertex corrections

As we aim to analyse the VBS process only at the one-loop level, it is sufficient to calculate the correction for the W propagator and vertices only. In the following the fermion and scalar contributions are treated separately and their contribution to the vertex function are distinguished with a subscript F and S respectively, because we want to consider also cases where one species, fermion or scalar, is added. In the fermionic case we only have a three-particle vertex and, therefore, we only have one diagram type for each correction, whereas the scalars also have a four-particle vertex. As a consequence, there are more diagrams to consider in the scalar case. The vertex functions are regularized and calculated with the techniques discussed in Section 2.3 and Appendix A.1 and are expressed with the help of Passarino-Veltman (PV) loop functions. All the results are obtained by using the FeynCalc [24–26] tensor integral decomposition in Mathematica. We also need to consider representation factors arising from a closed loop of the fermion or scalar multiplet. As is discussed in Appendix A.2, we have to take the trace of the generators that appear in the vertices of the closed loop. The product of the generators inside the trace has to be ordered in the opposite direction of the isospin charge transport indicated by the arrows. The full analytic expressions of the vertex corrections are implemented in our VeBoS code which is described in Appendix A.5.

We start with the vacuum polarization. For the fermion case we only have one diagram, in the scalar case there is also a second diagram for the four-particle vertex. Thus we

define the propagator corrections to be

$$\text{Diagram: a wavy line with a circular loop on top} =: \tilde{\Pi}_F^{\mu\nu,ab}(p, M_F^2, J_F), \quad (4.3a)$$

$$\text{Diagram: a wavy line with a dashed circular loop on top} + \text{Diagram: a wavy line with a dashed circular loop on bottom} =: \tilde{\Pi}_S^{\mu\nu,ab}(p, M_S^2, J_S). \quad (4.3b)$$

First we have a look at the isospin factors. Each three-particle vertex comes with a $SU(2)_L$ generator in the given representation and for the four-particle vertex we have the anticommutator of two generators. As we have closed loops, the trace in the isospin space is to be taken, leading to $\text{Tr}(t_R^a t_R^b) = T_R \delta^{ab}$ for the diagrams with three-particle vertices and $\text{Tr}(\{t_R^a, t_R^b\}) = 2T_R \delta^{ab}$ for the scalar diagram involving a four-particle vertex. Here T_R is the index of the representation, normalized to be $T_R = \frac{J_R(J_R+1)(2J_R+1)}{3}$ for the case of an isospin J_R representation. As the vacuum polarization will turn out to be transverse only we can therefore write

$$\tilde{\Pi}_F^{\mu\nu,ab}(p, M_F^2, J_F) = i\delta^{ab} (p^2 g^{\mu\nu} - p^\mu p^\nu) T_F \Pi_F(p^2, M_F^2), \quad (4.4a)$$

$$\tilde{\Pi}_S^{\mu\nu,ab}(p, M_S^2, J_S) = i\delta^{ab} (p^2 g^{\mu\nu} - p^\mu p^\nu) T_S \Pi_S(p^2, M_S^2). \quad (4.4b)$$

The next step is the calculation of the three-boson vertex. For the scalar case we again have two different types of diagrams. So we define the three-boson vertex corrections

$$\left(\text{Diagram: triangle with wavy lines} + \text{perm.} \right) =: \tilde{\Gamma}_{3,F}^{\mu\nu\rho,abc}(p_1, p_2, p_3, M_F^2, J_F), \quad (4.5a)$$

$$\left(\text{Diagram: triangle with dashed wavy lines} + \text{perm.} \right) + \left(\text{Diagram: bubble with dashed wavy lines} + \text{perm.} \right) =: \tilde{\Gamma}_{3,S}^{\mu\nu\rho,abc}(p_1, p_2, p_3, M_S^2, J_S), \quad (4.5b)$$

where in the triangle diagrams we add together the permutations of two external bosons, and in the bubble-type diagrams relevant for the scalar multiplets only we, in principle, have to respect all three possible positions for the four-boson vertex. But it turns out, that these diagrams individually vanish as their combination of PV functions is identically zero. Also we would have a trace in isospin space of the form $\text{Tr}(t_R^a \{t_R^b, t_R^c\})$ which is zero for generators of the $SU(2)_L$. The sum of both triangle-diagram permutations gives a representation factor from a trace of three generators with a commutator inside¹, namely $\text{Tr}(t_R^a [t_R^b, t_R^c]) = iT_R \epsilon^{abc}$. So we may rewrite

$$\tilde{\Gamma}_{3,F}^{\mu\nu\rho,abc}(p_1, p_2, p_3, M_F^2, J_F) = i\epsilon^{abc} T_F \Gamma_{3,F}^{\mu\nu\rho}(p_1, p_2, p_3, M_F^2), \quad (4.6a)$$

$$\tilde{\Gamma}_{3,S}^{\mu\nu\rho,abc}(p_1, p_2, p_3, M_S^2, J_S) = i\epsilon^{abc} T_S \Gamma_{3,S}^{\mu\nu\rho}(p_1, p_2, p_3, M_S^2). \quad (4.6b)$$

¹The permuted diagram can be seen as the charge conjugated diagram, hence having inverted loop particle propagation. The resulting expression is given by the original diagram result just with a negative sign and two $SU(2)_L$ generators interchanged.

For the four W vertex correction, there are four different types of scalar loop diagrams. There is the box-type diagram, two triangle-type diagrams and a bubble-type diagram. Therefore the total vertex correction is

$$\left(\text{Box diagram} + \text{perm.} \right) = \tilde{\Gamma}_{4,F}^{\mu\nu\alpha\beta,abcd}(p_1, p_2, p_3, p_4, M_F^2, J_F), \quad (4.7a)$$

$$\left(\text{Triangle diagrams} + \text{perm.} \right) + \left(\text{Bubble diagram} + t\&u\text{-type} \right) = \tilde{\Gamma}_{4,S}^{\mu\nu\alpha\beta,abcd}(p_1, p_2, p_3, p_4, M_S^2, J_S). \quad (4.7b)$$

The triangle-type diagrams can be distinguished by focusing on one particle, e.g. the upper incoming one, where the diagrams are grouped due to the particle's participation in the four-particle vertex. For each of those diagrams and also for the box there are six permutations to consider, which are obtained by fixing one external particle and permuting the position of the other three. The bubble diagrams come as an s -, t - and u -type diagram. For each diagram we will get a trace over four generators which results in

$$\begin{aligned} \text{Tr} \left(t_R^a t_R^b t_R^c t_R^d \right) &= \frac{1}{15} T_R (3C_{2,R} - 1) \left(\delta^{ab} \delta^{cd} + \delta^{ac} \delta^{bd} + \delta^{ad} \delta^{bc} \right) \\ &+ \frac{1}{6} T_R \left(\delta^{ab} \delta^{cd} - 2\delta^{ac} \delta^{bd} + \delta^{ad} \delta^{bc} \right), \end{aligned} \quad (4.8)$$

as is shown in Eq. (A.38). Therein the quadratic casimir of a representation of the $SU(2)_L$ is introduced, which is defined by $C_{2,R} = J_R(J_R + 1)$. We could now in principle separate between an anomalous isospin symmetric part² proportional to $\frac{T_R}{15}(3C_{2,R} - 1)$ and terms

²This will be the only contribution for a pure $ZZ \rightarrow ZZ$ scattering, as every other contribution is coming along with epsilon tensors and will vanish for all $SU(2)_L$ adjoint isospin indices being the same. This representation factor is quite small for doublet fields with $\frac{T_d}{15}(3C_{2,d} - 1) = \frac{1}{24}$ in comparison to an 11-plet ($J_R = 5$) with $\frac{T_{11}}{15}(3C_{2,11} - 1) = 652 + \frac{2}{3}$ which will be used in Section 5 and after.

coming from products of ϵ tensors, such that

$$\begin{aligned} \tilde{\Gamma}_{4,F}^{\mu\nu\alpha\beta,abcd}(p_1, p_2, p_3, p_4, M_F^2, J_F) =: \\ \frac{1}{15} T_F (3C_{2,F} - 1) \left(\delta^{ab} \delta^{cd} + \delta^{ac} \delta^{bd} + \delta^{ad} \delta^{bc} \right) \Gamma_{4,F,symm}^{\mu\nu\alpha\beta}(p_1, p_2, p_3, p_4, M_F^2) \\ + \frac{1}{6} T_F \Gamma_{4,F,\epsilon}^{\mu\nu\alpha\beta,abcd}(p_1, p_2, p_3, p_4, M_F^2), \end{aligned} \quad (4.9a)$$

$$\begin{aligned} \tilde{\Gamma}_{4,S}^{\mu\nu\alpha\beta,abcd}(p_1, p_2, p_3, p_4, M_S^2, J_S) =: \\ \frac{1}{15} T_S (3C_{2,S} - 1) \left(\delta^{ab} \delta^{cd} + \delta^{ac} \delta^{bd} + \delta^{ad} \delta^{bc} \right) \Gamma_{4,S,symm}^{\mu\nu\alpha\beta}(p_1, p_2, p_3, p_4, M_S^2) \\ + \frac{1}{6} T_S \Gamma_{4,S,\epsilon}^{\mu\nu\alpha\beta,abcd}(p_1, p_2, p_3, p_4, M_S^2). \end{aligned} \quad (4.9b)$$

However, since this will also not result in a very simple expression, we write

$$\begin{aligned} \tilde{\Gamma}_{4,F}^{\mu\nu\alpha\beta,abcd}(p_1, p_2, p_3, p_4, M_F^2, J_F) =: T_F \left(\delta^{ab} \delta^{cd} \Gamma_{4,F,1}^{\mu\nu\alpha\beta}(p_1, p_2, p_3, p_4, M_F^2, C_{2,F}) \right. \\ \left. + \delta^{ac} \delta^{bd} \Gamma_{4,F,2}^{\mu\nu\alpha\beta}(p_1, p_2, p_3, p_4, M_F^2, C_{2,F}) + \delta^{ad} \delta^{bc} \Gamma_{4,F,3}^{\mu\nu\alpha\beta}(p_1, p_2, p_3, p_4, M_F^2, C_{2,F}) \right), \end{aligned} \quad (4.10a)$$

$$\begin{aligned} \tilde{\Gamma}_{4,S}^{\mu\nu\alpha\beta,abcd}(p_1, p_2, p_3, p_4, M_S^2, J_S) =: T_S \left(\delta^{ab} \delta^{cd} \Gamma_{4,S,1}^{\mu\nu\alpha\beta}(p_1, p_2, p_3, p_4, M_S^2, C_{2,S}) \right. \\ \left. + \delta^{ac} \delta^{bd} \Gamma_{4,S,2}^{\mu\nu\alpha\beta}(p_1, p_2, p_3, p_4, M_S^2, C_{2,S}) + \delta^{ad} \delta^{bc} \Gamma_{4,S,3}^{\mu\nu\alpha\beta}(p_1, p_2, p_3, p_4, M_S^2, C_{2,S}) \right), \end{aligned} \quad (4.10b)$$

which resembles the form in the VeBoS code.³

It should be obvious, as all the representation factors come in front of the vertex corrections, that the calculation can be separately performed for the terms coming with T_R only and those with $C_{2,R} T_R$. This way we can numerically calculate those contributions for fixed masses and efficiently reconstruct various representations, i.e. different isospins, to simplify the numerics in phenomenological analysis. We implemented this option in VeBoS as described in Appendix A.5. We exploited this possibility in our analysis in Chapter 5 and subsequent implementation in VBFNL0 which is explained in Section 6.1.

4.2. Renormalization

Because the propagator and vertex corrections contain UV divergences, we still need to renormalize our theory. As we include only corrections to the W vertices, the necessary renormalization with respect to the NP contribution only affects the field-strength tensor and coupling renormalization.

³Nevertheless, the previous form can be recovered by subtracting the four-boson vertex correction with $C_{2,R} = 0$ from the full calculation. The result is given by $\frac{1}{15} T_R 3C_{2,R} (\delta^{ab} \delta^{cd} + \delta^{ac} \delta^{bd} + \delta^{ad} \delta^{bc}) \Gamma_{4,R,symm}(\dots)$. Setting $C_{2,R} \rightarrow C_{2,R} - \frac{1}{3}$ gives the isospin-symmetric part of the vertex correction.

$$\left[\text{Diagram} \right]_{SM} = \left(\delta_g + \frac{3}{2} \delta_3 \right) \left[\text{Diagram} \right]_{SM} \quad (4.16)$$

$$\left[\text{Diagram} \right]_{SM} = 2(\delta_g + \delta_3) \left[\text{Diagram} \right]_{SM} \quad (4.17)$$

Using the modified minimal subtraction (\overline{MS}) scheme, the strategy is to calculate δ_3 from the divergent part of the vacuum polarization and subsequently determine δ_g from the divergent part of the triangle which is not absorbed within the $\frac{3}{2}\delta_3$ contribution. Afterwards we have to check whether the estimated counter-term values in the four vertex also cancel the divergent part of the box calculation. The divergent parts of the loop integrals are obtained by Table A.1.

We will directly evaluate the counter terms for an unspecified number of NP multiplets, such that we are free to restrict the result to our chosen analysis afterwards. From the vacuum polarization we have to fulfill

$$\left[\text{Diagrams} \right]_{\text{Div}} + \text{Diagram} = 0. \quad (4.18)$$

This leads to

$$\delta_3 = -g^2 \Delta_\epsilon \left(\sum_F n_F \frac{T_F}{12\pi^2} + \sum_S n_S \frac{T_S}{48\pi^2} \right), \quad (4.19)$$

where $\Delta_\epsilon = \frac{1}{\epsilon} - \gamma_E + \log(4\pi)$ contains the pole from setting $d \rightarrow 4 - 2\epsilon$. In the next step we look for the cancellation of UV divergences in the three-boson vertex

$$\left[\text{Diagrams} \right]_{\text{Div}} + \text{Diagram} = 0. \quad (4.20)$$

We obtain

$$\begin{aligned} \left(\delta_g + \frac{3}{2} \delta_3 \right) &= -g^2 \Delta_\epsilon \left(\sum_F n_F \frac{T_F}{12\pi^2} + \sum_S n_S \frac{T_S}{48\pi^2} \right) \\ \Leftrightarrow \delta_g &= -\frac{1}{2} \delta_3 = \frac{g^2}{2} \Delta_\epsilon \left(\sum_F n_F \frac{T_F}{12\pi^2} + \sum_S n_S \frac{T_S}{48\pi^2} \right). \end{aligned} \quad (4.21)$$

Finally we check for the cancellation of UV divergences four-boson vertex

$$\begin{aligned} & \left[\left(\begin{array}{c} \text{Diagram 1} + \text{Diagram 2} + \text{Diagram 3} + \text{Diagram 4} + \text{perm.} \end{array} \right) \right. \\ & \left. + \left(\begin{array}{c} \text{Diagram 5} + t\&u\text{-type} \end{array} \right) \right]_{\text{Div}} + \text{Diagram 6} = 0. \end{aligned} \quad (4.22)$$

This results in

$$2(\delta_g + \delta_3) = \delta_3 = -g^2 \Delta_\epsilon \left(\sum_F n_F \frac{T_F}{12\pi^2} + \sum_S n_S \frac{T_S}{48\pi^2} \right), \quad (4.23)$$

which is already satisfied through Eqs. (4.19) and (4.21). This is the expected result, since the only way to have a gauge invariant Lagrangian only containing field-strength tensors is that all terms are proportional to $\text{Tr}(\hat{W}^{\mu\nu} \hat{W}_{\mu\nu})$, which implies that

$$\mathcal{L}' = -\frac{1}{4} W_0^a{}_{\mu\nu} W_0^{a\mu\nu} = -\frac{1}{2} \text{Tr}(\hat{W}_0^{\mu\nu} \hat{W}_{0\mu\nu}) = -\frac{1}{2} \text{Tr}(\hat{W}^{\mu\nu} \hat{W}_{\mu\nu}) - \frac{Z_3 - 1}{2} \text{Tr}(\hat{W}^{\mu\nu} \hat{W}_{\mu\nu}). \quad (4.24)$$

4.3. Matching of Wilson coefficients

At this point, as the discussion for the full one-loop calculation is completed, we can turn our attention to the top-down matching of the EFT Wilson coefficients using our NP model. We assume our fermions and scalars to be heavy in comparison to the energy scale of the physics we want to describe. As a consequence we can effectively interpret the NP particle masses as our expansion parameter Λ of the EFT for energies of $\sqrt{s} \ll M_{F/S} \sim \Lambda$. In any on-shell $2 \rightarrow 2$ process, the same hierarchy also holds for all products of external momenta involved, say $p_i \cdot p_j \ll M_{F/S}^2$. Analogously to the expansion of the EFT Lagrangian, we can now expand our results for propagator and vertex corrections in powers of $\frac{1}{M_{F/S}}$ what will give us an approximation of the full one-loop vertex for low energies. Comparing terms

arising at the order of $\mathcal{O}(\frac{1}{\Lambda^n})$ in the effective vertices with the terms of the same order of $\mathcal{O}(\frac{1}{M_{F/S}^n})$ in the one-loop vertices, the Wilson coefficients can be determined.

As the expansion of the vertex corrections in terms of PV functions is not straight forward, we used the approach presented in Appendix A.1.1 to expand to the overall order of $\mathcal{O}(\frac{1}{M_{F/S}^4})$. After performing the Feynman parameter integration and summing all contributing diagrams, the final expansion is obtained by taking the limit $d \rightarrow 4 - 2\epsilon$. This procedure is performed with the use of FeynCalc [24–26] and Mathematica.

We identify the coefficients of the operators from $\Pi_{EFT} = [\Pi_{F/S}]_{\frac{p_i \cdot p_j}{M^2} \ll 1}$, which results in

$$f_{WW} = [-g^2] \left(\sum_F n_F \frac{T_F}{24\pi^2} \left(\Delta_\epsilon - \log \left(\frac{M_F^2}{\mu^2} \right) \right) + \sum_S n_S \frac{T_S}{96\pi^2} \left(\Delta_\epsilon - \log \left(\frac{M_S^2}{\mu^2} \right) \right) \right), \quad (4.25)$$

$$\frac{f_{DW}}{\Lambda^2} = [-g^2] \left(\sum_F n_F \frac{T_F}{120\pi^2 M_F^2} + \sum_S n_S \frac{T_S}{960\pi^2 M_S^2} \right), \quad (4.26)$$

$$\frac{f_{D2W}}{\Lambda^4} = [-g^2] \left(\sum_F n_F \frac{T_F}{1120\pi^2 M_F^4} + \sum_S n_S \frac{T_S}{13440\pi^2 M_S^4} \right), \quad (4.27)$$

where we again present the results for the general case of several multiplets, i.e. we sum over F and S .⁵ At this point we can observe, that in the case of $\mu = M_F = M_S$, f_{WW} corresponds precisely to the divergent part of the vertex corrections which is absorbed in the counterterm δ_3 in the \overline{MS} scheme, as

$$[-2f_{WW}]_{\mu=M_F=M_S} = g^2 \Delta_\epsilon \left(\sum_F n_F \frac{T_F}{12\pi^2} + \sum_S n_S \frac{T_S}{48\pi^2} \right) = -\delta_3. \quad (4.28)$$

As a consequence, for $\mu = M_F = M_S$ we have no finite correction to f_{WW} , which is practically an on-shell scheme for the momentum independent part of the WW vertex.

In the next step we insert those Wilson coefficients into the three-boson effective coupling and identify $\Gamma_{3,EFT}^{\mu\nu\rho} = [T_{F/S}\Gamma_{3,F/S}^{\mu\nu\rho}]_{\frac{p_i \cdot p_j}{M^2} \ll 1}$. This leads to

$$\frac{f_{WWW}}{\Lambda^2} = [ig^3] \left(\sum_F n_F \frac{13T_F}{360\pi^2 M_F^2} + \sum_S n_S \frac{T_S}{360\pi^2 M_S^2} \right), \quad (4.29)$$

$$\frac{f_{DWWW_0}}{\Lambda^4} = [ig^3] \left(\sum_F n_F \frac{2T_F}{105\pi^2 M_F^4} + \sum_S n_S \frac{T_S}{1120\pi^2 M_S^4} \right), \quad (4.30)$$

$$\frac{f_{DWWW_1}}{\Lambda^4} = [ig^3] \left(\sum_F n_F \frac{T_F}{630\pi^2 M_F^4} + \sum_S n_S \frac{T_S}{4032\pi^2 M_S^4} \right). \quad (4.31)$$

⁵The coefficients of powers in $(ig)^n$ in the square brackets, follow from the field-strength tensor convention $\hat{W}^{\mu\nu} = \frac{1}{-ig} [\hat{D}^\mu, \hat{D}^\nu]$ and sign convention of the coupling constant g . For the easier translation into other conventions, i.e. when using no $\frac{1}{-ig}$ normalization, those factors are taken out in front.

Parameters	limit
$\frac{f_{WWW}}{i\Lambda^2}$	$[-0.45, 0.44] \text{ TeV}^{-2}$
$\frac{f_{T_0}}{\Lambda^4}$	$[-0.75, 0.81] \text{ TeV}^{-4}$
$\frac{f_{T_1}}{\Lambda^4}$	$[-0.49, 0.55] \text{ TeV}^{-4}$
$\frac{f_{T_2}}{\Lambda^4}$	$[-1.49, 1.85] \text{ TeV}^{-4}$

Table 4.1.: Experimental bounds on aTGCs and aQGCs. The values for aTGCs are taken from Ref. [32] and for aQGCs from Ref. [6].

Proceeding the same way with the four-boson vertex $\Gamma_{4,EFT}^{\mu\nu\rho\sigma,abcd} = \left[\tilde{\Gamma}_{4,F/S}^{\mu\nu\alpha\beta,abcd} \right]_{\frac{p_i \cdot p_j}{M^2} \ll 1}$, we obtain

$$\frac{f_{T_0}}{\Lambda^4} = [g^4] \left(\sum_F n_F \frac{(-14C_{2,F} + 1) T_F}{10080\pi^2 M_F^4} + \sum_S n_S \frac{(7C_{2,S} - 2) T_S}{40320\pi^2 M_S^4} \right), \quad (4.32)$$

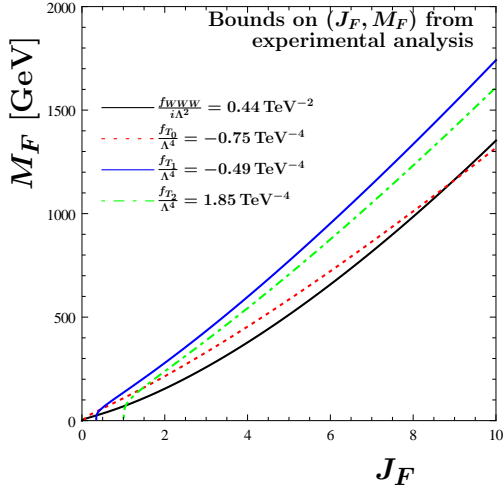
$$\frac{f_{T_1}}{\Lambda^4} = [g^4] \left(\sum_F n_F \frac{(-28C_{2,F} + 13) T_F}{10080\pi^2 M_F^4} + \sum_S n_S \frac{(14C_{2,S} - 5) T_S}{40320\pi^2 M_S^4} \right), \quad (4.33)$$

$$\frac{f_{T_2}}{\Lambda^4} = [g^4] \left(\sum_F n_F \frac{(196C_{2,F} - 397) T_F}{25200\pi^2 M_F^4} + \sum_S n_S \frac{(14C_{2,S} - 23) T_S}{50400\pi^2 M_S^4} \right), \quad (4.34)$$

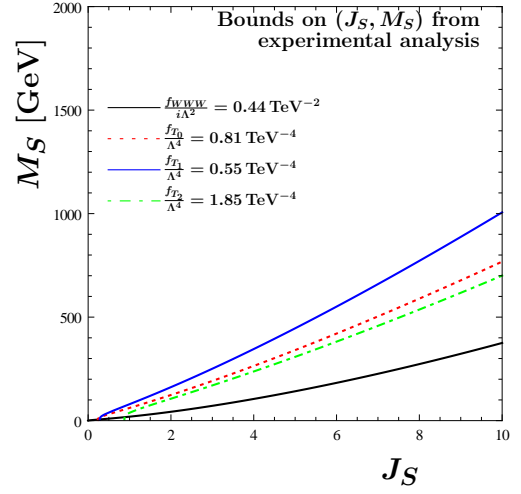
$$\frac{f_{T_3}}{\Lambda^4} = [g^4] \left(\sum_F n_F \frac{(98C_{2,F} + 299) T_F}{25200\pi^2 M_F^4} + \sum_S n_S \frac{(7C_{2,S} + 16) T_S}{50400\pi^2 M_S^4} \right). \quad (4.35)$$

We determined all the Wilson coefficients for our full EFT representation of our NP model. One interesting difference we can already see between the scalar and fermion multiplets, is that their signs of the T-operators do not always coincide, e.g. $\frac{f_{T_0}}{\Lambda^4}$ and $\frac{f_{T_1}}{\Lambda^4}$ will be negative for one single fermion multiplet whereas they are always positive values for a scalar multiplet. But we can see a sign flip from negative to positive for both cases in $\frac{f_{T_2}}{\Lambda^4}$ at $J_R \sim 1$. There is also a stronger numerical suppression in the scalar case for every Wilson coefficient.

At this point we may look for restrictions in the (J_R, M) parameter space for one single multiplet, given by experimental bounds on values for the Wilson coefficients. The values for anomalous triple-gauge couplings (aTGC) and anomalous quartic-gauge couplings (aQGC) for the comparison are listed in Table 4.1. The diagrams showing the corresponding exclusion limit are given in Fig. 4.1, where we used for the coupling parameter $g = 0.66$. We depict the minimum value of the multiplet mass for the case of a given representation of J_R . Therefore, all value pairs of (J_R, M) lying below the curve in the parameter space would be disfavored from the experimental bounds. In the scalar case a much larger J_S would be possible for a given mass M_S or, equivalently, M_S can be lower for a given J_S . This is the feature of the stronger suppression of the Wilson coefficients of the scalar model. Furthermore, in both cases the bounds on aQGCs are stricter than the bounds on aTGCs and the most stringent bound emerges from the Wilson coefficient of



(a)



(b)

Figure 4.1.: Demonstration of the experimental bounds on the (J_R, M) parameter space. We depict (a) the case of a fermion multiplet and (b) the case of a scalar multiplet. Value pairs below the curves would be disfavored by experimental analysis.

the O_{T_1} operator (solid, blue). For our purpose we will analyze the model with parameters in the vicinity of the bounds in the following discussions.

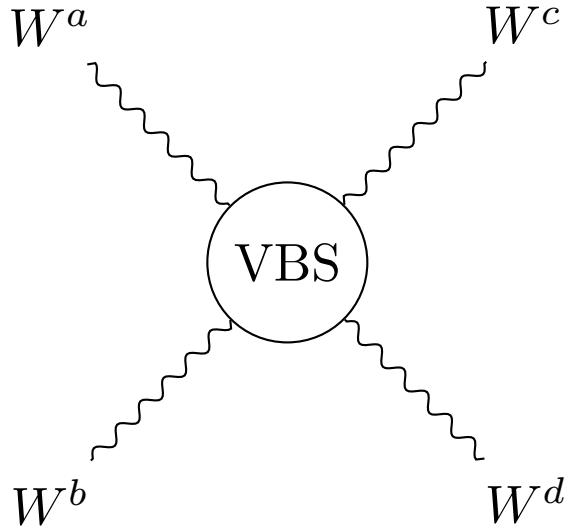


Figure 5.1.: VBS in the $SU(2)_L$ limit.

5. On-shell vector-boson scattering

After the extensive introduction of our model, its Feynman rules and the corresponding EFT representation, we proceed with the impact of our model realization on vector-boson scattering (VBS). In the first subsections we want to describe the calculation of the full on-shell process at one-loop order and define the kinematics. Then we will show results and discuss different aspects of VBS, comparing the EFT and the ultraviolet (UV) complete model. In Section 5.4 we will consider the full cross section for different VBS processes. We continue in Section 5.5 with the evaluation of several helicity amplitudes. Section 5.6 demonstrates the analysis of the partial-wave (PW) decomposition and the examination of unitarity considerations of the UV-complete model. The chapter will be closed in Section 5.7 with an accuracy estimation of the approximation of the new-physics (NP) contribution in VBS by only considering a small set of PW coefficients.

5.1. Process definition

Working in the $SU(2)_L$ limit, the on-shell process of VBS can be generally depicted as shown in the Feynman diagram of Fig. 5.1. The two incoming vector bosons W^a and W^b come from asymptotic free states and enter the interaction region depicted as the VBS

labeled blob. Two outgoing vector bosons W^c and W^d leave the interaction region into asymptotic free states. As we allow for inelastic scattering, the bosons W^c and W^d may differ from the W^a and W^b ones.

If we take a closer look into the interaction region, we can decompose the process into leading-order terms and various effects of higher-order due to additional fermions and scalars¹, as is presented in

$$\begin{aligned}
 & \text{VBS blob} = \text{tree-level exchange} + \left(\text{s-channel} + \text{t-channel} + \text{u-channel} + t\&u \text{ diag} \right) \\
 & + \left(\text{s-channel } \Pi, \Gamma_3 + \text{t-channel } \Gamma_3 + \text{u-channel } \Gamma_3 + t\&u \text{ diag} \right) \\
 & + \text{four-boson vertex } \Gamma_4 \\
 & = i \left(\mathcal{M}_1 \delta^{ab} \delta^{cd} + \mathcal{M}_2 \delta^{ac} \delta^{bd} + \mathcal{M}_3 \delta^{ad} \delta^{bc} \right). \tag{5.1}
 \end{aligned}$$

The diagrams in the first line on the right-hand side represent the tree-level SM contributions. In the second line we depicted corrections to the internal propagator and the three-boson vertex and in the last line the four-boson vertex correction. All diagrams involving an internal propagator come as an s -, t - and u -type diagram. In our discussions, the corrections are seen to follow from NP contributions only, thus coming from one-loop contributions of the new fermion or scalar multiplets or their derived EFT vertices, respectively.² The last equation follows from isospin symmetry, as the isospin combinations for four indices a_i can only be expressed in Kronecker deltas in the adjoint space, meaning that we can independently calculate the amplitudes for different isospin combinations.

If we want to associate those basic amplitudes with processes of physical particles W^\pm and Z , we can multiply the full expression in Eq. (5.1) with the corresponding isospin combinations for each external particle. So, for each Z we multiply by δ^{3a_i} , for incoming W^\pm with $\frac{1}{\sqrt{2}} (\delta^{1a_i} \pm i\delta^{2a_i})$ and for outgoing W^\pm with a factor $\frac{1}{\sqrt{2}} (\delta^{1a_i} \mp i\delta^{2a_i})$, where a_i is the isospin of the W^{a_i} that should be replaced by the physical particle. After summing over all internal a_i we get the amplitude combination for the physical process.

¹We do not perform an one-loop calculation within the SM!

²We will not include multiple insertions of EFT operators, since their contributions are negligible. This will be deduced in Section 5.3.

This procedure is demonstrated for the example of $ZZ \rightarrow W^+W^-$ scattering. In this case, the amplitude will be constructed with

$$\begin{aligned} \mathcal{M}(ZZ \rightarrow W^+W^-) &= \sum_{a,b,c,d=1}^3 \left(\delta^{3a}\delta^{3b} \left(\mathcal{M}_1\delta^{ab}\delta^{cd} + \mathcal{M}_2\delta^{ac}\delta^{bd} + \mathcal{M}_3\delta^{ad}\delta^{bc} \right) \right. \\ &\quad \left. \frac{1}{\sqrt{2}}(\delta^{1c} - i\delta^{2c}) \frac{1}{\sqrt{2}}(\delta^{1d} + i\delta^{2d}) \right) \\ &= \mathcal{M}_1. \end{aligned} \quad (5.2)$$

Likewise, we can reproduce the other physical processes by the basic amplitudes, leading to

$$\mathcal{M}(W^\pm W^\mp \rightarrow ZZ) = \mathcal{M}_1, \quad (5.3a)$$

$$\mathcal{M}(W^\pm Z \rightarrow W^\pm Z) = \mathcal{M}_2, \quad (5.3b)$$

$$\mathcal{M}(W^\pm Z \rightarrow ZW^\pm) = \mathcal{M}_3 = [\mathcal{M}(W^\pm Z \rightarrow W^\pm Z)]_{t \leftrightarrow u}, \quad (5.3c)$$

$$\mathcal{M}(W^\pm W^\mp \rightarrow W^\pm W^\mp) = \mathcal{M}_1 + \mathcal{M}_2, \quad (5.3d)$$

$$\mathcal{M}(W^\pm W^\mp \rightarrow W^\mp W^\pm) = \mathcal{M}_1 + \mathcal{M}_3 = [\mathcal{M}(W^\pm W^\mp \rightarrow W^\pm W^\mp)]_{t \leftrightarrow u}, \quad (5.3e)$$

$$\mathcal{M}(W^\pm W^\pm \rightarrow W^\pm W^\pm) = \mathcal{M}_2 + \mathcal{M}_3, \quad (5.3f)$$

$$\mathcal{M}(ZZ \rightarrow ZZ) = \mathcal{M}_1 + \mathcal{M}_2 + \mathcal{M}_3, \quad (5.3g)$$

where we also show the redundant combinations, which are just recovered via interchange of the kinematic variables t and u .

We can already make some predictions for the $ZZ \rightarrow ZZ$ process at this point. All the three gauge-boson vertices, even the corrected ones, carry a factor of the structure constant ϵ^{abc} . Thus, they will vanish for all external particles having $a_i = 3$. This is also true for the SM four-boson vertex. Therefore, the SM contribution will reduce to the sum of Higgs s , t and u diagrams, which is rather suppressed. All EFT vertices, except for the four-vertex part originating from T-operators, will also come with structure constants and vanish likewise. So the only relevant contribution will follow from the symmetric part of the four-boson vertex correction in Eq. (4.9), or its low energy approximation which is matched with the Wilson coefficients of the T-operators demonstrated as in Section 4.3.

5.2. Kinematics

The next step is to set up the kinematics for the calculation. In the on-shell case it is reasonable to work in the center of mass frame (COM), where the incoming and outgoing particle momenta add up to zero. As the $2 \rightarrow 2$ process happens in a plane, we are free to choose the xz -plane and take the incoming beam axis as our z axis. Therefore, the momenta of the particles are given by

$$\begin{aligned} p_1 &= \frac{\sqrt{s}}{2} (1, 0, 0, \beta), & q_1 &= \frac{\sqrt{s}}{2} (1, \beta \sin \theta, 0, \beta \cos \theta), \\ p_2 &= \frac{\sqrt{s}}{2} (1, 0, 0, -\beta), & q_2 &= \frac{\sqrt{s}}{2} (1, -\beta \sin \theta, 0, -\beta \cos \theta), \end{aligned} \quad (5.4)$$

where p_1 and p_2 are the incoming momenta and q_1 and q_2 outgoing and θ is the scattering angle between the three momenta \vec{p}_1 and \vec{q}_1 , $\cos \theta = \frac{\vec{p}_1 \cdot \vec{q}_1}{|\vec{p}_1| |\vec{q}_1|}$, and $\beta = \sqrt{1 - \frac{4m_W^2}{s}}$. In this frame the Mandelstam variables s, t, u can be expressed in terms of s, m_W and $\cos \theta$

$$s = (p_1 + p_2)^2, \quad (5.5a)$$

$$t = (p_1 - q_1)^2 = -\frac{s\beta^2}{2} (1 - \cos \theta), \quad (5.5b)$$

$$u = (p_1 - q_2)^2 = -\frac{s\beta^2}{2} (1 + \cos \theta). \quad (5.5c)$$

As discussed in the Appendix A.4 we get a set for the final helicity eigenvectors

$$\begin{aligned} \epsilon_{\pm}(p_1) &= -\frac{1}{\sqrt{2}} (0, 1, \pm i, 0), & \epsilon_0(p_1) &= \frac{\sqrt{s}}{2m_W} (\beta, 0, 0, 1), \\ \epsilon_{\pm}(p_2) &= -\frac{1}{\sqrt{2}} (0, 1, \mp i, 0), & \epsilon_0(p_2) &= \frac{\sqrt{s}}{2m_W} (\beta, 0, 0, -1), \\ \epsilon_{\pm}^*(q_1) &= -\frac{1}{\sqrt{2}} (0, \cos \theta, -\sin \theta \mp i, 0), & \epsilon_0^*(q_1) &= \frac{\sqrt{s}}{2m_W} (\beta, \sin \theta, 0, \sin \theta), \\ \epsilon_{\pm}^*(q_2) &= -\frac{1}{\sqrt{2}} (0, \cos \theta, -\sin \theta \pm i, 0), & \epsilon_0^*(q_2) &= \frac{\sqrt{s}}{2m_W} (\beta, -\sin \theta, 0, -\cos \theta), \end{aligned} \quad (5.6)$$

which we will use for the calculation of processes between helicity eigenstates.

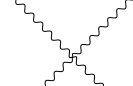
We developed the Fortran77 program VeBoS which we used in the analysis of different aspects of on-shell VBS. Further information on the program is presented in Appendix A.5. In the following sections we will discuss several results that were obtained with VeBoS.

5.3. Perturbative counting in the EFT cross-section calculation

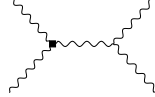
The EFT calculation involves different couplings and scales, in which a perturbative expansion can be performed. Thus, we dedicate this section to justify our choice of contributions which we include in the cross-section calculation.

The perturbative counting of the EFT calculation can be separated as follows: On the one hand, we have the energy scale Λ that serves as the EFT expansion parameter, determining the relevance of the contribution depending on the energy regime. Its effect can be estimated by a factor of $\frac{s}{\Lambda^2}$ for each insertion of a dimension 6 operator vertex and a factor of $\frac{s^2}{\Lambda^4}$ for each insertion of a dimension 8 operator vertex. On the other hand, as we have determined the Wilson coefficients of our EFT operators explicitly via one-loop matching of our NP fields, each insertion of an effective coupling is suppressed by a loop factor of $\frac{g^2}{16\pi^2}$, but also enhanced by the representation factors $T_R \sim J_R^3$ and $T_R C_{2,R} \sim J_R^5$. Moreover we include a discussion of the expected impact due to electroweak (EW) next-to leading order (NLO) corrections with a rough estimation given by a suppression of the loop factor $\frac{g^2}{16\pi^2}$. As an example, we consider different expected contributions to the amplitudes based on one insertion of O_{WW} , one insertion of a T-operator O_{T_i} , two insertions of

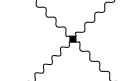
O_{WWW} , the pure SM EW NLO correction, the EW NLO correction with one insertion of O_{T_i} . To further clarify the notation used in this section, we show example Feynman diagrams and the approximated contribution factors associated with each Feynman diagram due to the above mentioned arguments in the following:



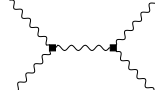
$$\in \mathcal{M}_{SM} \sim g^2, \quad (5.7a)$$



$$\in \mathcal{M}_{f_{WWW}} \sim g^2 \frac{g^2}{16\pi^2} \frac{s}{\Lambda^2} J_R^3, \quad (5.7b)$$



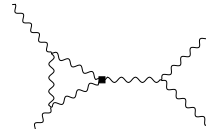
$$\in \mathcal{M}_{f_{T_i}} \sim g^2 \frac{g^2}{16\pi^2} \frac{s^2}{\Lambda^4} J_R^5, \quad (5.7c)$$



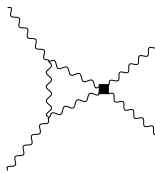
$$\in \mathcal{M}_{f_{WWW}^2} \sim g^2 \left(\frac{g^2}{16\pi^2} \right)^2 \frac{s^2}{\Lambda^4} J_R^6, \quad (5.7d)$$



$$\in \mathcal{M}_{SM}^{NLO} \sim g^2 \frac{g^2}{16\pi^2}, \quad (5.7e)$$



$$\in \mathcal{M}_{f_{WWW}}^{NLO} \sim g^2 \left(\frac{g^2}{16\pi^2} \right)^2 \frac{s}{\Lambda^2} J_R^3, \quad (5.7f)$$



$$\in \mathcal{M}_{f_{T_i}}^{NLO} \sim g^2 \left(\frac{g^2}{16\pi^2} \right)^2 \frac{s^2}{\Lambda^4} J_R^5. \quad (5.7g)$$

In the presented Feynman diagrams, the vertex denoted by a filled square corresponds to the insertion of the EFT vertex. If we want to estimate the impact of each anomalous amplitude in the cross section, we consider the contribution at the level of the interference term with the SM, which is given by $2\text{Re}(\mathcal{M}_{SM}\mathcal{M}_i)$, and at the level of the anomalous squared piece $|\mathcal{M}_i|^2$. The resulting additional factors³ for each contribution in the cross section are given in Table 5.1, where we also highlight explicit values using parameters of an underlying fermion multiplet model with ($J_F = 5$, $M_F = 750$ GeV) and inserting explicit COM energies \sqrt{s} for the lower and upper bound of the expected validity region of the EFT.

³The overall factor of g^4 is omitted, since it is proportional to the SM cross section and enters in each contribution. Therefore, we will only look at the additional factors for a better distinction.

5. On-shell vector-boson scattering

\mathcal{M}_i	$2\text{Re}(\mathcal{M}_{SM}\mathcal{M}_i)$	$\frac{s}{\Lambda^2} \rightarrow [\frac{(2m_W)^2}{M_F^2}, 1]$	$ \mathcal{M}_i ^2$	$\frac{s}{\Lambda^2} \rightarrow [\frac{(2m_W)^2}{M_F^2}, 1]$
$\mathcal{M}_{f_{WWW}}$	$\frac{g^2}{16\pi^2} \frac{s}{\Lambda^2} J_R^3$	[0.01616, 0.34481]	$\left(\frac{g^2}{16\pi^2}\right)^2 \frac{s^2}{\Lambda^4} J_R^6$	[0.00026, 0.11889]
$\mathcal{M}_{f_{Ti}}$	$\frac{g^2}{16\pi^2} \frac{s^2}{\Lambda^4} J_R^5$	[0.01893, 8.62022]	$\left(\frac{g^2}{16\pi^2}\right)^2 \frac{s^4}{\Lambda^8} J_R^{10}$	[0.00036, 74.3081]
$\mathcal{M}_{f_{WWW}^2}$	$\left(\frac{g^2}{16\pi^2}\right)^2 \frac{s^2}{\Lambda^4} J_R^6$	[0.00026, 0.11889]	$\left(\frac{g^2}{16\pi^2}\right)^4 \frac{s^4}{\Lambda^8} J_R^{12}$	[$6.8 \cdot 10^{-8}$, 0.01414]
\mathcal{M}_{SM}^{NLO}	$\frac{g^2}{16\pi^2}$	[0.00276, 0.00276]	$\left(\frac{g^2}{16\pi^2}\right)^2$	[$7.6 \cdot 10^{-6}$, $7.6 \cdot 10^{-6}$]
$\mathcal{M}_{f_{WWW}}^{NLO}$	$\left(\frac{g^2}{16\pi^2}\right)^2 \frac{s}{\Lambda^2} J_R^3$	[0.00004, 0.00095]	$\left(\frac{g^2}{16\pi^2}\right)^4 \frac{s^2}{\Lambda^4} J_R^6$	[$2.0 \cdot 10^{-9}$, $9.0 \cdot 10^{-7}$]
$\mathcal{M}_{f_{Ti}}^{NLO}$	$\left(\frac{g^2}{16\pi^2}\right)^2 \frac{s^2}{\Lambda^4} J_R^5$	[0.00005, 0.02378]	$\left(\frac{g^2}{16\pi^2}\right)^4 \frac{s^4}{\Lambda^8} J_R^{10}$	[$2.7 \cdot 10^{-9}$, 0.00057]

Table 5.1.: Counting of additional factors in EFT perturbative expansion of the cross section arising from one-loop calculation/matching (factor $\frac{g^2}{16\pi^2}$) and EFT expansion (factor $\frac{s}{\Lambda^2}$). The powers of isospin J_R follow from the representation factor of the NP fields, leading to an enhanced coupling and, therefore, enhanced contribution to the cross section. The explicit values are estimated for $g = 0.66$, $J_R = J_F = 5$, $\Lambda = M_F = 750$ GeV and the estimated limits of the EFT validity region given by the kinematic threshold $s = (2m_W)^2$ as lower bound and the NP energy scale Λ as higher bound.

It is obvious, when we calculate a cross section in the low-energy regime, i.e. $2m_W \leq \sqrt{s} \ll \Lambda$, the dominant anomalous contribution will follow from the interference term with single insertion of the EFT vertices, i.e. $2\text{Re}(\mathcal{M}_{SM}\mathcal{M}_{f_{WWW}})$ and $2\text{Re}(\mathcal{M}_{SM}\mathcal{M}_{f_{Ti}})$. The next relevant term would be the interference term of the pure SM EW NLO correction which is about an order of magnitude suppressed, as it does not involve a representation enhancement. Therefore, it will not be considered in our calculation. All other contributions are not of relevance at low energies, since they are further suppressed. In the high-energy regime of the expected validity region of the EFT, the dominant contribution follow from the anomalous squared piece of the T-operators, i.e. $|\mathcal{M}_{Ti}|^2$, followed by the interference term of the T-operators, i.e. $2\text{Re}(\mathcal{M}_{SM}\mathcal{M}_{f_{Ti}})$. Other contributions are negligible.

Considering these observations, we decide to include in the subsequent sections only single insertions of the EFT vertices and analyze the cross section at the level of adding only the interference term as anomalous contribution in comparison with adding the full anomalous amplitude squared as well. We evaluate in which energy region the dimension 6 operators dominate and in which regime the T-operators give an accurate approximation of the full EFT calculation. One could argue, that when we include the anomalous squared piece of $|\mathcal{M}_{f_{WWW}}|^2$, we could as well include the interference term of the double inserted EFT vertex, i.e. $2\text{Re}(\mathcal{M}_{SM}\mathcal{M}_{f_{WWW}^2})$. But, using the reasoning above, both contributions are not of relevance throughout the whole energy range.

To summarize, we only include single insertions of the EFT operators in the tree-level amplitude, but then consider not only the interference with the SM, but also the square of the anomalous amplitude itself. This corresponds to the contributions given in the first two lines in Table 5.1. Thus, the EFT calculation will follow the full one-loop calculation of

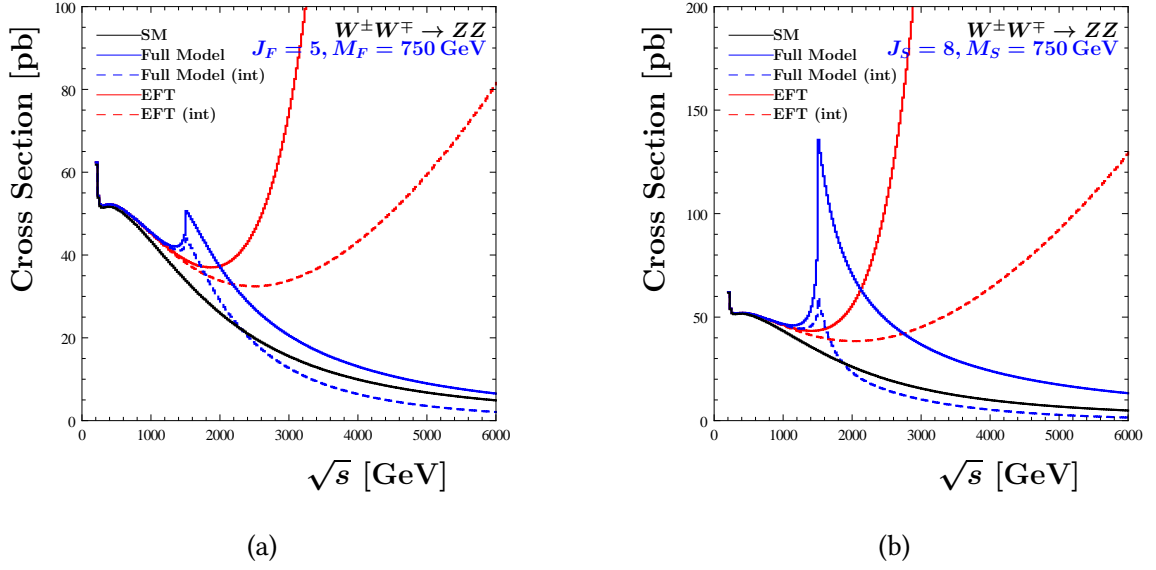


Figure 5.2.: Cross section summed and averaged over polarizations as a function of the COM energy \sqrt{s} for $WW \rightarrow ZZ$ scattering in the case of (a) one new fermion multiplet ($J_F = 5, M_F = 750$ GeV) or (b) one new scalar multiplet ($J_S = 8, M_S = 750$ GeV). Dashed lines correspond to cross sections, where only the interference term of SM and anomalous part is included as the NP contribution (i.e. $|\mathcal{M}_{SM}|^2 + 2\text{Re}(\mathcal{M}_{SM}\mathcal{M}_{\text{anom}}^*)$), whereas solid lines represent the cross section, where the full absolute squared of the amplitude (i.e. $|\mathcal{M}_{SM} + \mathcal{M}_{\text{anom}}|^2$) is considered.

the NP fields approximating each loop correction as a single EFT vertex in the low-energy limit.

5.4. On-shell cross section

In this section we examine the result for the total cross section σ . But first, we have to specify the model parameter we used in the calculation. Following the idea mentioned in Section 4.3 we used parameters such that the Wilson coefficients of the EFT fall in the vicinity of the bound given by experimental collaborations. Thus, a natural model choice is one single fermion or scalar multiplet with a value pair (J_R, M_R) according to the boundary in Fig. 4.1. In the subsequent analysis we will focus on a multiplet with mass $M = 750$ GeV and, hence, a fermion multiplet with isospin $J_F = 5$ or a scalar multiplet $J_S = 8$, respectively. The relevant SM parameters throughout this section are $v = 246$ GeV and $g = 0.66$, which results in $m_W = 81.18$ GeV.

Additionally, we impose a cut on the scattering angle, so we include for the angular integration $\sigma = \int d\cos\theta \frac{d\sigma}{d\cos\theta}$ only scattering angles of $5^\circ < \theta < 175^\circ$. This cut while drastically reducing the SM contribution from small angles in the t - and u -channel diagrams highlights the NP contribution.

In Fig. 5.2 we present the result for σ as a function of the COM energy $\sqrt{s} = m_{ZZ}$ for the processes $WW \rightarrow ZZ$. Our figures start at $\sqrt{s} = 200$ GeV as this is well above the

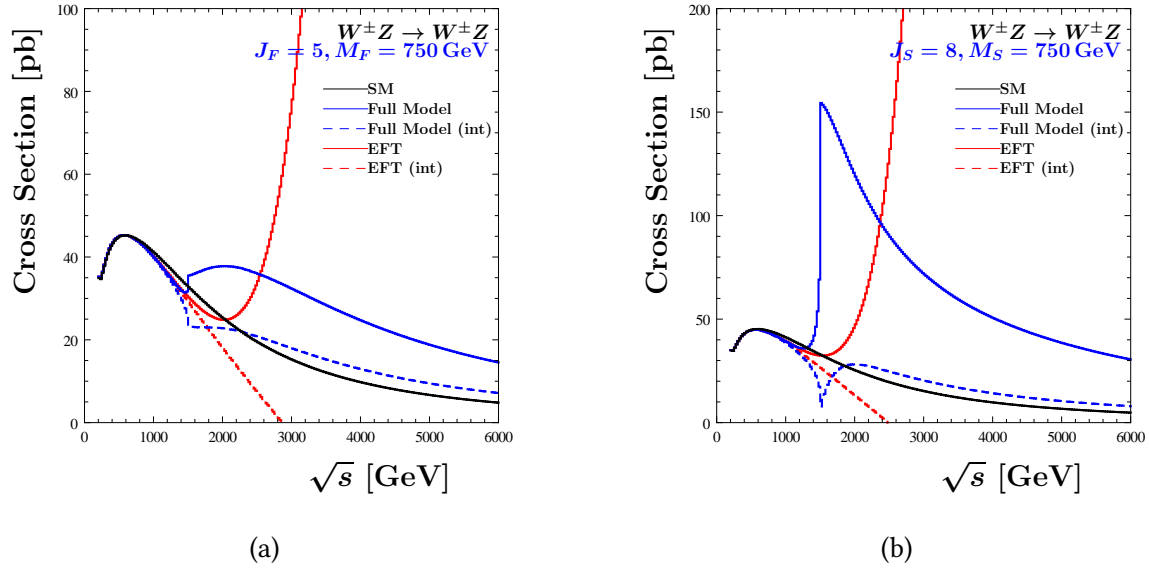


Figure 5.3.: Cross section summed and averaged over polarizations as a function of the COM energy \sqrt{s} for $WZ \rightarrow WZ$ scattering in the case of (a) one new fermion multiplet ($J_F = 5, M_F = 750$ GeV) or (b) one new scalar multiplet ($J_S = 8, M_S = 750$ GeV). Dashed lines correspond to cross sections, where only the interference term of SM and anomalous part is included as the NP contribution (i.e. $|\mathcal{M}_{SM}|^2 + 2\text{Re}(\mathcal{M}_{SM}\mathcal{M}_{\text{anom}}^*)$), whereas solid lines represent the cross section, where the full absolute squared of the amplitude (i.e. $|\mathcal{M}_{SM} + \mathcal{M}_{\text{anom}}|^2$) is considered.

kinematic threshold $\sqrt{s} = 2m_W$. On the left side we depict the fermion and on the right side the scalar contribution.

First, we want to point out that we have good accordance between loop calculation (blue) and EFT (red) for COM energies until slightly above the loop particle mass. This can be understood as an indirect check of the correctness of our EFT matching.

For energies centered around $2M = 1500$ GeV we see a clear peak structure for the loop calculation in the full model. This was expected, as it is the energy region where the particles in the loop could be pair-produced. As a consequence the loop integrals develop an imaginary part. Of course, the naive tree level EFT calculation cannot reproduce such a peak structure, so there is a huge discrepancy between the full model and the EFT cross section starting from COM energies $\sqrt{s} \sim 1000$ GeV, in particular in the vicinity of the peak. For energies well above the peak we see a flattening of the cross section in the full model loop calculation resulting in a decline almost parallel to the SM (black, solid), whereas the EFT cross section continuously rises, which would clearly violate probability conservation at one point. Another observation is that we see a relevant discrepancy between only adding the interference term between the SM and the anomalous contribution (dashed), i.e. $|\mathcal{M}_{SM}|^2 + 2\text{Re}(\mathcal{M}_{SM}\mathcal{M}_{\text{anom}}^*)$, and the full absolute squared of the amplitude $|\mathcal{M}_{SM} + \mathcal{M}_{\text{anom}}|^2$ (solid) for energies above $2M = 1500$ GeV, indicating that we might work with a model that does not converge appropriately fast in a perturbative calculation. As explained in Section 5.3 the interference with the SM corresponds to a calculation at $\mathcal{O}(g^6)$,

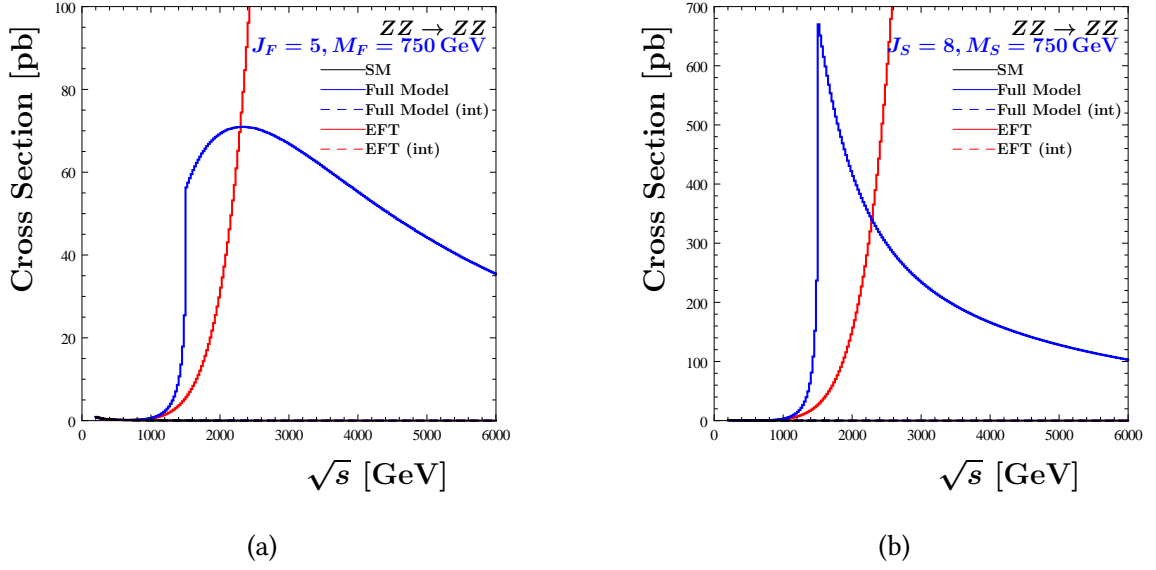


Figure 5.4.: Cross section summed and averaged over polarizations as a function of the COM energy \sqrt{s} for $ZZ \rightarrow ZZ$ scattering in the case of (a) one new fermion multiplet ($J_F = 5, M_F = 750$ GeV) or (b) one new scalar multiplet ($J_S = 8, M_S = 750$ GeV). Dashed lines correspond to cross sections, where only the interference term of SM and anomalous part is included as the NP contribution (i.e. $|\mathcal{M}_{SM}|^2 + 2\text{Re}(\mathcal{M}_{SM}\mathcal{M}_{\text{anom}}^*)$), whereas solid lines represent the cross section, where the full absolute squared of the amplitude (i.e. $|\mathcal{M}_{SM} + \mathcal{M}_{\text{anom}}|^2$) is considered.

whereas squaring the anomalous part yields $\mathcal{O}(g^8)$. A large difference between the two options is especially pronounced in the scalar case, which arises due to the much higher representation $J_S = 8$ compared to $J_F = 5$. We also want to highlight that we observe a constructive interference in this process.

We consider the process of WZ -scattering in Fig. 5.3. A clear distinction to the previous case of $WW \rightarrow ZZ$ is a destructive interference between the anomalous contribution and the SM. The interference term gives a negative contribution to the cross section for energies below ~ 2400 GeV in the fermion and ~ 2000 GeV in the scalar case, leading to a negative peak around $2M = 1500$ GeV. Since the EFT calculation extrapolates the full model low energy behavior up to arbitrary energies, we get even negative cross section values for the $\mathcal{O}(g^6)$ calculation above 3000 GeV. Nevertheless, this is an acceptable behavior, since it is well above the expected validity region of the EFT.

The process of ZZ -scattering presented in Fig. 5.4 again shows a different behavior. As was explained earlier, the SM contributions to this process are highly suppressed, leading to an almost vanishing cross section for the SM alone, i.e. $|\mathcal{M}_{SM}|^2$, and also for the interference contribution, i.e. $2\text{Re}(\mathcal{M}_{SM}\mathcal{M}_{\text{anom}}^*)$. Only the squared pure anomalous part gives a large cross section starting at energies in the vicinity of the peak, resulting in the highest cross section of all analyzed processes. It was shown in Section 4.1, that the dominant representation factor $\sim T_R C_{2,R} \sim J_R^5$ is part of the isospin symmetric term in the box calculation. In constructing the $ZZ \rightarrow ZZ$ Feynman amplitude, as described

5. On-shell vector-boson scattering

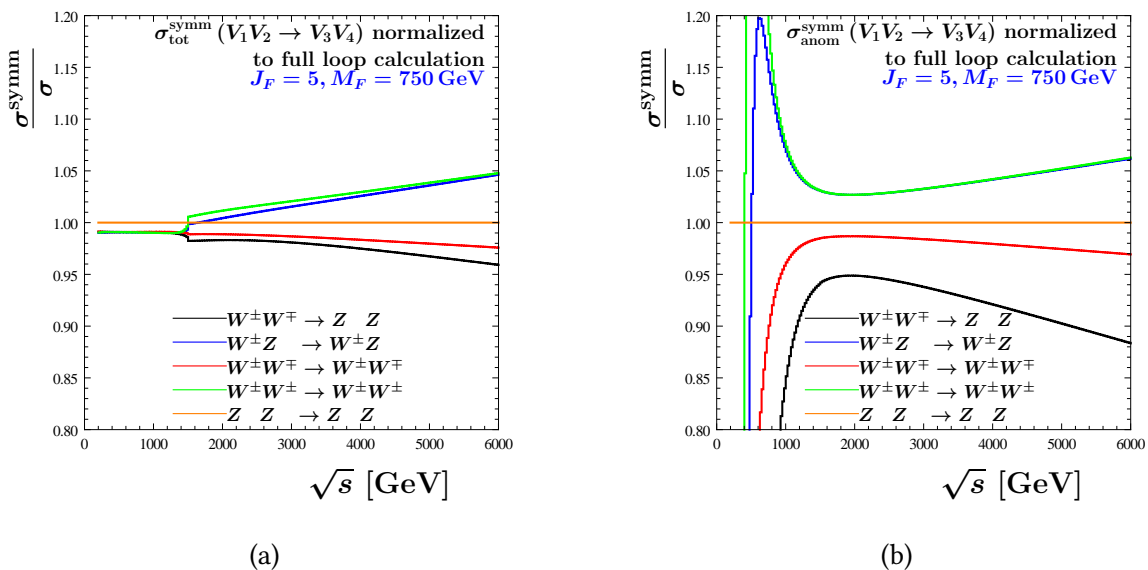


Figure 5.5.: Ratio plot for the cross section summed and averaged over helicities where the anomalous contribution of the Feynman amplitude follows from the isospin symmetric part of the four-vertex correction alone, as defined in Eq. (4.9), normalized for the case of the full one-loop correction over COM energy \sqrt{s} for all VBS channels. We depict (a) the ratio for the full cross sections and (b) the ratio for the cross sections following from the anomalous squared part of the amplitude.

in Eq. (5.3), we get this dominant term three times by summing up the basic amplitudes. Thus, $ZZ \rightarrow ZZ$ represents the strongest VBS channel for a fermionic representation as high as $J_F = 5$.

Since the scalar calculation behaves qualitatively similar to the fermionic case, we will restrict the following discussion to the fermion multiplet case only and present the scalar results just when qualitative differences occur. We will also use the full amplitude squared $|\mathcal{M}_{SM} + \mathcal{M}_{\text{anom}}|^2$ in the subsequent cross-section calculations for a better comparison with the VBFNLO [8–10] results in Chapter 6, since the anomalous contributions for VBS in VBFNLO also enter at this order.

Subsequently, we estimate which vertex corrections depicted in Eq. (5.1) gives the dominant contribution to the anomalous part of the amplitude. We therefore present in Fig. 5.5 the comparison of the cross section summed over helicities as it arises from adding the isospin symmetric part of the box calculation, defined in Eq. (4.9), as the only anomalous contribution to the amplitude with the full one-loop corrected calculation. The isospin symmetric part of the box calculation is chosen, as it gathers the strongest enhancement due to representation factors $T_{RC_{2,R}} \sim J_R^5$ for a representation of $J_F = 5$. Fig. 5.5 (a) clearly shows, that adding only the anomalous part purely arising from the isospin symmetric part of the box calculation to the amplitude is in good accordance with the full result for all VBS channels, as the deviation is $< 5\%$ over the whole energy range. In the case of ZZ scattering it even reproduces the exact result, as was explained in Section 5.1. However, in the other VBS channels the low energy regime below the peak, namely $\sqrt{s} < 1500$ GeV, is

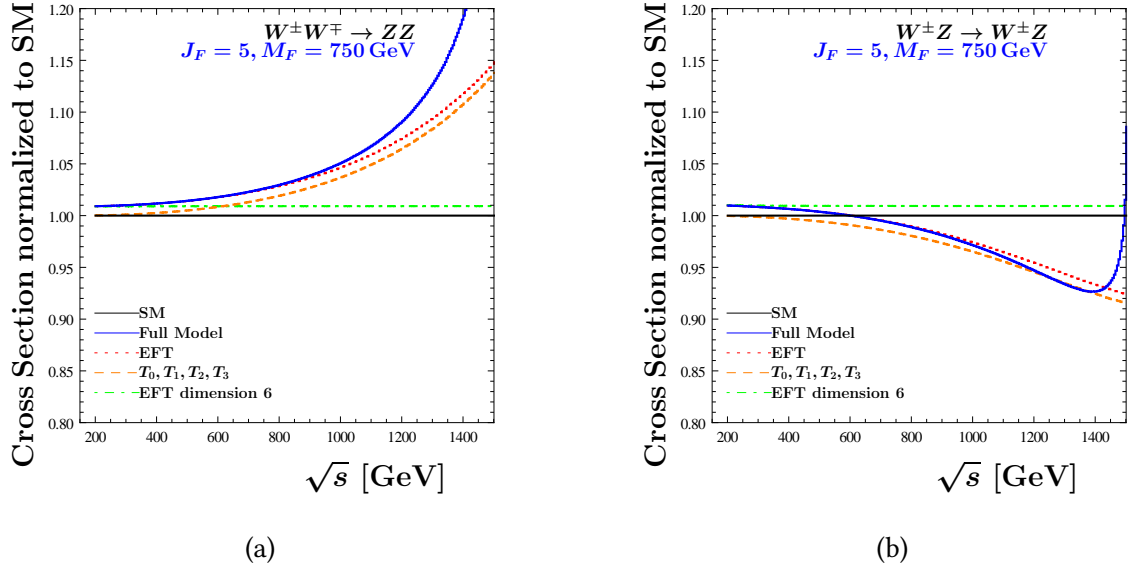


Figure 5.6.: Cross section summed and averaged over helicities normalized to the SM cross section depicted as a function of the COM energy \sqrt{s} up to $2M = 1500$ GeV for (a) $WW \rightarrow ZZ$ scattering and (b) $WZ \rightarrow WZ$ scattering in the case of one new fermion multiplet ($J_F = 5, M_F = 750$ GeV).

dominated by the pure SM contribution to the cross section, as was seen in the examples of Figs. 5.2 and 5.3. Thus, we see in Fig. 5.5 (b) that the relative difference of the cross section contribution of the anomalous squared piece only from the isospin symmetric part is large in the low-energy regime. But, for energies above $\sqrt{s} = 1100$ GeV the pure anomalous contribution to the cross section can be approximated within 10 % deviation with the isospin symmetric part alone. We can conclude, that the isospin symmetric part of the four-vertex correction dominates the other vertex corrections in the energy region where the anomalous part is of relevance. The same reasoning could be applied to the T-operators in comparison with the full EFT contribution, as they inherit the low-energy behavior of the isospin symmetric part of the four-boson vertex correction.

After we exemplified global features of the cross section over the whole energy range, it is worthwhile to focus on the behavior for energies below the peak and analyze the validity of the EFT. In figure 5.6 we present the cross section up to $\sqrt{s} = 1500$ GeV normalized to the SM values for the $WW \rightarrow ZZ$ and $WZ \rightarrow WZ$ scattering for one fermion multiplet and compare the full model and different classes of the EFT approximation. The full EFT approximation (dotted, red) is in good accordance with the full model calculation (solid, blue) up to energies of 1000 GeV with a deviation of less than 1 %. Where the difference between the EFT and the full model amounts to 1 %, both deviate approximately by 5 % from the SM. If we look at the dimension 6 EFT approximation (dot-dashed, green), we see a continuous relative offset to the SM of about 1 % which dominates the low energy behavior of the full EFT (dotted, red) until 600 GeV. This offset is not present in the T-operator only approximation (dashed, orange) which coincides with the SM prediction for 200 GeV. The low energy offset, can be explained when considering the expected energy dependence

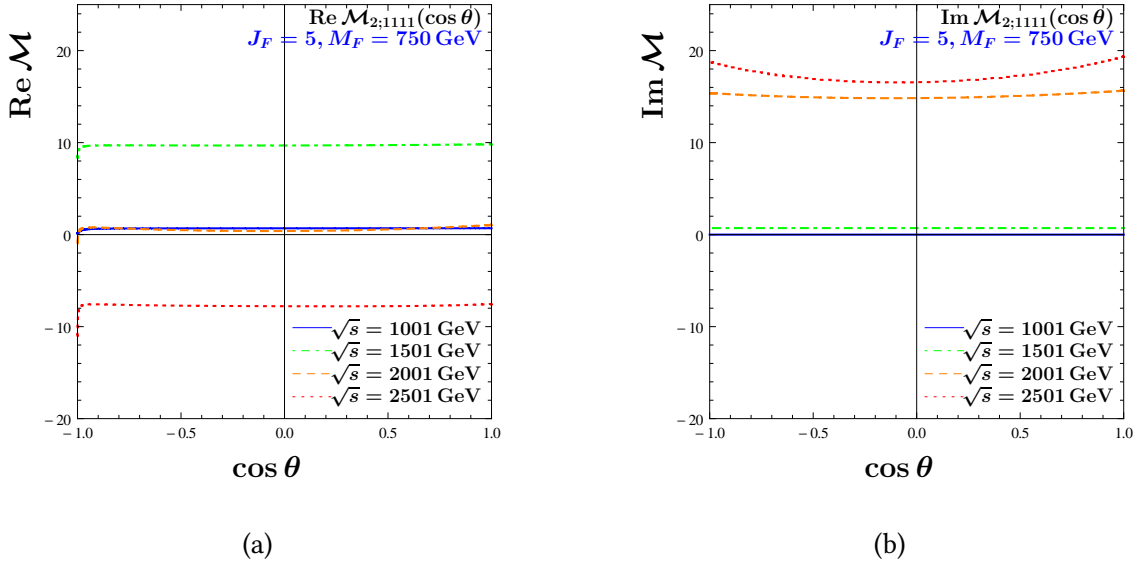


Figure 5.7.: Helicity amplitude $\mathcal{M}_{2;1111}$ for energies $\sqrt{s} = 1001, 1501, 2001, 2501$ GeV as a function of the COM scattering angle values for $\cos\theta \in [-1, 1]$. We depict (a) the real part and (b) the imaginary part separately.

of the observed EFT operators. For each insertion of an EFT dimension 6 vertex, we expect an energy dependence of $\sim \frac{s}{\Lambda^2} \sim \frac{s}{M^2}$, whereas in the case of the T-operators, which have energy dimension 8, we expect a $\sim \frac{s^2}{\Lambda^4} \sim \frac{s^2}{M^4}$ behavior. For low energies at the kinematic threshold, this still amounts for a non-vanishing anomalous contribution with a suppression of $\sim \frac{m_W^2}{M^2}$ for the dimension 6 operators and $\sim \frac{m_W^4}{M^4}$ for the T-operators, respectively. Hence, an explicit evaluation in the case of $WW \rightarrow ZZ$ scattering at the kinematic threshold of $\sqrt{s} = 2m_W$ results in a 0.9% deviation for the dimension 6 operators, whereas the T-operators amount for only 0.004%. Besides the missing offset, however, the shape of the T-operator approximation behaves qualitatively like the full EFT, as the T-operators are dominant at high energies.

5.5. Angular dependence of the amplitudes

In this section we discuss the angular behavior of the non-vanishing helicity amplitudes. Hereby, we consider only the anomalous part following from the NP contribution, as the SM contribution is well understood.

All amplitudes are formed out of the basic amplitudes following from Eq. (5.3). Also considering the redundancy $\mathcal{M}_3 = [\mathcal{M}_2]_{t \leftrightarrow u}$, it is sufficient to analyze the basic amplitudes \mathcal{M}_1 and \mathcal{M}_2 in order to discuss the angular dependence of the helicity amplitudes.

As it turns out, we only find non-negligible values for the helicity amplitudes $\mathcal{M}_{i;1111}$, $\mathcal{M}_{i;11-1-1}$, $\mathcal{M}_{i;1-11-1}$, $\mathcal{M}_{i;1-1-1-1}$, $\mathcal{M}_{i;-1-111}$, $\mathcal{M}_{i;-11-11}$ and $\mathcal{M}_{i;-111-1}$. Since $\mathcal{M}_{i;-1-1-1-1}$, $\mathcal{M}_{i;-1-111}$, $\mathcal{M}_{i;-11-11}$ and $\mathcal{M}_{i;-111-1}$ follow from helicity inversion of $\mathcal{M}_{i;1111}$, $\mathcal{M}_{i;11-1-1}$, $\mathcal{M}_{i;1-11-1}$ and $\mathcal{M}_{i;1-1-11}$, respectively, they are exactly the same and, therefore, the discussion of one

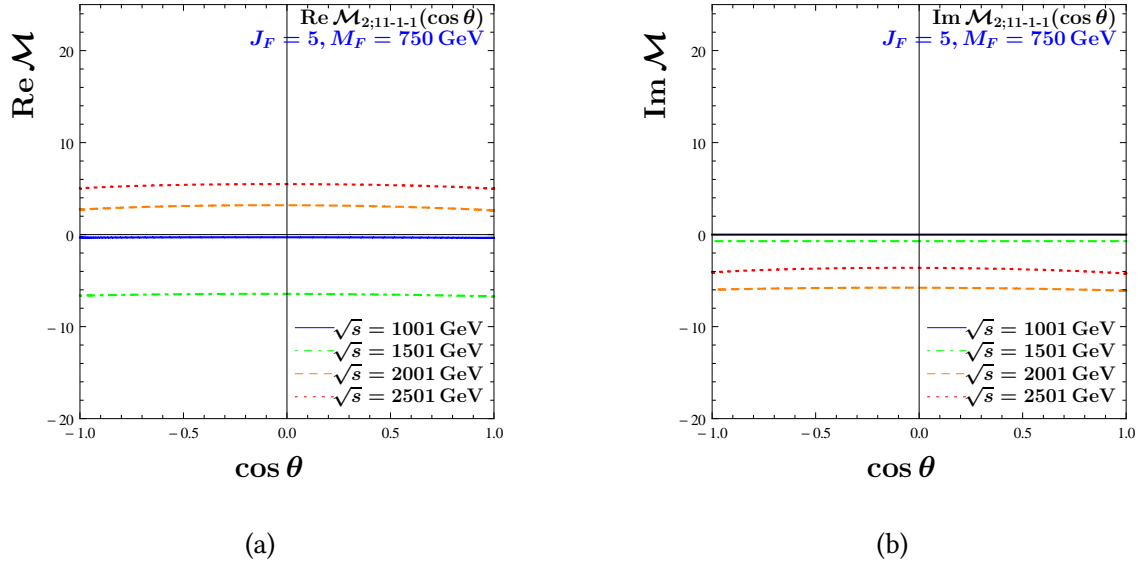


Figure 5.8.: Helicity amplitude $\mathcal{M}_{2;11-1-1}$ for energies $\sqrt{s} = 1001, 1501, 2001, 2501$ GeV as a function of the COM scattering angle values for $\cos\theta \in [-1, 1]$. We depict (a) the real part and (b) the imaginary part separately.

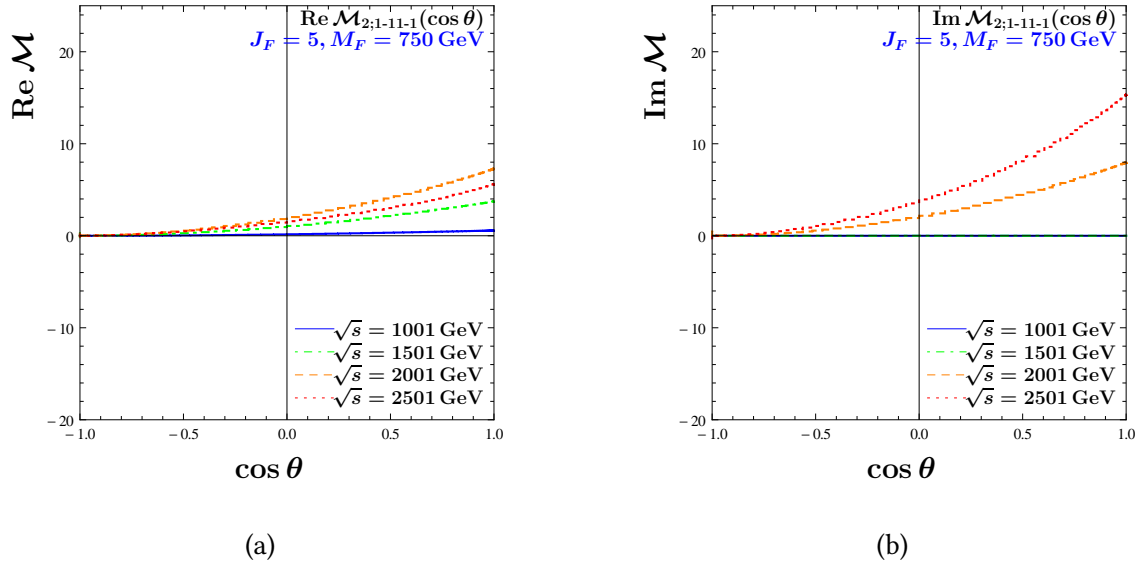


Figure 5.9.: Helicity amplitude $\mathcal{M}_{2;1-11-1}$ for energies $\sqrt{s} = 1001, 1501, 2001, 2501$ GeV as a function of the COM scattering angle values for $\cos\theta \in [-1, 1]$. We depict (a) the real part and (b) the imaginary part separately.

set is sufficient. The qualitative difference in the angular dependence between \mathcal{M}_1 and \mathcal{M}_2 is only marginal. $\mathcal{M}_{2;1111}$ and $\mathcal{M}_{2;11-1-1}$ are slightly asymmetric in the exchange $\theta \rightarrow \pi - \theta$ for extreme values of $\cos\theta$ very close to ± 1 , whereas the helicity amplitudes of \mathcal{M}_1 are completely symmetric. Also it yields $\mathcal{M}_{1;1-11-1} = [\mathcal{M}_{1;1-1-11}]_{\theta \rightarrow \pi - \theta}$, which is not perfectly satisfied for \mathcal{M}_2 for angles close to the beam axis $\cos\theta = \pm 1$. Nevertheless, the contribution

of this asymmetry gets irrelevant when predicting observables or calculating partial-wave (PW) coefficients, as will be discussed in the subsequent section.

In Fig. 5.7 we depict the real and imaginary part of $\mathcal{M}_{2;1111}$ for different energy values as a function of $\cos \theta$. The helicity amplitude remains almost constant throughout the whole range of angles. Only for higher energies, we see a parabola-like form which starts when $\sqrt{s} \sim 2500$ GeV (dotted, red) in the imaginary part. Also, there is almost no asymmetry for interchanging $\cos \theta \leftrightarrow -\cos \theta$. Due to the almost symmetric dependence a PW decomposition is expected to be dominated by even coefficients. We expect a dominating $j = 0$ PW and corrections for higher energies coming from the $j = 2$ PW. Another important feature of the helicity amplitude is given by the sign of real and imaginary part. The real part has positive values for lower energies, reaching its maximum for the peak at $\sqrt{s} = 1500$ GeV. For higher energies, the real part decreases, leading to negative values. Due to the flatness of the amplitude, we will further investigate this behavior by analyzing the $j = 0$ PW in the next section. The imaginary part will only be non-vanishing for energies above $\sqrt{s} = 1500$ GeV resulting in positive values.

The corresponding values for the helicity amplitude $\mathcal{M}_{2;11-1-1}$ are presented in Fig. 5.8. Most features are analogous to the $\mathcal{M}_{2;1111}$ helicity amplitude. The absolute values of the amplitude are rather small and the angular distribution exhibits an even milder dependence on $\cos \theta$. The main difference to the previous helicities is due to opposite signs in the amplitude. The real part changes the sign from negative to positive for rising energies and the imaginary part is negative above the peak at $\sqrt{s} = 1500$ GeV. This result is not true in the model for one scalar multiplet, where the signs are the same as the $\mathcal{M}_{2;1111}$ helicity amplitude and even the magnitude of the imaginary part is exactly the same.

Fig. 5.9 shows the helicity amplitude $\mathcal{M}_{2;1-11-1}$ over $\cos \theta$ separated in real and imaginary part. The amplitude vanishes for $\cos \theta \rightarrow -1$ and rises with increasing $\cos \theta$. The shape fits well to a parabola with minimum at $\cos \theta = -1$, what resembles the behavior of the $j = 2$ partial wave accompanied by the Wigner d function $d_{2,2}^2 = \frac{1}{4}(1 + \cos \theta)^2$. The amplitude gets more pronounced for higher energies.

We can close this section with the conclusion, that all the features of the non-negligible helicity amplitudes $\mathcal{M}_{i;1111}$, $\mathcal{M}_{i;11-1-1}$, $\mathcal{M}_{i;1-11-1}$ and $\mathcal{M}_{i;1-1-11}$ can be well covered by the $j = 0$ and $j = 2$ PW, respectively. A thorough discussion of the PW decomposition follows in the next section. We can use the previous observations to explain the positive and negative interference between the SM and the anomalous contribution seen in Figs. 5.2 and 5.3. The dominant anomalous contribution to the helicity averaged cross section follows from the helicity amplitude $\mathcal{M}_{i;1111}$. On the one hand, the corresponding tree-level helicity amplitude in the SM is positive for all values of \sqrt{s} and all scattering angles in the case of $WW \rightarrow ZZ$ scattering, whereas it is negative in the case of $WZ \rightarrow WZ$ scattering. On the other hand, the anomalous part of the helicity amplitude $\mathcal{M}_{i;1111}$ starts with positive real values that fall into negative values at some point after the peak energy $\sqrt{s} = 1500$ GeV. Thus, the interference term $2\text{Re}(\mathcal{M}_{SM}\mathcal{M}_{\text{anom}}^*)$ gives a positive or a negative contribution to the cross section depending on the combination of the helicity amplitudes at a specific energy. For $WZ \rightarrow WZ$ scattering we therefore have a destructive interference for energies below the sign change in the anomalous amplitude. This even leads to a damping of the cross section $|\mathcal{M}_{SM} + \mathcal{M}_{\text{anom}}|^2$ below the threshold for pair production, since the

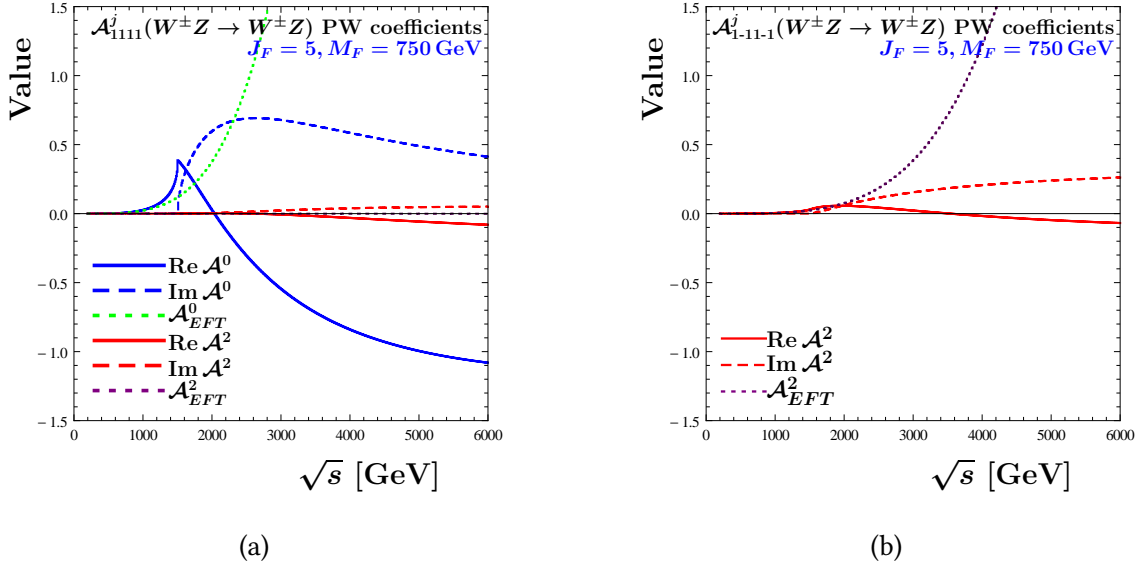


Figure 5.10.: PW coefficients (a) $\mathcal{A}_{1111}^j(WZ \rightarrow WZ)$ and (b) $\mathcal{A}_{1-11-1}^j(WZ \rightarrow WZ)$ as a function of \sqrt{s} for $j = 0, 2$. The full model and the EFT coefficient are shown.

interference term dominates the pure anomalous squared contributions in this energy range due to small anomalous amplitude values.

5.6. Partial wave analysis

In this section we want to analyze the partial-wave (PW) coefficients up to $j = 2$ in the sum of Eq. (3.33) and validate the accuracy of this approximation of the amplitude. Afterwards we explicitly check, whether our one-loop calculation with the chosen model parameters still satisfies the unitarity considerations discussed in Section 3.2. For this purpose we diagonalize the PW coefficients $\mathcal{A}_{\lambda_1\lambda_2\lambda_3\lambda_4}^j$, which are defined in Eq. (3.33), with respect to the helicity space and isospin channel and present the largest eigenvalue together with the already mentioned Argand circle.

We depict the dominant PW coefficients for the helicity amplitudes $\mathcal{M}_{1111}(WZ \rightarrow WZ)$ and $\mathcal{M}_{1-11-1}(WZ \rightarrow WZ)$ in Fig. 5.10. As it turns out, all the $j = 1$ PW coefficients remain of order $\mathcal{O}(10^{-2})$ and below even in the shown case of WZ -scattering, where there is no symmetry forcing it to vanish. Hence, we neglect depicting it, since it would not be distinguishable from zero in the employed scaling of the plot.

We clearly notice, that the largest values follow from the $j = 0$ PW of the helicity amplitude \mathcal{M}_{1111} . This $j = 0$ PW coefficient in Fig. 5.10 (a) already describes most of the features of the amplitude displayed in Fig. 5.7, since the $j = 0$ PW describes a shift in the amplitude which has no angular dependence. We recognize the rise in the real part (solid, blue) until reaching its peak maximum at $\sqrt{s} = 1500$ GeV followed by a decrease for energies above, resulting in a sign-flip slightly after 2000 GeV. The imaginary part (dashed, blue) contributes for $\sqrt{s} \geq 1500$ GeV and rises until $\sqrt{s} = 2500$ GeV. For higher energies its value declines, indicating that it will approach 0 again in the large-energy limit. We

see small values for the \mathcal{A}_{1111}^2 partial wave (red) for energies above 2000 GeV, that will explain the parabola shape seen in Fig. 5.7 for large energies. Another observation shows that the PW coefficient for the EFT (dotted, green) coincides with the real value of the full model in the low-energy regime, therefore giving a valid approximation. For energies above $\sqrt{s} \geq 1100$ GeV, however, the deviation starts increasing, as the EFT cannot capture the peak structure. After the peak the EFT approximated PW coefficient continues with an unphysical rise. Additionally, the EFT does not follow the full model for the $j = 2$ PW for the \mathcal{M}_{1111} amplitude. So, we can conclude that the EFT just extends the low-energy behavior of the model when leaving its region of validity, e.g. at high energies \sqrt{s} .

The real part of the PW coefficient shown in Fig. 5.10 (b) (solid, red) also rises for lower energies, but it reaches its maximum value around 1900 GeV after the imaginary part (dashed, red) enters. The imaginary part continuously increases for rising energies, however with decreasing gradient. The EFT PW coefficient (dotted, purple) again follows the behavior of the real part in the beginning, but exhibits a divergent behavior for high energies.

In the following part we demonstrate, how the eigenvalues of the PW coefficients are analytically constructed after we approximate negligible contributions with zero. Subsequently, we will present the Argand diagram showing the behavior of the dominant eigenvalues.

In order to find the highest coefficient eigenvalues, we first deduce which helicities will give a non-negligible contribution to the process. We define three basic partial wave coefficient matrices in helicity space A_1^j, A_2^j, A_3^j analogously to Eq. (5.3), as we then do not have to check for each channel separately. This is possible, because the partial wave coefficients were projected out on the level of amplitudes (not cross sections) which was shown in Eq. (3.37). Therefore, the definition reads

$$A_{i; \lambda_1 \lambda_2 \lambda_3 \lambda_4}^j := \frac{\beta}{16\pi} \int_{-1}^1 d \cos \theta \mathcal{M}_{i; \lambda_1 \lambda_2 \lambda_3 \lambda_4}(\theta) d_{\lambda_{12} \lambda_{34}}^j(\theta) \quad \text{for } i = 1, 2, 3. \quad (5.8)$$

Using those basic PW coefficients, we recover the PW coefficients of the physical channels from linear combination and proper normalization due to symmetry factors, thus leading to the identification table

$$\begin{aligned} \mathcal{A}^j (W^\pm W^\mp \rightarrow ZZ) &= \frac{1}{\sqrt{2}} A_1^j \\ \mathcal{A}^j (W^\pm Z \rightarrow W^\pm Z) &= A_2^j \\ \mathcal{A}^j (W^\pm Z \rightarrow ZW^\pm) &= A_3^j \\ \mathcal{A}^j (W^\pm W^\mp \rightarrow W^\pm W^\mp) &= A_1^j + A_2^j \\ \mathcal{A}^j (W^\pm W^\mp \rightarrow W^\mp W^\pm) &= A_1^j + A_3^j \\ \mathcal{A}^j (W^\pm W^\pm \rightarrow W^\pm W^\pm) &= \frac{1}{2} (A_2^j + A_3^j) \\ \mathcal{A}^j (ZZ \rightarrow ZZ) &= \frac{1}{2} (A_1^j + A_2^j + A_3^j). \end{aligned} \quad (5.9)$$

So, we are able to identify negligible helicities by considering the above basic amplitude contribution or, equivalently, the basic PW coefficients.

As discussed in the previous section, we see only relevant amplitude values for the helicity amplitudes $\mathcal{M}_{i;1111}$, $\mathcal{M}_{i;11-1-1}$, $\mathcal{M}_{i;1-11-1}$ and $\mathcal{M}_{i;1-1-1-1}$ and the amplitudes with inverted helicity, that will give the same PW coefficient. Thus, we only have to evaluate contributions for those coefficients. Our observation showed, that all the basic PW coefficients behave similarly, hence the conclusions made for WZ -scattering with Fig. 5.10 hold in a general VBS process.

Since all $j = 1$ PW coefficients are very close to 0 and the $j = 2$ contributions turn out to be less relevant than the $j = 0$ contribution, the dominant eigenvalue is to be found in the $j = 0$ PW coefficient matrix. Thus, we have to work with the helicity matrix

$$\begin{pmatrix} \mathcal{A}_{1111}^0 & \mathcal{A}_{11-1-1}^0 \\ \mathcal{A}_{-1-111}^0 & \mathcal{A}_{-1-1-1-1}^0 \end{pmatrix} = \begin{pmatrix} \mathcal{A}_{1111}^0 & \mathcal{A}_{11-1-1}^0 \\ \mathcal{A}_{11-1-1}^0 & \mathcal{A}_{1111}^0 \end{pmatrix}, \quad (5.10)$$

where each element is to be understood as a matrix in the different vector boson channels. This helicity matrix can be easily brought to a diagonal form with

$$\begin{aligned} & \begin{pmatrix} \frac{1}{\sqrt{2}} & \frac{1}{\sqrt{2}} \\ \frac{1}{\sqrt{2}} & -\frac{1}{\sqrt{2}} \end{pmatrix} \cdot \begin{pmatrix} \mathcal{A}_{1111}^0 & \mathcal{A}_{11-1-1}^0 \\ \mathcal{A}_{-1-111}^0 & \mathcal{A}_{-1-1-1-1}^0 \end{pmatrix} \cdot \begin{pmatrix} \frac{1}{\sqrt{2}} & \frac{1}{\sqrt{2}} \\ \frac{1}{\sqrt{2}} & -\frac{1}{\sqrt{2}} \end{pmatrix} \\ &= \begin{pmatrix} \mathcal{A}_{1111}^0 + \mathcal{A}_{11-1-1}^0 & 0 \\ 0 & \mathcal{A}_{1111}^0 - \mathcal{A}_{11-1-1}^0 \end{pmatrix} \\ &=: \begin{pmatrix} \mathcal{A}_+^0 & 0 \\ 0 & \mathcal{A}_-^0 \end{pmatrix}. \end{aligned} \quad (5.11)$$

Here we can interpret the \mathcal{A}_\pm^0 as the eigenvalues of the helicity space, given as matrix in the vector boson channels.

As we already finished the diagonalization with respect to the helicity combinations in our approximation, only the vector-boson channels are left to be diagonalized. To accomplish this, we include the redundancy of identical channels $W^\pm Z$ and ZW^\pm as well as $W^\pm W^\mp$ and $W^\mp W^\pm$, in order to get a symmetric result in terms of the basic PW coefficients A_1^0 , A_2^0 and A_3^0 . As we want to avoid double counting, we have to include a normalization of $\frac{1}{\sqrt{2}}$ for each redundancy in the initial and/or final state. The full matrix reads⁴

$$\mathcal{A}_\pm^0 = \begin{pmatrix} A_\pm^0 (W^\pm W^\pm \rightarrow W^\pm W^\pm) & 0 & 0 & 0 & 0 & 0 & 0 \\ 0 & \frac{1}{2} A_\pm^0 (W^\pm Z \rightarrow W^\pm Z) & \frac{1}{2} A_\pm^0 (W^\pm Z \rightarrow ZW^\pm) & 0 & 0 & 0 & 0 \\ 0 & \frac{1}{2} A_\pm^0 (ZW^\pm \rightarrow W^\pm Z) & \frac{1}{2} A_\pm^0 (ZW^\pm \rightarrow ZW^\pm) & 0 & 0 & 0 & 0 \\ 0 & 0 & 0 & \frac{1}{2} A_\pm^0 (W^+ W^- \rightarrow W^+ W^-) & \frac{1}{\sqrt{2}} A_\pm^0 (W^+ W^- \rightarrow ZZ) & \frac{1}{2} A_\pm^0 (W^+ W^- \rightarrow W^- W^+) & 0 \\ 0 & 0 & 0 & \frac{1}{\sqrt{2}} A_\pm^0 (ZZ \rightarrow W^+ W^-) & A_\pm^0 (ZZ \rightarrow ZZ) & \frac{1}{\sqrt{2}} A_\pm^0 (ZZ \rightarrow W^- W^+) & 0 \\ 0 & 0 & 0 & \frac{1}{2} A_\pm^0 (W^- W^+ \rightarrow W^+ W^-) & \frac{1}{\sqrt{2}} A_\pm^0 (W^- W^+ \rightarrow ZZ) & \frac{1}{2} A_\pm^0 (W^- W^+ \rightarrow W^- W^+) & 0 \end{pmatrix}. \quad (5.12)$$

The channels are already aligned in a block diagonal form. This can be explained due to conservation of isospin. The vector bosons W^\pm and Z form an isospin triplet representation

⁴The index \pm refers to the elements of the diagonal matrix for the helicity combinations, see Eq. (5.11). Hence, $A_\pm^0(\dots)$ are scalar quantities.

and they can be seen as one particle eigenstates of isospin $J_i = 1$ and isospin z-component $J_{i,z} = \{0, \pm 1\}$ [33], e.g.

$$|W^\pm\rangle = |J_i = 1, J_{i,z} = \pm 1\rangle, \quad (5.13a)$$

$$|Z\rangle = |J_i = 1, J_{i,z} = 0\rangle. \quad (5.13b)$$

The incoming and outgoing two-particle states form the product space in $SU(2)_L$ of two triplets. The resulting irreducible representations of $SU(2)_L$ are given by $3 \otimes 3 = 5 \oplus 3 \oplus 1$. Hence, the elements of the product space can be decomposed into a quintet, a triplet and a singlet in the space of total isospin that form the orthonormal states. Using the rules for angular momentum addition known from quantum mechanics the product of two triplet states $|J_1 = 1, J_{1,z}\rangle, |J_2 = 1, J_{2,z}\rangle$ decompose as

$$|J_1 = 1, J_{1,z}\rangle \otimes |J_2 = 1, J_{2,z}\rangle = \sum_{J=|J_{1,z}+J_{2,z}|}^2 c_J |J, J_z = J_{1,z} + J_{2,z}\rangle. \quad (5.14)$$

The states of total isospin $|J, J_z\rangle$ form an orthonormal set that remains unchanged in our VBS process, as we did not include additional $SU(2)_L$ symmetry breaking. Thus, they represent the basis in which the matrix of Eq. (5.12) has diagonal form. The blocks in the matrix of Eq. (5.12) are given by the z-component of the total isospin, namely J_z , since it directly follows from the addition of the z-component of the one-particle isospin states, e.g.

$$|W^\pm W^\mp\rangle \sim |J_1 = 1, J_{1,z} = \pm 1\rangle \otimes |J_2 = 1, J_{2,z} = \mp 1\rangle = \sum_{J=0}^2 c_J |J, J_z = 0\rangle. \quad (5.15)$$

Hence, we can treat each block of isospin z-component J_z separately.

Starting with the isospin z-component $J_z = \pm 2$, there is nothing to be diagonalized, since $|W^\pm W^\pm\rangle$ forms the only possible $J_z = \pm 2$ two particle state. So the first eigenvalues are

$$a_\pm^0(J = 2, J_z = \pm 2) = \frac{1}{2} \left(A_{2;\pm}^0 + A_{3;\pm}^0 \right), \quad (5.16)$$

where $J = 2$ means, that the two particle state is an element of the $SU(2)_L$ quintett. We continue with $J_z = 1$, where we consider the matrix

$$\begin{pmatrix} \frac{1}{2}A_\pm^0(W^\pm Z \rightarrow W^\pm Z) & \frac{1}{2}A_\pm^0(W^\pm Z \rightarrow ZW^\pm) \\ \frac{1}{2}A_\pm^0(ZW^\pm \rightarrow W^\pm Z) & \frac{1}{2}A_\pm^0(ZW^\pm \rightarrow ZW^\pm) \end{pmatrix} \\ = \frac{1}{2} \begin{pmatrix} A_\pm^0(W^\pm Z \rightarrow W^\pm Z) & A_\pm^0(W^\pm Z \rightarrow ZW^\pm) \\ A_\pm^0(W^\pm Z \rightarrow ZW^\pm) & A_\pm^0(W^\pm Z \rightarrow W^\pm Z) \end{pmatrix}. \quad (5.17)$$

Due to the symmetric nature of the submatrix, the eigenvalues can be directly read off, resulting in

$$\begin{aligned} a_\pm^0(J = 2, J_z = \pm 1) &= \frac{1}{2} \left(A_{2;\pm}^0 + A_{3;\pm}^0 \right), \\ a_\pm^0(J = 1, J_z = \pm 1) &= \frac{1}{2} \left(A_{2;\pm}^0 - A_{3;\pm}^0 \right), \end{aligned} \quad (5.18)$$

All the $J_z = 0$ processes align in the submatrix

$$\begin{pmatrix} \frac{1}{2}A_{\pm}^0(W^+W^- \rightarrow W^+W^-) & \frac{1}{\sqrt{2}}A_{\pm}^0(W^+W^- \rightarrow ZZ) & \frac{1}{2}A_{\pm}^0(W^+W^- \rightarrow W^-W^+) \\ \frac{1}{\sqrt{2}}A_{\pm}^0(ZZ \rightarrow W^+W^-) & A_{\pm}^0(ZZ \rightarrow ZZ) & \frac{1}{\sqrt{2}}A_{\pm}^0(ZZ \rightarrow W^-W^+) \\ \frac{1}{2}A_{\pm}^0(W^-W^+ \rightarrow W^+W^-) & \frac{1}{\sqrt{2}}A_{\pm}^0(W^-W^+ \rightarrow ZZ) & \frac{1}{2}A_{\pm}^0(W^-W^+ \rightarrow W^-W^+) \end{pmatrix}, \quad (5.19)$$

whose eigenvalues in terms of the basic PW coefficients are given by

$$\begin{aligned} a_{\pm}^0(J = 2, J_z = 0) &= \frac{1}{2} \left(A_{2;\pm}^0 + A_{3;\pm}^0 \right), \\ a_{\pm}^0(J = 1, J_z = 0) &= \frac{1}{2} \left(A_{2;\pm}^0 - A_{3;\pm}^0 \right), \\ a_{\pm}^0(J = 0, J_z = 0) &= \frac{1}{2} \left(3A_{1;\pm}^0 + A_{2;\pm}^0 + A_{3;\pm}^0 \right). \end{aligned} \quad (5.20)$$

We observe, that there is only a distinction between two particle states of different total isospin $J = \{2, 1, 0\}$ in the $SU(2)_L$ limit, which form the quintet, triplet and singlet representation, respectively. Therefore, including the eigenvalues due to helicity combinations we have six PW coefficient eigenvalues to check for unitarity.⁵

In Figs. 5.11 and 5.13 we show the PW coefficient eigenvalues of the isospin singlet and the isospin quintet, respectively. The isospin triplet does not have a relevant contribution, since the combination $\frac{1}{2} \left(A_2^j - A_3^j \right)$ is nonzero only for odd j for the analyzed helicities. We see, that the singlet combination exhibits the dominant eigenvalues. On the one hand, the $a_+^0(J = 0)$ (red) still behaves reasonably and stays within the required bounds of perturbative unitarity of Eq. (3.40) up to an energy of 3000 GeV when the real part acquires a too large absolute value. The $a_-^0(J = 0)$ eigenvalue (blue), on the other hand, already exceeds the bound on the real part at the peak energy and at an energy of 2000 GeV all three bounds are slightly violated. For higher energy values the imaginary part falls below its bound, but the real part alone continues exceeding the other bounds. So, we state that our model prediction slightly deviates from being within the unitarity bounds in a one-loop calculation. This is due to the chosen representation $J_F = 5$ of the fermion multiplet which couples quite strongly to the vector bosons. Hence, we have to be careful using perturbation theory on our model, as there might be large corrections from higher

⁵For a precise estimation at which COM energy the unitarity bound would be violated, we would also need to include the SM contribution. In general, we get also contributions for other helicity combinations than the discussed ones including longitudinal polarization, therefore needing a much more complicated diagonalization procedure than the one shown in Eq. (5.11). Fortunately, the SM contributions also approximately aligns in a maximal 2×2 block-diagonal manner, when depicted in matrices. The full $j = 0$ PW coefficients thus take the form

$$\begin{pmatrix} \mathcal{A}_{1111}^0 & \mathcal{A}_{11-1-1}^0 & 0 \\ \mathcal{A}_{11-1-1}^0 & \mathcal{A}_{1111}^0 & 0 \\ 0 & 0 & \mathcal{A}_{0000}^0 \end{pmatrix} \quad (5.21)$$

in helicity space. It is therefore ensured, that our construction of the dominant contribution remains valid, such that the analogous SM eigenvalue only has to be added. Since we include only the tree-level SM contribution, the SM eigenvalue will result in an energy dependent shift of the real part of the eigenvalue.

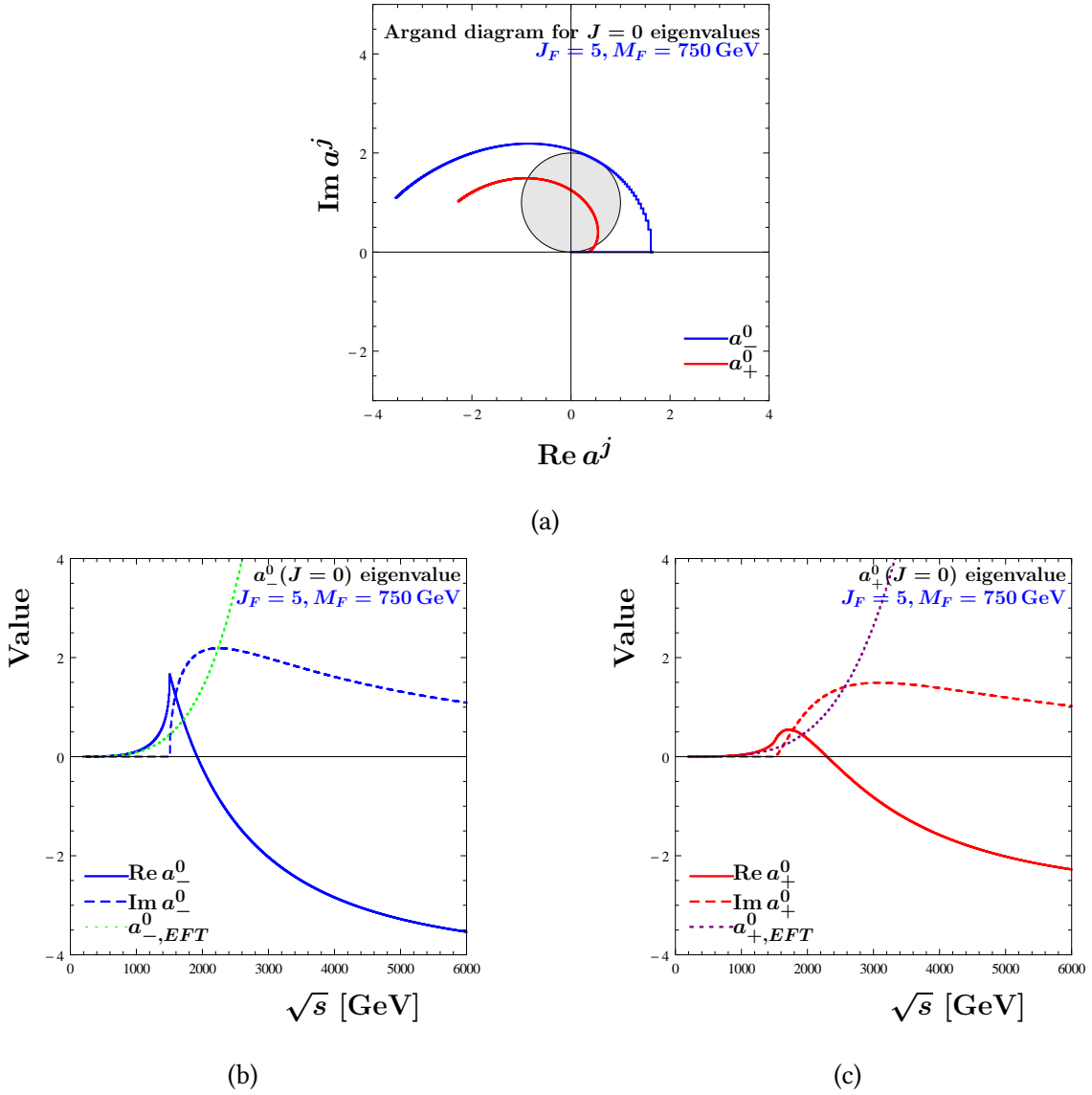


Figure 5.11.: Analysis of the isospin singlet PW coefficient eigenvalues $a_{\pm}^0 (J=0)$. We show (a) the Argand diagram for both eigenvalues and the diagram showing the real part, imaginary part and the EFT eigenvalue (b) of $a_-^0 (J=0)$ and (c) of $a_+^0 (J=0)$ as a function of \sqrt{s} .

order calculations. Nevertheless, we continue using our model with the given parameters perturbatively in the comparison with the EFT results, as only such high values of J_F give Wilson coefficients of the T-operators that are in the ballpark of the existing bounds.⁶

The EFT eigenvalues (dotted) of the singlet in Fig. 5.11 (a) approximate nicely the real part of the one-loop eigenvalues in the low energy regime, but start differing in the vicinity of the peak. For energies above the peak, both EFT eigenvalues start diverging

⁶The situation is much worse in the scalar case, as the dominant eigenvalue clearly exceeds the unitarity bound presented in Eq. (3.40). The behavior of the dominant eigenvalue is demonstrated in Appendix A.6.

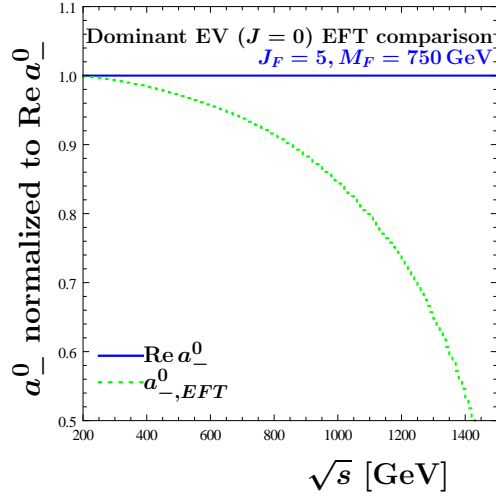


Figure 5.12.: Ratio plot $\frac{a_{-,EFT}^0(J=0)}{\text{Re } a_{-}^0(J=0)}$ for energies below the peak of the one-loop calculation.

to positive values, whereas the one-loop real value decreases. The unitarity bounds are violated starting from energies above 2000 GeV for a_{-}^0 ($J = 0$) and 2500 GeV for a_{+}^0 ($J = 0$). Fig. 5.12 shows a close-up in the low energy regime for the dominant eigenvalue of the PW amplitude of the pure EFT calculation (dotted, green) normalized to the eigenvalue in the one-loop calculation. The accuracy of the EFT is perfect at low energies, but quickly shows a $> 5\%$ deviation from the full model calculation already at an COM energy $\sqrt{s} = 750$ GeV, which corresponds to the loop-particle mass. A 10% deviation is already reached for 800 GeV.

For the isospin quintet of Fig. 5.13 both helicity eigenvalues stay within the required bounds of perturbative unitarity of Eq. (3.40) for a great range of the observed energy. Only for high energies above 3500 GeV, the absolute value of the real part of a_{-}^0 ($J = 2$) gets larger than the bound of 1. Still, such behavior is well compatible with unitarity. For the EFT eigenvalues, we have again a low energy agreement with the one-loop real value which does not hold for energies above the peak, however. In this region we observe a divergence to positive values even though these are sub-dominant eigenvalues.

We conclude, that our concrete fermion model should be taken with care, as it is not perfectly compatible with unitarity. Still, it is in the vicinity of the bounds given in Eq. (3.40) and, hence, it is still acceptable for our purpose of comparing with EFT predictions. We again see a good accordance of the EFT with the one-loop calculation in the low-energy regime, but there is a large deviation for higher energies leading to obvious unitarity violation.

5.7. Validity of the $j \leq 2$ partial wave approximation

In this section, we want to estimate the accuracy of the approximation of VBS in our model using a finite partial-wave (PW) expansion up to $j = 2$. We perform this exercise as we want to implement a finite PW expansion in the code VBFNL0 [9] which is used to

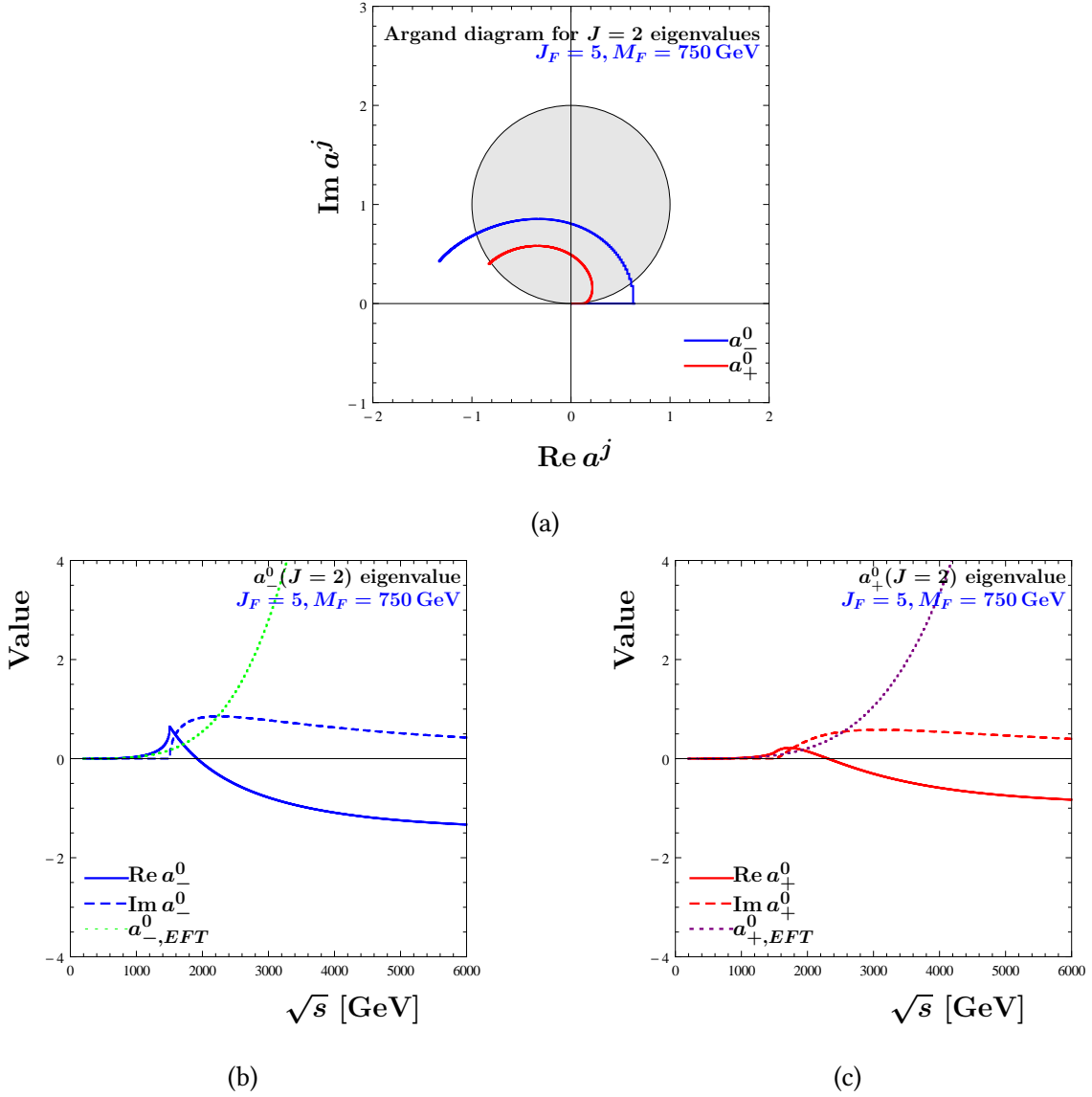


Figure 5.13.: Analysis of the isospin quintet PW coefficient eigenvalues a_{\pm}^0 ($J=2$). We show (a) the Argand diagram for both eigenvalues and the diagram showing the real part, imaginary part and the EFT eigenvalue (b) of a_-^0 ($J=2$) and (c) of a_+^0 ($J=2$) as a function of \sqrt{s} .

obtain results of our concrete model realization and its EFT setup for actual experimentally measured processes. We first discuss the reconstruction of the anomalous amplitude and comparison to the full calculated amplitude. Afterwards, we investigate the error on the total cross section summed over helicities when including the anomalous part with the up to $j=2$ PW expansion only in the dominant helicity amplitudes \mathcal{M}_{1111} , \mathcal{M}_{11-1-1} , \mathcal{M}_{1-11-1} , \mathcal{M}_{1-1-11} and in the amplitudes with inverted helicity.

In Fig. 5.14 we show the comparison of the anomalous helicity amplitude $\mathcal{M}_{2; \lambda_1 \lambda_2 \lambda_3 \lambda_4}$ and anomalous helicity amplitude $\mathcal{M}_{2; \lambda_1 \lambda_2 \lambda_3 \lambda_4}^{PW}$ based on the full calculation based on PWs

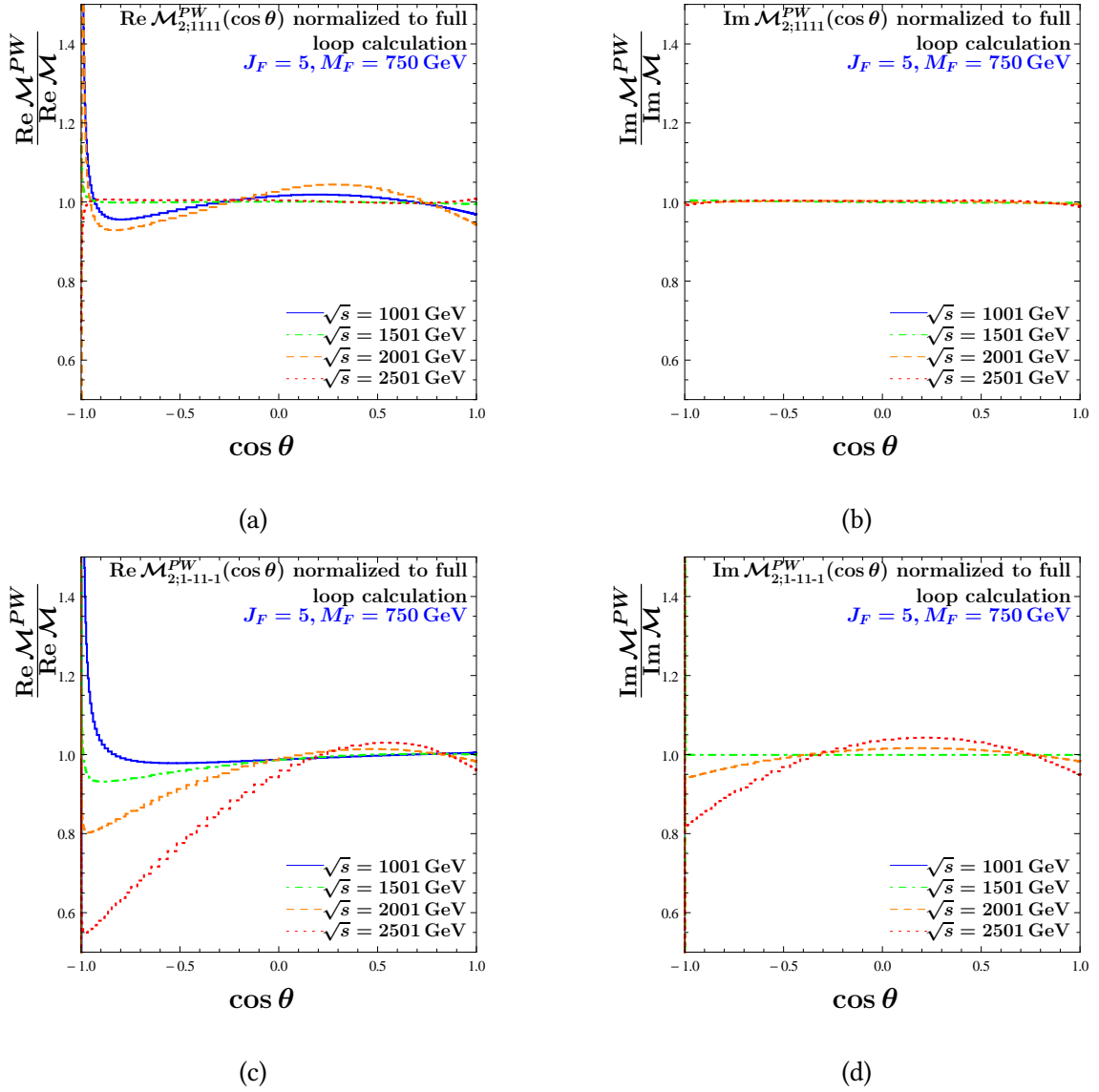


Figure 5.14.: Reconstructed real and imaginary part of the helicity amplitude $\mathcal{M}_{2;1111}^{PW}$ and $\mathcal{M}_{2;1-11-1}^{PW}$ normalized to the corresponding exact amplitude $\mathcal{M}_{2;1111}$ and $\mathcal{M}_{2;1-11-1}$ for energies $\sqrt{s} = 1001, 1501, 2001, 2501$ GeV plotted over the COM scattering angle values for $\cos \theta \in [-1, 1]$. We depict separately in (a) the case $\text{Re } \mathcal{M}_{2;1111}^{PW}$, in (b) the case $\text{Im } \mathcal{M}_{2;1111}^{PW}$, in (c) the case $\text{Re } \mathcal{M}_{2;1-11-1}^{PW}$ and in (d) the case $\text{Im } \mathcal{M}_{2;1-11-1}^{PW}$.

up to $j \leq 2$ for the example of helicities $(\lambda_1 \lambda_2 \lambda_3 \lambda_4) = \{(1111), (1-11-1)\}$. For the helicity amplitude $\mathcal{M}_{2;1111}$ we see perfect agreement of the imaginary part. Also the reconstructed real part is in good accordance with the exact result, since we only have a relative deviation of around 5% for the energies 1001 GeV (solid, blue) and 2001 GeV (dashed, orange). The region of $\cos \theta$ close to -1 with large relative deviation gives an irrelevant contribution when calculating cross sections. For the helicity amplitude $\mathcal{M}_{2;1-11-1}$ we see quite large relative deviations from the exact result presented in Fig. 5.9. But again, this relative

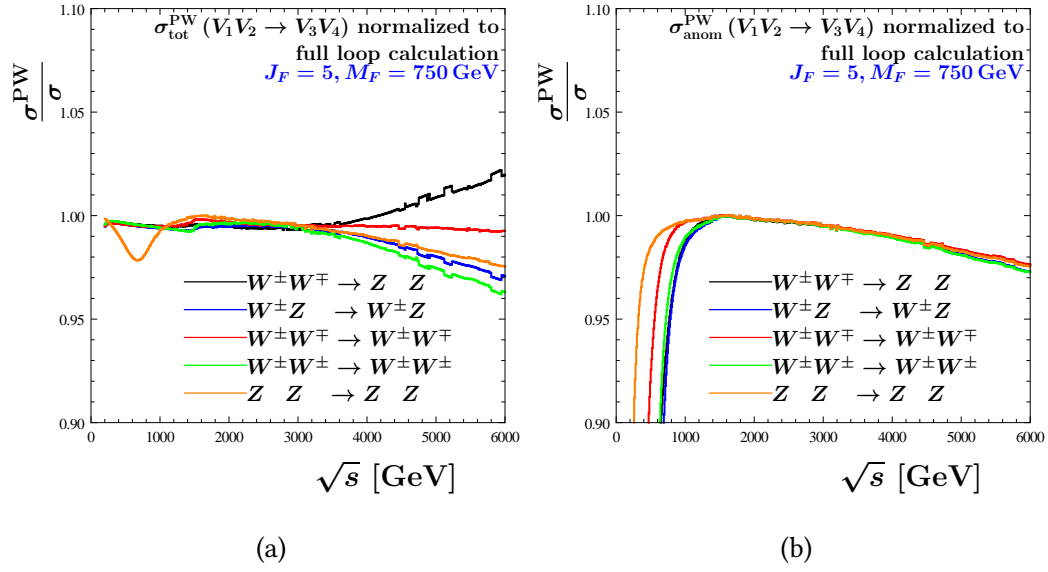


Figure 5.15.: Ratio plots for reconstructed polarization sum cross section normalized to the exact cross section $\frac{\sigma^{PW}}{\sigma}$ over COM energy \sqrt{s} for all VBS channels. We present (a) the total cross section and (b) only the anomalous squared part of the cross section.

deviation occurs in an angular region of negligible contribution compare to Fig. 5.9. Hence, we only have a $\leq 5\%$ relative deviation in the relevant region.

Our PW approximation only enters in the anomalous part of the amplitude, whereas we stick to the exact SM amplitude (as it is also part of VBFNLO). Additionally, with the arguments of the previous section, we only include the anomalous part for the dominant helicity amplitudes \mathcal{M}_{1111} , \mathcal{M}_{11-1-1} , \mathcal{M}_{1-11-1} , \mathcal{M}_{1-1-11} and for the inverted helicities, meaning

$$\mathcal{M}_{tot; \lambda_1 \lambda_2 \lambda_3 \lambda_4}^{PW} = \begin{cases} \mathcal{M}_{SM; \lambda_1 \lambda_2 \lambda_3 \lambda_4} + \mathcal{M}_{\lambda_1 \lambda_2 \lambda_3 \lambda_4}^{PW} & \text{if } \mathcal{M}_{\lambda_1 \lambda_2 \lambda_3 \lambda_4} \text{ dominant} \\ \mathcal{M}_{SM; \lambda_1 \lambda_2 \lambda_3 \lambda_4} & \text{else} \end{cases} \quad (5.22)$$

The PW approximated cross section σ^{PW} is then constructed by performing the polarization sum on $|\mathcal{M}_{tot; \lambda_1 \lambda_2 \lambda_3 \lambda_4}^{PW}|^2$. The result of this approximation for all VBS processes is shown in Fig. 5.15 as a ratio over the exact cross section summed over polarizations σ as a function of the energy \sqrt{s} . We notice, that the agreement of the PW reconstruction with the exact cross section only exhibits minor relative differences of $< 5\%$ in the observed energy range. This accuracy also holds for the pure anomalous part of the reconstructed cross section, since it stays within 3% deviation at high energies, where the squared anomalous contribution is dominant.

We therefore conclude, that the approximation with the small set of $j \leq 2$ PW coefficients for four independent helicity amplitudes \mathcal{M}_{1111} , \mathcal{M}_{11-1-1} , \mathcal{M}_{1-11-1} and \mathcal{M}_{1-1-11} gives a valid description of the physics of our underlying model. Thus, once those PW coefficients are known for a given energy, we are able to calculate an accurate estimation for the various aspects of the on-shell VBS process without evaluating any complicated loop integral and/or vertex structure. We can even further increase the efficiency of our phenomenological analysis, when we use the fact, that the PW coefficients can be calculated

without specifying the multiplet representation, as was indicated at the end of Section 4.1. This feature is implemented in our `VeBoS` program and the application is explained in Appendix A.5. Hence, we calculated the projection of our PW coefficients with only specifying the loop particle mass, such that we are able to adjust the representation according to the physics case we want to analyze.

6. Vector-boson scattering at the LHC

We finally discuss the impact of our previous findings in on-shell VBS for actual experimental analysis as they are performed by the multipurpose experiments ATLAS and CMS at the Large Hadron Collider (LHC). For this purpose we make use of the program VBFNLO [8–10] that takes into account various aspects needed for the simulation of hadronic collisions. Our modification will only take place in the electroweak calculation for the matrix elements of VBS. A minimal introduction to VBFNLO and our implementation of the new-physics (NP) model will be described in the next section. After introducing the implementation and outlining performed cross checks, we will present results for VBS in the ZZ and $W^\pm Z$ final states decaying further to leptons and neutrinos.¹ We finally highlight the impact on experimental analysis that set bounds on anomalous quartic-gauge couplings (aQGCs) by investigating the results of Refs. [6, 7].

6.1. VBFNLO and the implementation of the new-physics model

VBFNLO is a Monte Carlo program that simulates events that are induced by hadronic collisions between protons and/or antiprotons. The hadronic cross section is obtained by a convolution of the partonic cross sections, that start with gluons and quarks in the initial state, with parton distribution functions. The cross section can generically be written in the form

$$\sigma = \int dx_1 dx_2 \sum_{\text{subprocesses}} f_{a_1}(x_1) f_{a_2}(x_2) \frac{1}{2\hat{s}} \int d\Phi_n(x_1 P_1 + x_2 P_2; p_1 \dots p_n) \Theta(\text{cuts}) \overline{\sum} |\mathcal{M}(a_1 a_2 \rightarrow b_1 \dots b_n)|^2. \quad (6.1)$$

Here $f_{a_i}(x_i)$ are the parton distribution functions, that describe the probability to find a parton a_i inside the hadron i carrying the fraction x_i of the hadron total momentum P_i . $\sqrt{\hat{s}}$ is the COM energy of the two parton system and $d\Phi_n(x_1 P_1 + x_2 P_2; p_1 \dots p_n)$ is the Lorentz invariant phase space of the final state of the subprocess. $\Theta(\text{cuts})$ symbolically represents the cuts that exclude phase space points which do not fulfill the requirements set by the user and $\mathcal{M}(a_1 a_2 \rightarrow b_1 \dots b_n)$ is the Feynman amplitude representing the hard process, which absolute squared gets summed and averaged over polarizations and colors of the external partons.

¹I want to express my thank to Stefan Liebler, for his help in the implementation of the necessary cuts and for providing the numerical results which are presented throughout this chapter.

In the case of VBS with a leptonic decay in the final state vector bosons this matrix element $\mathcal{M}_{p_1 p_2 \rightarrow 4l jj}$ is separated into the leptonic tensor $\mathcal{M}_{V_1 V_2 \rightarrow 4l \mu \nu}$ containing the $V_1 V_2 \rightarrow V_3 V_4$ process and quark currents $J_{p_i \rightarrow j V_i}^{\mu_i}$ for the vector boson emitting partons. The leptonic tensor involves the virtual vector-boson propagation from the emitting quark lines, the Lorentz tensor for the VBS process, the propagation of outgoing bosons and currents $J_{V_i \rightarrow \bar{l}' l}$ for the decay into the final leptons.

Assuming all the participating currents are conserved, i.e. the quarks and leptons are approximated being massless, the tensor structure of the propagators can be further decomposed into a helicity sum over well defined off-shell polarization vectors. We refer to Ref. [18] for a careful derivation. This leads to the decomposition of the leptonic tensor in the form[18]

$$\mathcal{M}_{V_1 V_2 \rightarrow 4l \mu \nu} = \prod_{i=1}^4 \frac{1}{q_i^2 - m_{V_i}^2 + im_{V_i} \Gamma_{V_i}} \sum_{\lambda_1, \lambda_2, \lambda_3, \lambda_4} \epsilon_{J, \mu}^*(q_1, \lambda_1) \epsilon_{J, \nu}^*(q_2, \lambda_2) \mathcal{M}_{\lambda_1 \lambda_2 \lambda_3 \lambda_4}^{VBS} \epsilon_J(q_3, \lambda_3) \cdot J_{V_3 \rightarrow \bar{l}_1 l_2} \epsilon_J(q_4, \lambda_4) \cdot J_{V_4 \rightarrow \bar{l}_3 l_4}. \quad (6.2)$$

Hereby, $\frac{1}{q_i^2 - m_{V_i}^2 + im_{V_i} \Gamma_{V_i}}$ are the propagator denominators for the vector boson V_i with a finite decay width Γ_{V_i} . $\epsilon_{J, \mu_i}^{(*)}(q_i, \lambda_i)$ are the polarization vectors contracted with the conserved currents, that follow from the propagator decomposition. Finally, $\mathcal{M}_{\lambda_1 \lambda_2 \lambda_3 \lambda_4}^{VBS}$ is the helicity amplitude for VBS in the off-shell case.

The anomalous part of the matrix elements $\mathcal{M}_{\lambda_1 \lambda_2 \lambda_3 \lambda_4}^{VBS}$ following from any NP contribution are generically calculated from the partial-wave (PW) decomposition of the off-shell helicity amplitudes up to the $j = 2$ partial wave. For the case of anomalous couplings given by dimension 8 EFT operators this reproduces the exact result, as pointed out in Ref. [18]. Within the framework of VBFNLO there are also implemented unitarization models, that manipulate the PW coefficients before re-constructing the matrix elements, in order to restore the unitarity requirements of Eq. (3.40). In our subsequent analysis we will make use of the so-called T_u -model, which is illustrated in Ref. [18] and shall not be described in more detail here.

For our approximate estimation we feed the on-shell calculated PW coefficients for the COM energy given by the invariant mass of the final state into the VBFNLO PW decomposition of the helicity amplitude and include only the dominant helicity contributions. We implemented the possibility to choose the isospin J_R of the multiplets of the underlying model for each run of VBFNLO, since we calculated the PW coefficients by separating in different representation factors, as was discussed in Section 4.1. Of course, we neglected several aspects and expect noticeable differences arising from:

- We insert on-shell values into an off-shell matrix element. Hence, we do not treat virtual incoming vector bosons correctly. On the other hand, outgoing vector bosons are close to be on-shell, due to the employed experimental cuts.
- Our calculation is performed in the $SU(2)_L$ limit, in which photons are absent and the W and Z boson have identical mass, which for this study we set to $m_W = \frac{gv}{2} = 81.18$ GeV for our chosen values of $g = 0.66$ and $v = 246$ GeV. Though we split all

contributions involving an external Z boson with the weak mixing angle on a Z boson and a photonic contribution, we expect differences at low invariant masses, \sqrt{s} , of the gauge boson pair, where virtualities q_i^2 cannot be neglected compared to s .

- We only modify VBS as a 4-point interaction and do not include all contributions to the full $pp \rightarrow 4ljj$ process. Referring to the discussion of Fig. 5.5 we assume, that the dominant behavior should still be well covered, as neglected contributions do not exhibit the representation enhancement of $T_R C_{2,R} \sim J_R^5$.
- We do not include all helicity contributions. However, this difference should be at the percent level using previous arguments as presented in Section 5.7.

Therefore, our calculation needs to be understood as an approximation. We want to justify this approximation with some cross checks presented in Section 6.3.

6.2. VBFNLO settings

In this section we summarize all input parameters, that are specified in the VBFNLO input files. All predictions are made for a proton-proton collider with a COM energy of 13 TeV. We continue with some general settings, before we discuss the implemented cuts for the specific case of the analyzed processes.

For our cross section calculations, we used parton distribution functions at leading order, namely MMHT2014 [34], that are linked through LHAPDF [35]. The SM parameters have been set to the following values:²

- Higgs-boson mass: $m_H = 125.09$ GeV,
- W boson mass: $m_W = 80.398$ GeV,
- Z boson mass: $m_Z = 91.1876$ GeV,
- Weak mixing angle: $\sin^2 \theta_W = 0.222646$.

Predictions of the number of events are obtained for an integrated luminosity of 35 fb^{-1} , chosen for compatibility with the experimental analysis which we investigate further in Section 6.5.

We use VBFNLO to investigate the VBS subprocesses of $W^\pm Z$ and ZZ production. For the first case we consider the full electroweak (EW) processes

$$pp \rightarrow W^\pm Z jj \rightarrow l'^{\pm} \nu_l l^{\pm} l^{\mp} jj,$$

with $l, l' \in \{e, \mu\}$. Since we want to compare our results qualitatively in Section 6.5 with the estimation of bounds on aQGCs in Ref. [6], we followed the implementation of cuts in

²The values only enter the VBFNLO internal routines. The PW coefficients calculated in the on-shell scattering are generated with the parameters specified in Chapter 5.

their analysis as close as possible. Therefore, our cutflow includes:

$$\begin{aligned}
 p_T^{l'}, p_T^l &> 20 \text{ GeV}, & |\eta^e| &< 2.5, & |\eta^\mu| &< 2.4, \\
 |m_{ll} - m_Z| &< 15 \text{ GeV}, & m_{3l} &> 100 \text{ GeV}, & p_T^{\text{miss}} &> 30 \text{ GeV}, \\
 |\eta^j| &< 4.7, & p_T^j &> 50 \text{ GeV}, & |\Delta R(j, l)| &> 0.4 \\
 m_{jj} &> 500 \text{ GeV}, & |\Delta\eta_{jj}| &> 2.5, & |\eta^{3l} - \frac{\eta^{j_1} + \eta^{j_2}}{2}| &< 2.5. \quad (6.3)
 \end{aligned}$$

We denote with “3l” the three-lepton system, i.e. the sum of the three lepton momenta, and its invariant mass m_{3l} and its rapidity η^{3l} . We simplify our calculation in comparison to the CMS analysis, as we only take into account the flavour combination $l' = e, l = \mu$ and multiply our results by a factor of 4 in order to approximate for all flavour combinations. As a consequence we have just one cut on the transverse momentum $p_T^l, p_T^{l'}$, which is chosen equal for all leptons. The cuts depicted in the last two lines of Eq. (6.3) are typical VBS cuts, which enhance the contribution of EW VBS over QCD-induced VBS and other SM background.

For the case of ZZ production, we calculate the cross section with VBFNLO of the full EW processes

$$pp \rightarrow ZZjj \rightarrow l'^{\pm} l'^{\mp} l^{\pm} l^{\mp} jj,$$

with $l, l' \in \{e, \mu\}$. The experimental analysis which uses those processes to bound anomalous operators is given in Ref. [7]. We again mainly follow their cutflow for a qualitatively comparison, namely

$$\begin{aligned}
 p_T^{l'}, p_T^l &> 20 \text{ GeV}, & |\eta^e| &< 2.5, & |\eta^\mu| &< 2.4, \\
 40 \text{ GeV} &< m_{ll}, m_{l'l'} < 120 \text{ GeV}, & |\eta^j| &< 4.7, & p_T^j &> 30 \text{ GeV}, \\
 |\Delta R(j, l)| &> 0.3, & m_{jj} &> 400 \text{ GeV}, & |\Delta\eta_{jj}| &> 2.4. \quad (6.4)
 \end{aligned}$$

As in the previous case, we restrict our calculation to the flavour combination $l' = e, l = \mu$ and multiply our result with a factor of 2. With our choice of the final state we avoid the problem of correctly assigning the leptons to the two Z boson candidates. Note that the actual experimental analysis is using a boosted decision tree, which also takes into account the Zeppenfeld variable to enhance the fraction of vector-boson scattering events over QCD background events.

6.3. Monte Carlo cross checks

This section is dedicated to the cross checks, we performed in order to validate the implementation and to roughly estimate the differences that appear due to the on-shell approximation and the $SU(2)_L$ limit of our model. We make use of the EFT T-operators that are part of our set and are also implemented in the set of aQGC EFT operators in the VBFNLO code, as presented in Ref. [9], with the addition of the O_{T_3} operator. For the cross check, we analyze a comparison of the predicted number of events, as given by

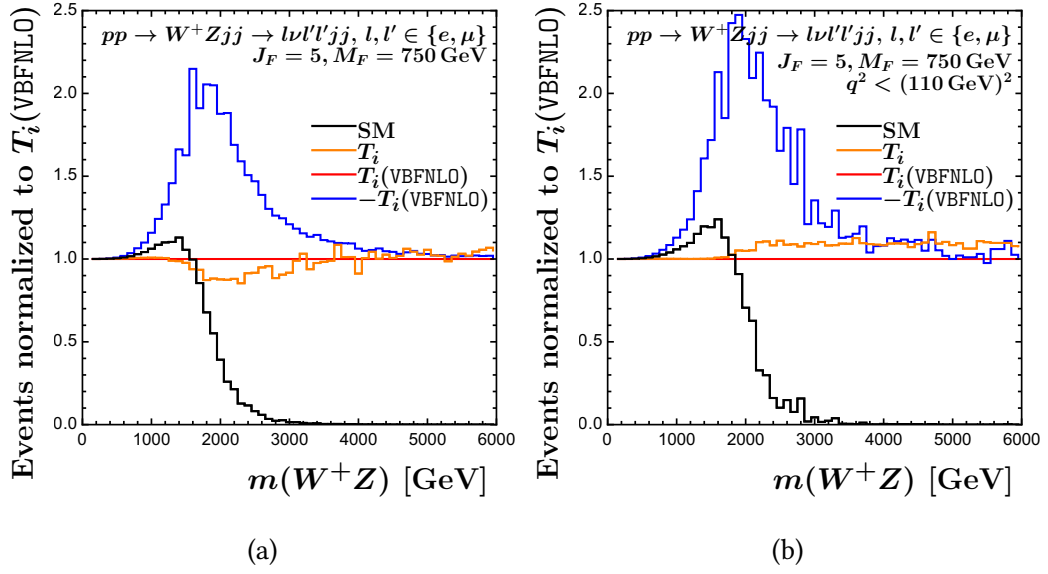


Figure 6.1.: Ratio plots for the predicted event number for the W^+Z production VBS process including aQGCs following from the set of T-operators calculated for PW coefficients extracted from the on-shell scattering events normalized to the respective events using the VBFNLO internally calculated PW coefficients as a function of the invariant mass of the two-boson final state $m(W^+Z)$. The underlying model determining the Wilson coefficients is given by a fermion multiplet with $(J_F = 5, M_F = 750 \text{ GeV})$. The contribution for internal T-operators are evaluated for the case of same and opposite sign of the Wilson coefficients in order to see the impact on the interference with the SM. We also depict the SM cross section for comparison. We show the cross check plots for the case (a) without restricting the virtuality of the incoming vector bosons and (b) with an artificial cut on the incoming momenta of $q^2 < (110 \text{ GeV})^2$.

feeding in the externally calculated PW coefficients using only the set of T-operators in the EFT calculation, with the VBFNLO internally calculated contribution. Since the internally calculated contribution respects the correct off-shell behavior and also uses the full $SU(2)_L \times U(1)_Y$ gauge group, we will use it as the reference prediction. In addition, we want to examine the interference behavior between the SM and anomalous contribution. Therefore, we also show the pure SM prediction and the result of the internal calculation with inverted sign of the Wilson coefficients for additional comparison. Furthermore, in order to identify the deviation that arises due to the missing virtuality of the incoming bosons in the on-shell approximation, we performed the same analysis with an unphysical cut on the incoming virtuality of $q^2 < (110 \text{ GeV})^2$. The drastically reduced statistics due to the cut was partly compensated using a previously calculated grid from a high statistics run, therefore selecting events in the relevant region of phase-space.

The results of the cross check are given in Fig. 6.1 for the case of W^+Z final state. We first note in Fig. 6.1 (a), that the pure SM contribution (black) exceeds slightly the normalization value for the VBFNLO internally predicted number of events (red) including aQGCs from the T-operators in the low-energy regime below $m(W^+Z) \sim 1600 \text{ GeV}$. This is expected,

since we also predicted destructive interference below the peak in the on-shell process as shown in Fig. 5.3, which was due to a different sign in the SM and the anomalous amplitude as discussed in Section 5.5. The predicted number of events including aQGCs following from the external PW coefficients (orange) shows a similar overall behavior as the internal calculated reference prediction. However, in the region of $1200 \text{ GeV} < m(W^+Z) < 3500 \text{ GeV}$ we have less predicted events for the on-shell calculated PW coefficients, reaching a deviation of $\sim 10\%$. In the high-energy regime, the predictions of the number of events based on the internal calculation and external PW coefficients coincide well. The calculation using inverted sign for the Wilson coefficients of the T-operators (blue) shows a constructive interference with the SM contribution, which contradicts the on-shell prediction and confirms that we inserted the external PW amplitude with the correct sign into VBFNLO. We see a doubling of the amount of predicted events for invariant masses around $m(W^+Z) \sim 1800 \text{ GeV}$ in comparison to the prediction using the correct sign. For the high-energy regime, both predictions match each other, since the anomalous contribution clearly dominates the pure SM prediction.

If we compare with the result after employing an artificial cut on the virtuality of the incoming vector bosons as shown in Fig. 6.1 (b), we see that the PW coefficients from on-shell approximation (orange) predict slightly more events than the VBFNLO internal calculation (red) for $m(W^+Z) > 1900 \text{ GeV}$ with a deviation of $\sim 10\%$. In the low-energy regime, both calculations coincide. Thus, we deduce, that the $\sim 10\%$ deviation seen in Fig. 6.1 (a) might be due to the virtuality of the incoming vector bosons, that is not taken into account in the on-shell approximation.

In the case of the ZZ final state of Fig. 6.2, we see a constructive interference between the SM and the aQGC contributions of the internal calculated reference prediction. The calculation with inverted sign in the Wilson coefficients (blue) exhibits a destructive interference, hence it does not resemble the expected interference behavior given by comparison with the on-shell $WW \rightarrow ZZ$ and $ZZ \rightarrow ZZ$ scattering of Figs. 5.2 and 5.4. The behavior of the on-shell and $SU(2)_L$ approximation (orange) in comparison with the reference prediction is qualitatively similar to the previous discussion of the W^+Z final state calculation. We again have an underestimation for invariant masses of $1000 \text{ GeV} < m(ZZ) < 3000 \text{ GeV}$ in the approximated prediction of Fig. 6.2 (a) with a higher deviation to the reference prediction of about $\sim 20\%$. This can be removed by the artificial cut on the incoming virtuality as seen in Fig. 6.2 (b), but we again have a 10% deviation in the other direction.

The conclusion of this section is as follows: The on-shell and $SU(2)_L$ approximation in the calculation of the PW coefficients is well justified in the case of T-operators for the W^+Z final state using the model parameters, as an accuracy of $\sim 10\%$ is sufficient for the analysis of the general model features that we discuss in the subsequent sections. The $\sim 20\%$ deviation appearing in the approximation for the ZZ final state calculation is more worrisome, nevertheless we should be able to perform a qualitative evaluation, since we are working with $SU(2)_L$ representations as high as $J_F = 5$ and $J_S = 8$ that should lead to strong effects in the cross section.

After this consideration, we may expect that calculations using the on-shell and $SU(2)_L$ approximation for the full set of EFT operators and the concrete model also lead to predictions within the desired accuracy. In the subsequent sections we display both the full

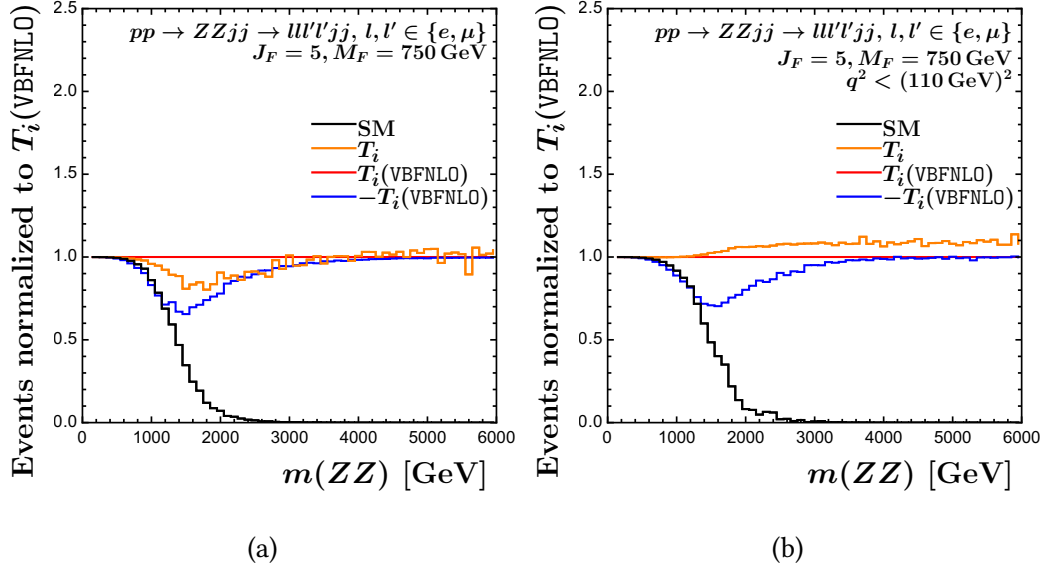


Figure 6.2.: Ratio plots for the predicted event number for the ZZ production VBS process including aQGCs following from the set of T-operators calculated for PW coefficients extracted from the on-shell scattering events normalized to the respective events using the VBFNLO internally calculated PW coefficients as a function of the invariant mass of the two-boson final state $m(ZZ)$. The underlying model determining the Wilson coefficients is given by a fermion multiplet with $(J_F = 5, M_F = 750 \text{ GeV})$. The contribution for internal T-operators are evaluated for the case of same and opposite sign of the Wilson coefficients in order to see the impact on the interference with the SM. We also depict the SM cross section for comparison. We show the cross check plots for the case (a) without restricting the virtuality of the incoming vector bosons and (b) with an artificial cut on the incoming momenta of $q^2 < (110 \text{ GeV})^2$.

model, the EFT and the T-operator contributions to the cross section based on the external amplitude. This ensures that their relative behavior is not affected from differences due to the on-shell/off-shell behavior or the $SU(2)_L$ limit.

6.4. Results for $W^\pm Z$ and ZZ production

After we have justified our implementation with necessary cross checks, we continue to discuss the analysis of the $W^\pm Z$ and ZZ production processes. We will describe and compare the predicted events generated by aQGCs induced by our model. We take into account the calculation using the full model, the complete EFT basis, the complete set of generated T-operators, the O_{T_2} operator alone and the T_u -model unitarized complete EFT basis. All calculations use the partial-wave (PW) coefficients calculated in the on-shell and $SU(2)_L$ approximation, except for the O_{T_2} operator, which uses the VBFNLO internal routines. We will also present the pure SM contribution as a reference.

The predictions for WZ production are shown in Fig. 6.3 for the model with an additional fermion multiplet with $J_F = 5$ and $M_F = 750 \text{ GeV}$. Note that the invariant mass of the

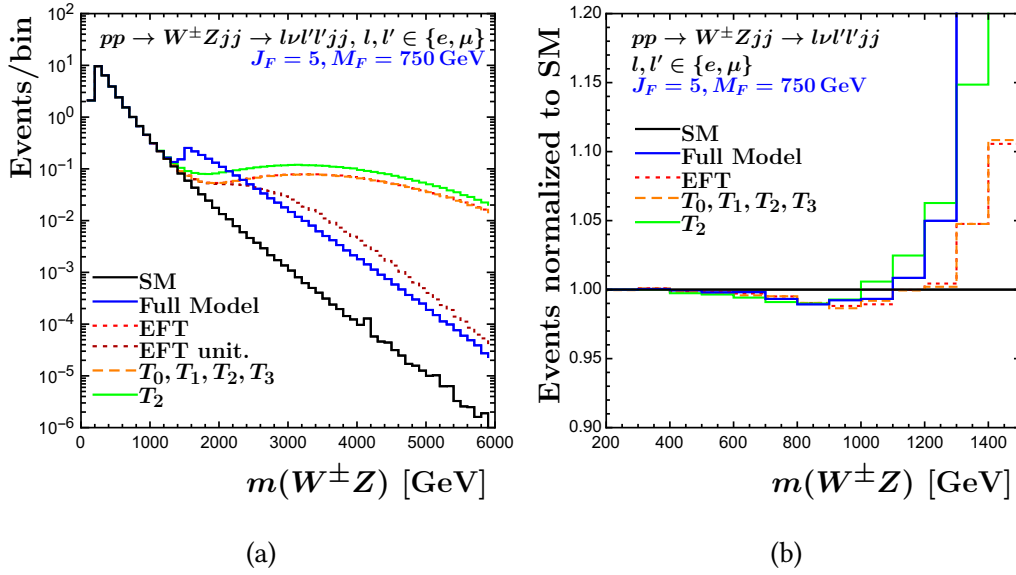


Figure 6.3.: Predicted event number per bin (100 GeV) for VBS with WZ final state in the full $pp \rightarrow l\nu l' l' jj$ process as a function of the invariant mass of the final state two boson system $m(W^\pm Z)$ where the aQGCs are induced by an additional fermion multiplet ($J_F = 5, M_F = 750$ GeV). We present (a) the distribution of predicted events over the whole energy range from $200 \text{ GeV} < m(W^\pm Z) < 6000 \text{ GeV}$ and (b) the predicted events normalized to the SM prediction for the low-energy regime $200 \text{ GeV} < m(W^\pm Z) < 1500 \text{ GeV}$.

gauge-boson system is not experimentally accessible for the W decaying into a lepton and a neutrino. To understand the phenomenology we however depict it on the x-axis in this section and turn to the transverse mass in the next section.

The SM prediction (solid, black) starts with 10 events per 100 GeV bin at $m(W^\pm Z) \sim 200$ GeV and then declines quickly due to the suppression of the partonic form factor convolution, diminishing by a bit more than an order of magnitude per 1000 GeV step on average. The aQGC contribution is negligible for the low energy regime up to $m(W^\pm Z) \sim 1000$ GeV. Slightly below the model peak at $m(W^\pm Z) \leq 1500$ GeV a noticeable deviation from the SM starts to develop as it is shown in Fig. 6.3 (a). The full model (solid, blue) forms its typical peak structure with a maximum at $m(W^\pm Z) = 1500$ GeV, the fermion pair production threshold, which has about a factor 3 difference to the SM. Afterwards, the predicted event number starts declining slower than the SM prediction, but having a trend seemingly parallel to the SM for high energies when the difference reaches about an order of magnitude. The complete EFT basis prediction (dotted, red) coincides with the full model (solid, blue) only in the low energy region for $m(W^\pm Z) < 1200$ GeV, where no relevant deviation from the SM prediction occurs. When the full model starts rising to the peak, the EFT already lost its validity, as it continues declining up to $m(W^\pm Z) \sim 1800$ GeV. Then the EFT rises slowly, hence dominating the form factor suppression, and declines slowly for invariant masses above $m(W^\pm Z) = 3000$ GeV. At about $m(W^\pm Z) \sim 2200$ GeV the full model prediction gets outperformed by the EFT estimation. This EFT high energy prediction clearly cannot be physical and violates unitarity at some point, as was previously

discussed in Section 5.6. If we compare the predictions of the T-Operator set (dashed, orange) and the complete EFT basis we see good accordance for all energies, as their overall shape is identical. The calculation using the O_{T_2} operator alone (solid, green) yields more predicted events than the calculation with the full EFT basis or the full set of T-operators. The deviation already starts at $m(W^\pm Z) \sim 1200$ GeV and dominates the complete model prediction above $m(W^\pm Z) \sim 2000$ GeV. Hence, this demonstrates a cancellation between individual T-operator contributions. The T_u -model unitarized EFT prediction (dotted, dark red) coincides with the naive EFT prediction up to $m(W^\pm Z) \sim 2000$ GeV, which is in the ballpark of the energy where the on-shell EFT prediction violates the unitarity bound, as discussed in Section 5.6. Above this invariant mass, the unitarization procedure sets in, effectively leading to a damping of the naive EFT prediction. In the regime of high invariant mass, the unitarized EFT exhibits a trend parallel to the complete model and to the SM prediction.

If we look closer in the low-energy region, as shown in Fig. 6.3 (b), we see the destructive interference predicted from on-shell scattering depicted in Fig. 5.3. The negative deviation from the SM (black) starts at an invariant mass around 500 GeV, but only leading to a maximal difference of 1 % for all contributions. For invariant masses above 1100 GeV the predictions including aQGCs all exceed the pure SM prediction. As was noticed beforehand, the predictions for the set of T-operators (dashed, orange) and the full EFT basis (dotted, red) lie on top of each other within statistics. For small invariant masses $m(W^\pm Z) \leq 1200$ GeV we see a negligible difference between the complete model and the EFT calculation. Therefore, the EFT serves as a reasonable approximation up to an invariant mass $m(W^\pm Z) \sim 1200$ GeV. However, the difference to the pure SM prediction of < 5 % is less than our estimated accuracy and also is only hardly accessible in experimental analysis.

In the following, we turn our attention to the prediction for $W^\pm Z$ production with the underlying model of an additional scalar multiplet as depicted in Fig. 6.4. Due to the higher suppression of EFT operators in the scalar case, this example chooses $J_S = 8$ and $M_S = 750$ GeV to generate operators in the ballpark of current bounds. Most features shown in Fig. 6.4 (a) behave qualitatively comparable, but more pronounced, to the fermion case of Fig. 6.3 (a). The complete model calculation (solid, blue) already reaches a deviation of more than an order of magnitude at the threshold energy and having a trend seemingly parallel to the SM (solid, black) for energies above. Noticeable deviations from the pure SM prediction already start at an invariant mass of $m(W^\pm Z) \sim 1000$ GeV. The unitarized EFT (dotted, dark red) prediction falls below the naive EFT prediction (dotted, red) above invariant masses of $m(W^\pm Z) = 1500$ GeV and it almost coincides by chance with the complete model prediction for invariant masses of $m(W^\pm Z) \geq 3000$ GeV. The most prominent observation is, that the calculation with aQGCs from O_{T_2} only (solid, green) amounts to a small contribution to the predicted events which will be more than an order of magnitude below the contribution of the full set of T-operators. This is clearly in contrast to the behavior in the case of an underlying fermion model. A possible explanation of the large anomalous contribution in the EFT calculation of the underlying scalar model is a strong constructive interference of the individual T-operators.

Finally, we will examine the results of the ZZ production subprocess which is shown in Fig. 6.5. The predictions of the ZZ production share most of the general features with

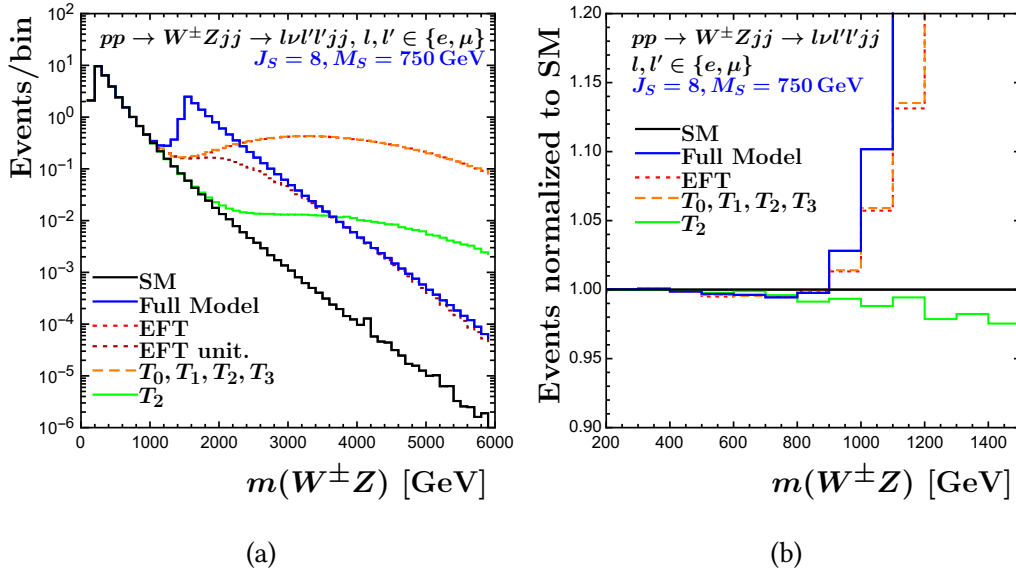


Figure 6.4.: Predicted event number per bin (100 GeV) for VBS with $W^\pm Z$ final state in the full $pp \rightarrow l\nu l' \nu jj$ process as a function of the invariant mass of the final state two boson system $m(W^\pm Z)$ where the aQGCs are induced by an additional scalar multiplet ($J_S = 8$, $M_S = 750 \text{ GeV}$). We present (a) the distribution of predicted events over the whole energy range from $200 \text{ GeV} < m(W^\pm Z) < 6000 \text{ GeV}$ and (b) the predicted events normalized to the SM prediction for the low-energy regime $200 \text{ GeV} < m(W^\pm Z) < 1500 \text{ GeV}$.

the $W^\pm Z$ production, when comparing Figs. 6.5 (a) and (b) with Figs. 6.3 (a) and 6.4 (b), respectively. Among those are:

- The peak structure of the loop calculation (solid, blue) which is more pronounced in the scalar case.
- Strong suppression in the high-energy region due to the parton distribution functions in number of predicted events for the pure SM (solid, black), the loop (solid, blue) and the unitarized EFT (dotted, dark red).
- Unphysical number of events in the non-unitarized prediction of EFT operators.
- Predictions using the set of T-operators (dashed, orange) coincides well within statistics with the full EFT basis predictions (dotted, red).
- Cancellation between contributions of individual T-operators in the fermion case.
- Amplification between contributions of individual T-operators in the scalar case.

The low-energy behavior, however, exhibits qualitative difference between the two VBS subprocesses, which is due to the constructive interference of the anomalous $W^\pm W^\mp \rightarrow ZZ$ and $ZZ \rightarrow ZZ$ subprocesses contribution with the SM contribution. Therefore, the full model prediction (solid, blue) shows a $> 5\%$ deviation from the SM (solid, black) already at $m(ZZ) \sim 800 \text{ GeV}$ for the fermion case and $m(ZZ) \sim 700 \text{ GeV}$ for the scalar case, which

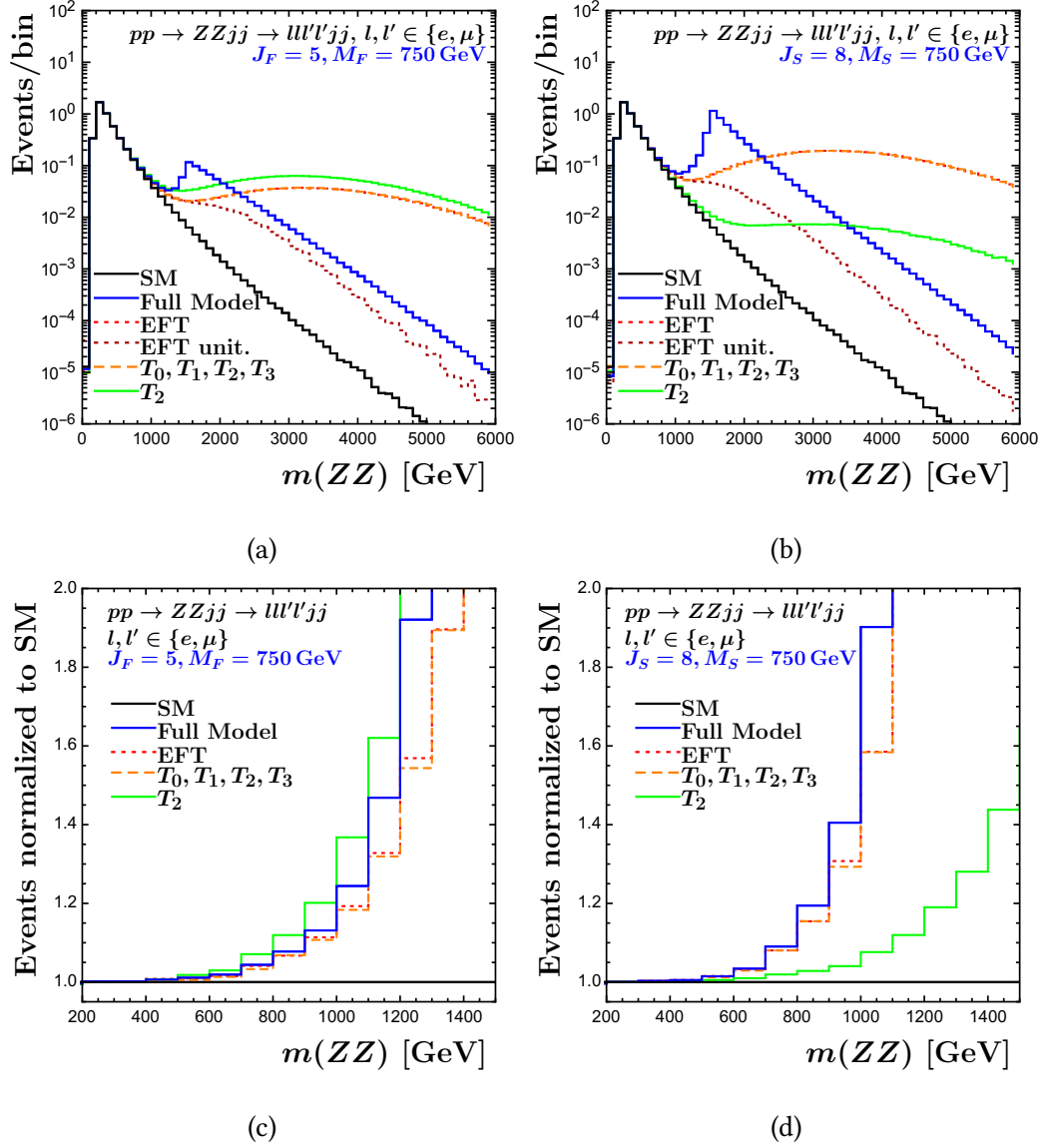


Figure 6.5.: Predicted event number per bin (100 GeV) for VBS with ZZ final state in the full $pp \rightarrow ll'l'jj$ process as a function of the invariant mass of the final state two boson system $m(ZZ)$ where the aQGCs are induced by an additional fermion multiplet ($J_F = 5, M_F = 750$ GeV) or an additional scalar multiplet ($J_S = 8, M_S = 750$ GeV), respectively. We present the distribution of predicted events over the whole energy range from $200 \text{ GeV} < m(ZZ) < 6000 \text{ GeV}$ (a) in the fermion case and (b) in the scalar case, and the predicted events normalized to the SM prediction for the low-energy regime $200 \text{ GeV} < m(ZZ) < 1500 \text{ GeV}$ (c) in the fermion case and (d) in the scalar case, respectively.

is different to the values of $W^\pm Z$ final state, where the deviation remains below 5% up to $m(W^\pm Z) \geq 1000$ GeV. In addition, the difference between the full model and the EFT prediction (dotted, red) rises above 5% for invariant masses $m(ZZ) \geq 1000$ GeV for the fermion case and $m(ZZ) \sim 800$ GeV for the scalar case. Hence, the EFT is valid for a larger

energy range in the case of a process with destructive interference like $W^\pm Z$ production, in comparison with a case of constructive interference like ZZ production. This resembles the same behavior as observed in the on-shell processes of $W^\pm W^\mp \rightarrow ZZ$ and $W^\pm Z \rightarrow W^\pm Z$ scattering depicted in Fig. 5.6. The rise of the cross section for lower invariant masses due to the constructive interference also leads to a violation of the unitarity bound of the naive EFT calculation at lower invariant masses. This can be observed by the deviation of the predicted number of events from the naive and the unitarized EFT calculation that sets in at $m(ZZ) \sim 1500$ GeV for the fermion case and $m(ZZ) \sim 1200$ GeV for the scalar case of the ZZ production.

We close this section with a summary of our observations. The full model exhibits a distinct peak structure around the threshold for pair production, which is clearly visible above the pure SM prediction. The EFT only has a small low-energy validity region, as it cannot reproduce the rise to the peak of the full model. In the case of the $W^\pm Z$ production the validity of the EFT has a wider range than in the case of ZZ production due to the different interference behavior. The T-operators dominate the full EFT contribution and, hence, give an accurate approximation of the full EFT calculation. Therefore, the low-energy behavior of our specific full model is well covered by dimension 8 operators. The prediction using the unitarised EFT leads to a high-energy behavior that would be allowed by a general unitarity principle. However, the unitarised EFT may only exhibit the same high-energy behavior as the full model coincidentally, as can be seen in the $W^\pm Z$ production with the underlying scalar model. In all other cases, this was not satisfied. The fermion and the scalar model share most qualitative features, which are more pronounced in the scalar case. The main difference occurs in the contributions of the T-operators. In the fermion case we observe a cancellation among contributions of individual T-operators whereas they lead to amplification in the scalar case. This can be concluded from comparing the predicted number of events using O_{T_2} alone as anomalous contribution with the predicted number of events following from the full set of T-operators. An explanation is given by the different signs of the Wilson coefficients $\frac{f_{T_0}}{\Lambda^4}$ and $\frac{f_{T_1}}{\Lambda^4}$ for the fermion and scalar model, as it was discussed in Section 4.3. Thus, correlations of the Wilson coefficients of EFT operators arising from the underlying model are of relevance.

6.5. Implications for experimental analysis

Having discussed features of our toy model and its derived EFT approximation in detail, we finally compare our findings with experimental analyses which set bounds on EFT operators. We will refer to the analysis for $W^\pm Z$ production of Ref. [6] and to the analysis for ZZ production of Ref. [7]. First, we review the explicit bounds on Wilson coefficients that are determined by both analysis and compare to the Wilson coefficients which are given by our model parameters.

Table 6.1 shows the bounds on Wilson coefficients of the T-operators as determined in Refs. [6, 7]. The limits are obtained in individual fits, i.e. using the contribution from one operator alone. In addition, we list the corresponding Wilson coefficients that emerge from an underlying fermion multiplet or scalar multiplet of our toy-model for the previously discussed cases with $J_F = 5$, $M_F = 750$ GeV and $J_S = 8$, $M_S = 750$ GeV, respectively. We

Wilson coefficient	$W^\pm Z$ bounds	ZZ bounds	fermion case	scalar case
$\frac{f_{T_0}}{\Lambda^4}$	$[-0.75, 0.81]$	$[-0.46, 0.44]$	-0.278	0.308
$\frac{f_{T_1}}{\Lambda^4}$	$[-0.49, 0.55]$	$[-0.61, 0.61]$	-0.548	0.617
$\frac{f_{T_2}}{\Lambda^4}$	$[-1.49, 1.85]$	$[-1.2, 1.2]$	1.454	0.484
$\frac{f_{T_3}}{\Lambda^4}$	-	-	0.859	0.256

Table 6.1.: Experimental bounds on the Wilson coefficients of the T-operators in units of TeV^{-4} as given by the $W^\pm Z$ production analysis of Ref. [6] and by the ZZ production analysis of Ref. [7], respectively. We compare with the corresponding Wilson coefficients for our toy model with one underlying fermion multiplet with $J_F = 5$ and $M_F = 750$ GeV or one underlying scalar multiplet with $J_S = 8$ and $M_S = 750$ GeV.

see that the stronger bounds on $\frac{f_{T_0}}{\Lambda^4}$ and $\frac{f_{T_2}}{\Lambda^4}$ arise from the ZZ analysis of Ref. [7]. In the latter publication, also an estimation at which invariant mass the operators with Wilson coefficients of the estimated bounds violate unitarity. The unitarity violation emerges at $m(ZZ) \sim 2.3 - 2.5$ TeV depending on the analyzed operator. Ref. [6] poses the stronger bound on $\frac{f_{T_1}}{\Lambda^4}$. We demonstrate that our model parameters were chosen such that one Wilson coefficient matches with the most stringent bound, which is given by $\frac{f_{T_1}}{\Lambda^4}$. Hence, both multiplets would be disfavored due to the bound on $\frac{f_{T_1}}{\Lambda^4}$ from the $W^\pm Z$ analysis, and the scalar multiplet amounts even for a higher value of $\frac{f_{T_1}}{\Lambda^4}$ than given by the bound from the ZZ analysis. Whilst all other Wilson coefficients in the scalar case have values below the bound, the value of $\frac{f_{T_2}}{\Lambda^4}$ of the fermion multiplet is above its estimated bound from the ZZ analysis and below the bound from the $W^\pm Z$ analysis. Table 6.1 also highlights the different signs of the Wilson coefficients in the fermion case, whereas in the scalar case all Wilson coefficients appear with the same sign. This indicates the cancellation among individual contributions of the T-operators in the fermion case, leading to cancellations between the contributions of $\frac{f_{T_1}}{\Lambda^4}$ and $\frac{f_{T_2}}{\Lambda^4}$, whereas in the scalar case all contributions add up leading to a much higher number of predicted events as discussed in Section 6.4.

We record, that the $\frac{f_{T_2}}{\Lambda^4}$ contribution calculated in the fermion case should give a reasonable measure of the estimated bound given by experimental analysis in the comparison with the results from Refs. [6, 7].

Subsequently, we compare the predictions of our model with the experimental analysis and formulate implications for estimations of future bounds on aQGCs. We recap, the examination of the $W^\pm Z$ production incorporates the full EW processes

$$pp \rightarrow W^\pm Z jj \rightarrow l'^{\pm} \nu_l l^{\pm} l^{\mp} jj,$$

with $l, l' \in \{e, \mu\}$. In their analysis [6], CMS used the transverse mass parameter of the $W^\pm Z$ system $m_T(W^\pm Z)$, which they define as[6]

$$m_T(W^\pm Z) = \sqrt{[E_T(W) + E_T(Z)]^2 - [\vec{p}_T(W^\pm) + \vec{P}_T(Z)]^2}, \quad (6.5)$$

with $E_T = \sqrt{m^2 + p_T^2}$ and m^2 denotes the invariant mass of the W^\pm or Z candidate. The W^\pm candidate is constructed from \vec{p}_T^{miss} and the associated lepton. Fig. 6.6 (a) demonstrates the CMS measurement for the $W^\pm Z$ production together with the expected contributions from different production processes which they use to determine the bounds on aQGCs. We want to stress out, that the last bin in the histogram contains all events with $m_T(W^\pm Z) > 1500$ GeV, including the region where the T-operators violate the unitarity limit. Fig. 6.6 (b) and (c) shows our prediction using an underlying fermion or scalar multiplet, respectively. The employed transverse mass and binning follows the CMS definition.

We need to validate the compatibility of our predictions with the work of CMS. Therefore, we consider our SM prediction (solid, black) in Fig. 6.6 (b) and (c) which should coincide with the SM EW-WZjj distribution of the CMS results (filled, purple) in Fig. 6.6 (a). We see a slight overestimation of our SM prediction for several bins, however, the overall behavior is well comparable. The predicted events in the range $200 \text{ GeV} < m_T(W^\pm Z) < 400 \text{ GeV}$ give the largest contribution and the contribution quickly declines for values of the transverse above. For $m_T(W^\pm Z) > 400 \text{ GeV}$, the regime where the anomalous contributions start to deviate from the SM prediction, the SM contribution from all different production processes gives a prediction close to zero. Hence, a comparison of our estimation with the CMS $W^\pm Z$ analysis can be performed directly.

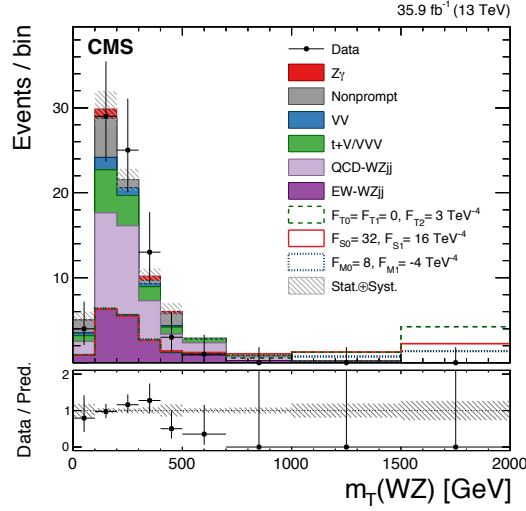
The CMS data points in Fig. 6.6 (a) show accordance within uncertainty with their theoretically predicted number of events without aQGCs. However, in the last three bins no events are measured given an uncertainty of approximate two events per bin. Following their prediction with aQGCs from the O_{T_2} operator alone (dashed, green) with a Wilson coefficient well above the estimated bound, we only observe discrepancy with the data for transverse masses in the last bin. Hence, the exclusion of Wilson coefficients is solely determined from the transverse mass region $m_T(W^\pm Z) > 1500 \text{ GeV}$ in which the EFT operators violate unitarity at some point.

Comparing with our predictions in the fermion case of Fig. 6.6 (b) there is no reason to rule out our full model (solid, blue) by the given measurement uncertainty, even though its derived Wilson coefficient of the O_{T_1} operator is above the determined bound. Moreover, the prediction of the complete set of T-operators (dashed, orange) is also compatible with the measurement. Only the prediction for the single O_{T_2} operator (solid, green) is slightly above the allowed region. For the scalar case in Fig. 6.6 (c) the picture is different. The full model (solid, blue) is ruled out by the measurement, as the predictions for the last two bins obviously exceed the data. This is caused by the high rise of the cross section in the vicinity of the peak, as was seen in Fig. 6.4. The prediction of the full set of T-operators (dashed, orange) is also ruled out due to the number of events in the last bin. The predicted events for the single O_{T_2} operator (solid, green), however, are well within the allowed region for all bins. The unitarized EFT prediction (dotted, dark red) for the fermion and scalar both are in agreement with the data.

In the ZZ production process the full EW processes read

$$pp \rightarrow ZZjj \rightarrow l'^{\pm} l'^{\mp} l^{\pm} l^{\mp} jj,$$

with $l, l' \in \{e, \mu\}$. For the presentation of their data used to set bounds on Wilson coefficients, CMS used the invariant mass of the ZZ system $m(ZZ)$ [7]. We present the



(a) “ $m_T(WZ)$ for events satisfying the EW signal selection, used to place constraints on the anomalous coupling parameters. The dashed lines show predictions for several aQGC parameters values that modify the EW WZ process. The last bin contains all events with $m_T(WZ) > 2000$ GeV. The hatched bands represent the total and relative systematic uncertainties on the predicted yields. The bottom panel shows the ratio of the number of events measured in data to the total number of expected events. The predicted yields are shown with their best-fit normalizations from the background-only fit.” Image and caption taken from Ref. [6].

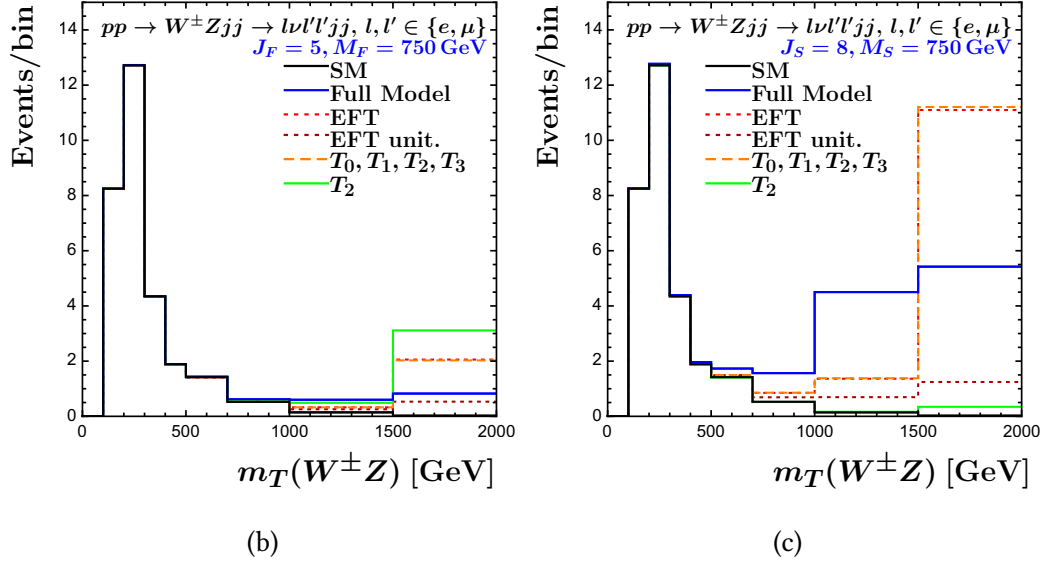
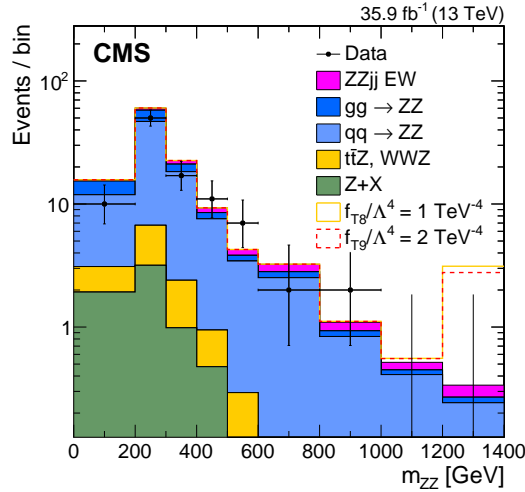
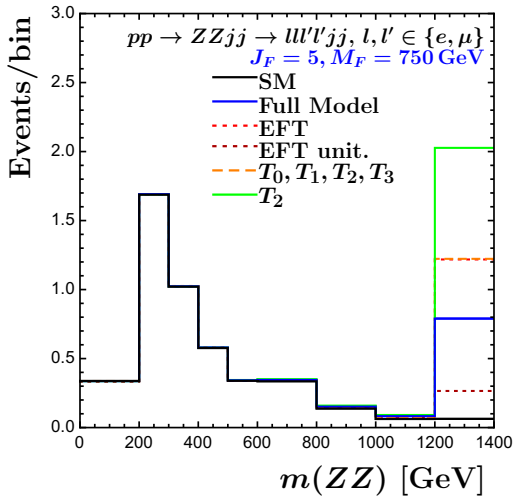


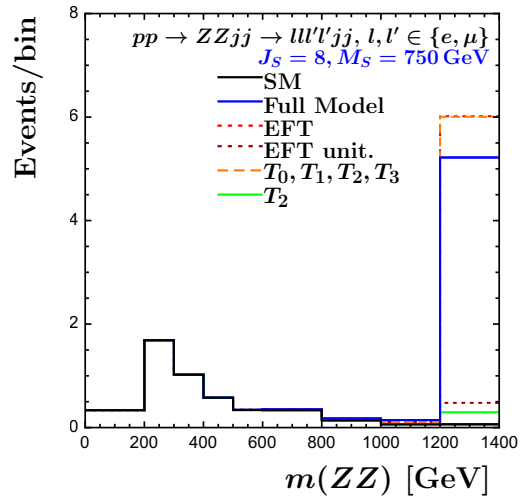
Figure 6.6.: Comparison of events in VBS scattering with $W^\pm Z$ final states applying the CMS signal selection with the theoretical predicted number as a function of the transverse mass of the $W^\pm Z$ system. We show (a) the CMS analysis result, as presented in Ref. [6], and our predicted results for aQGCs (b) for an additional fermion multiplet and (c) for an additional scalar multiplet. The definition of $m_T(W^\pm Z)$ and the binning in (b) and (c) is chosen to match the CMS analysis.



(a) “The $m(ZZ)$ distribution in the $ZZjj$ selection together with the SM prediction and two hypotheses for the aQGC coupling strengths. Points represent the data, filled histograms the expected signal and background contributions. The last bin includes all contributions with $m(ZZ) > 1200$ GeV.” Image and caption taken from Ref. [7].



(b)



(c)

Figure 6.7.: Comparison of events VBS scattering with ZZ final states applying the CMS signal selection with the theoretical predicted number as a function of the invariant mass of the ZZ system. We show (a) the CMS analysis result, as presented in Ref.[7], and our estimated results for aQGCs (b) for an additional fermion multiplet and (c) for an additional scalar multiplet. The binning in (b) and (c) is chosen to match the CMS analysis.

results of Ref. [7] together with our prediction for ZZ production using our model with an underlying fermion or scalar multiplet in Fig. 6.7. The last bin involves all invariant masses with $m(ZZ) > 1200$ GeV. As in the previous case of the comparison in $W^\pm Z$ production, we first focus on the SM prediction in order to cross check for comparability. The reference prediction is given by the $ZZjj$ EW distribution of the CMS analysis (filled, magenta)

which is presented on top of the other contributions in their prediction of Fig. 6.7 (a). Our estimation of the SM contribution (solid, black) in Figs. 6.7 (b) and (c) is in perfect agreement with the CMS values, as both yield a small and decreasing number of predicted events for $200 \text{ GeV} < m(ZZ) < 400 \text{ GeV}$ leading to less than one event per bin for invariant masses above for the 400 GeV. For invariant masses above 1000 GeV, the pure SM prediction including all production processes remains below one event per bin.

After the successful cross check of the SM prediction the subsequent discussion proceeds similarly as in the case of the comparison in $W^\pm Z$ production. In the results of the CMS analysis [7] there are no events found for the last two bins in the data, for which they determine an uncertainty of approximate two events per bin. The bounds on Wilson coefficients for single operators is again determined by the excess of predicted number of events above the data uncertainty for invariant masses of $m(ZZ) > 1200 \text{ GeV}$.

Turning our attention to the predictions of our model with an underlying fermion multiplet in Figs. 6.7 (b) we find no events beyond the uncertainty for the full model calculation (solid, blue). Also the set of T-operators (dashed, orange) is well compatible with the data. Only the predicted events in the last bin for the calculation using aQGCs of the single O_{T_2} are in the vicinity of the uncertainty maximum. This was expected, since the corresponding Wilson coefficient is slightly above the estimated bound from the ZZ production analysis of CMS in Table 6.1. In the scalar case, the full model (solid, blue) and the set of T-operators (dashed, orange) are obviously ruled out by the data, whereas the O_{T_2} prediction (solid, green) is acceptable in this case. Both unitarized EFT calculations (dotted, dark red) result in predictions well compatible with the data.

We briefly summarize the observations of this section in the following: On the one hand, in the case of the scalar model the exclusion due to the dominant T-operator is rather reasonable, since we have an amplification between the individual T-operator contributions which already resemble the behavior of the full EFT approximation, as seen in Section 6.4. Thus, if the contribution of one operator alone exceeds its experimental bound we can rule out the model. However, if we include all relevant operators, the bounds can be pushed to lower values for the individual dominant Wilson coefficients and, therefore, we could exclude scalar multiplets with lower representations than $J_S = 8$.³

On the other hand, we should not use the bound given by one single Wilson coefficient in order to disregard our model with a fermion multiplet, as we have obvious cancellations among the contributions of individual T-operators. Hence, the resulting number of events of the combination of operators is lower than the yield of some individual operators.

The unitarized EFT should also be taken with care, since it damps all contributions below the exclusion limit. This therefore allows for much higher values of the Wilson coefficients. The underlying models leading to such high coefficients, however, would be far from being reasonable in the case of one fermion or scalar $SU(2)_L$ multiplet, as they are not perturbative as well. Furthermore, referring to the discussion of Section 6.4, we see that the unitarized EFT does not resemble the high-energy behavior of the full model, what is assumed to be a feature of the loop-induced nature of the EFT operators.

We conclude, that setting limits on single Wilson coefficients of operators by their contribution in the regime where unitarity is violated does not result in an appropriate

³Also the discussion of unitarity violation in Appendix A.6 would lead to this result.

measure in order to disregard specific models, in general. We found out, that considering correlations for the underlying model can improve the discussion for some cases. Nevertheless, this does not cure the unitarity violation of the EFT prediction in the high-energy regime. The unitarity violation can be cured by an unitarization procedure. However, in the case of our model with a loop-induced EFT approximation, the unitarized EFT cannot describe the behavior of the underlying model beyond the validity region of the original EFT and, hence, is not suitable for determining bounds on our toy-model parameters.

7. Summary and conclusion

Any EFT, by construction, is only meant to be valid in a limited kinematic regime. Using an EFT as a tool in the search of high-energy physics beyond the SM, its validity region is bounded by the energy scale at which the use of the complete underlying model is inevitable. The aim of the present thesis is to analyze the validity region of an EFT application in the case of VBS, and to observe the discrepancy to the underlying model in the transition to the high-energy regime. In addition, we investigate how contributions from EFT operators interfere and determine the dominant subset of EFT operators. All calculations are carried out in the $SU(2)_L$ limit of the SM.

For this purpose, a short introduction into the idea of EFTs is given. After formulating our assumptions for the underlying model, a complete EFT basis up to energy dimension 8 is constructed. We review the implications of unitarity on $2 \rightarrow 2$ scattering processes and derive the unitarity bounds in their common formulation. We propose an underlying toy-model, which includes new fermion and scalar multiplets that transform under a representation of the $SU(2)_L$. For its impact on VBS, we calculate the one-loop correction of the vector-boson vertices and perform the associated renormalization in the \overline{MS} scheme. Setting the isospin of the representation of a multiplet J_R enables a tuning of the coupling, as the vertex corrections appear with representation factors $T_R \sim J_R^3$ and $T_R C_{2,R} \sim J_R^5$. The identification of the low-energy approximation of the vertex corrections with the EFT vertices of our complete basis leads to the determination of the Wilson coefficients.

For a phenomenological analysis of the VBS processes we choose a single underlying fermion or scalar multiplet with mass $M = 750$ GeV and isospin such that at least one Wilson coefficient is in the ballpark of current experimental bounds on aQGCs from Ref. [6]. We therefore make sure, that our new-physics (NP) model has a maximal impact on VBS. Comparison of the cross section in different energy regions show a good accordance between the EFT and full loop calculation in the low-energy regime. However, the validity region is fairly limited due to strong discrepancy in the vicinity of the peak when the COM energy approaches the threshold for pair production of the loop particles. The investigation of the NP contribution from the full model to the helicity amplitudes in the on-shell scattering indicates that only a small subset of helicity amplitudes give a non-negligible contribution to the cross section. The first partial-wave (PW) coefficients up to the $j = 2$ PW are calculated for the non-negligible helicity amplitudes and we verified, that this finite PW expansion is an adequate approximation of the contribution of our model to on-shell VBS. The dominant eigenvalues are constructed for a check of unitarity. It turns out, that the case of a fermion multiplet contribution is compatible with the unitarity bound. The scalar case, on the other hand, does not fulfill this condition, indicating that the model is not perturbative.

With the use of the on-shell calculated PW coefficients, we included an approximation of our model in VBFNLO as a contribution to anomalous couplings of VBS. This enables us

to investigate our model prediction of VBS at a proton-proton collider. After the necessary consistency check of the implementation, we demonstrate the prediction for $W^\pm Z$ and ZZ production events and our results are compared with the experimental analyses of Refs. [6, 7]. Our findings lead to the following conclusions:

With the choice of our underlying model parameters, we clearly see that the dominant contribution to the EFT calculation follows from the complete set of T-operators for VBS topologies. Whereas we find in the case of on-shell scattering a deviation in the very low-energy regime to the full EFT calculation due to the relevance of dimension 6 operators, we cannot distinguish the contribution for the complete set of T-operators from the full EFT in the prediction of VBS events at proton-proton colliders. This behavior was already expected from the observation of current bounds on the parameter space of one multiplet in Section 4.3. Thus, we demonstrated that models do exist for which an analysis of the aQGCs from dimension 8 EFT operators alone suffices to parameterize the relevant low-energy physics in VBS. However, since the T-operators are only obtainable from integrating out loop contributions of heavy, charged particles, the EFT is limited in energy range, since it fails reproduce the peak structure of the full model. In the case of destructive interference, like for $W^\pm Z$ production, the EFT validity region is slightly extended in comparison to the case of constructive interference, like for ZZ production. A sizable deviation from the pure SM prediction emerges only at higher energies in the case of destructive interference. So, the validity of the EFT is bounded to energies, where the contributions from our still perturbative model are almost indistinguishable from the SM prediction. Hence, it would be very difficult to observe effects in experiments. This limitation also cannot be extended with the application of a unitarization procedure, because the high-energy behavior of the underlying model does not get restored. An agreement in the high-energy region only appears coincidentally.

The comparison of single T-operator contribution with the full set of T-operators shows a clear distinction between the fermion and the scalar case which is apparent in the sign differences of the individual Wilson coefficients in the two cases, as seen in Section 4.3 and in Table 6.1. Depending on the type of underlying model, we therefore expect an occurrence of different correlations between individual Wilson coefficients. In the comparison with the experimental analyses of Refs. [6, 7], we noticed that including the full set of T-operators could improve the evaluation of compatibility with the data in the case of our model with one fermion or scalar multiplet. However, the problem of unitarity violation of the naive EFT prediction would still be unsolved in that case.

We therefore infer that future analyses of EFT in VBS should not only work with single operators, but also include subsets of operators which are motivated by the underlying model type that is probed. For those subsets, a global analysis of the Wilson coefficients or imposing correlations estimated by theoretical considerations should be performed. A further investigation of different particle combinations of our generic model, or including extensions to add an interaction with the Higgs field or the hypercharge field, could deepen the understanding about correlations of Wilson coefficients and its effect on the EFT investigation. However, as the limited validity region of the EFT and the unitarity violation of the prediction needs to be considered, it might be inevitable to work with UV-complete models, or at least to apply a unitarization procedure to the EFT operators, if the high-energy region is probed.

A. Appendix

A.1. One-loop calculations

In this chapter we want to follow on the short introduction given in Section 2.3. We first recap the defined tensor integral from Eq. (2.27)

$$T^{\mu_1 \dots \mu_p} = \frac{\mu^{4-d}}{(2\pi)^d} \int d^d k \frac{k^{\mu_1} \dots k^{\mu_p}}{D_0 D_1 \dots D_{n-1}}. \quad (\text{A.1})$$

In section A.1.1 we will describe general procedures in manipulating tensor integrals resulting in a full decomposition into a small set of master integrals. We will also demonstrate, how those master integrals can be expanded at low energies or, likewise, small momenta, such that we will be able to provide an analytic approximation for the tensor integrals. Subsequently we present the basic idea behind the Passarino-Veltman (PV) decomposition in Appendix A.1.2.

A.1.1. Master integral prescription

In the discussion of this section we will restrict us to the case of an one-loop integration with all propagators having the same mass, e.g. $D_i = (k + r_i)^2 - M^2$. The first step in the manipulation of tensor integrals of the form in Eqs. (2.27) and (A.1) will make use of the Feynman parametrization, which is defined as follows:

$$\frac{1}{A_0 \dots A_{n-1}} = (n-1)! \int_0^1 dx_0 \dots dx_{n-1} \frac{\delta(1 - x_0 - \dots - x_{n-1})}{[x_0 A_0 + \dots x_{n-1} A_{n-1}]^n}. \quad (\text{A.2})$$

Hence, we can rewrite

$$\begin{aligned} T^{\mu_1 \dots \mu_p} &= (n-1)! \int_0^1 dx_0 \dots dx_{n-1} \delta(1 - x_0 - \dots - x_{n-1}) \frac{\mu^{4-d}}{(2\pi)^d} \int d^d k \frac{k^{\mu_1} \dots k^{\mu_p}}{[x_0 D_0 + \dots x_{n-1} D_{n-1}]^n} \\ &= (n-1)! \int_0^1 dx_0 \dots dx_{n-1} \delta(1 - x_0 - \dots - x_{n-1}) \frac{\mu^{4-d}}{(2\pi)^d} \int d^d k \frac{k^{\mu_1} \dots k^{\mu_p}}{[(k + P)^2 - C^2]^n} \\ &=: (n-1)! \int_0^1 dx_0 \dots dx_{n-1} \delta(1 - x_0 - \dots - x_{n-1}) \mathcal{I}_n^{\mu_1 \dots \mu_p}, \end{aligned} \quad (\text{A.3})$$

where we simplified the denominator in the second line and introduced the d -dimensional momentum integrals $\mathcal{I}_n^{\mu_1 \dots \mu_p}$ containing the tensor structure $k^{\mu_1} \dots k^{\mu_p}$. The momentum P is defined as

$$P = x_1 r_1 + \dots x_{n-1} r_{n-1}, \quad (\text{A.4})$$

and the mass quantity C is defined through

$$C^2 = M^2 + P^2 - x_1 r_1^2 - \dots - x_{n-1} r_{n-1}^2. \quad (\text{A.5})$$

In the case of a $2 \rightarrow 2$ scattering of vector bosons, we only have to consider tensors up to four Lorentz indices. Therefore we need to evaluate the set

$$\mathcal{I}_n = \mu^{4-d} \int \frac{d^d k}{(2\pi)^d} \frac{1}{[(k+P)^2 - C^2]^n}, \quad (\text{A.6a})$$

$$\mathcal{I}_n^\mu = \mu^{4-d} \int \frac{d^d k}{(2\pi)^d} \frac{k^\mu}{[(k+P)^2 - C^2]^n}, \quad (\text{A.6b})$$

$$\mathcal{I}_n^{\mu\nu} = \mu^{4-d} \int \frac{d^d k}{(2\pi)^d} \frac{k^\mu k^\nu}{[(k+P)^2 - C^2]^n}, \quad (\text{A.6c})$$

$$\mathcal{I}_n^{\mu\nu\alpha} = \mu^{4-d} \int \frac{d^d k}{(2\pi)^d} \frac{k^\mu k^\nu k^\alpha}{[(k+P)^2 - C^2]^n}, \quad (\text{A.6d})$$

$$\mathcal{I}_n^{\mu\nu\alpha\beta} = \mu^{4-d} \int \frac{d^d k}{(2\pi)^d} \frac{k^\mu k^\nu k^\alpha k^\beta}{[(k+P)^2 - C^2]^n}, \quad (\text{A.6e})$$

for which we define our master integrals

$$I_{n,m} := \mu^{4-d} \int \frac{d^d k}{(2\pi)^d} \frac{(k^2)^m}{[k^2 - C^2]^n}. \quad (\text{A.7})$$

If we shift the integration momentum with $k \rightarrow k - P$ in the integrals of Eq. (A.6) we can decompose all the tensorial dependence on products of the momentum P^{μ_i} and/or the (d -dimensional!) metric $g^{\mu_i \mu_j}$. The result reads as follows:

$$\mathcal{I}_n = I_{n,0}, \quad (\text{A.8a})$$

$$\mathcal{I}_n^\mu = -P^\mu I_{n,0}, \quad (\text{A.8b})$$

$$\mathcal{I}_n^{\mu\nu} = P^\mu P^\nu I_{n,0} + \frac{g^{\mu\nu}}{d} I_{n,1}, \quad (\text{A.8c})$$

$$\mathcal{I}_n^{\mu\nu\alpha} = -P^\mu P^\nu P^\alpha I_{n,0} - \frac{1}{d} (P^\mu g^{\nu\alpha} + P^\nu g^{\alpha\mu} + P^\alpha g^{\mu\nu}) I_{n,1}, \quad (\text{A.8d})$$

$$\begin{aligned} \mathcal{I}_n^{\mu\nu\alpha\beta} = & P^\mu P^\nu P^\alpha P^\beta I_{n,0} + \frac{1}{d} (P^\mu P^\nu g^{\alpha\beta} + P^\mu P^\alpha g^{\nu\beta} + P^\mu P^\beta g^{\nu\alpha} + P^\nu P^\alpha g^{\mu\beta} \\ & + P^\nu P^\beta g^{\mu\alpha} + P^\alpha P^\beta g^{\mu\nu}) I_{n,1} + \frac{1}{d(d+2)} (g^{\mu\nu} g^{\alpha\beta} + g^{\mu\alpha} g^{\nu\beta} + g^{\mu\beta} g^{\nu\alpha}) I_{n,2}. \end{aligned} \quad (\text{A.8e})$$

We motivate this result for the example of $\mathcal{I}_n^{\mu\nu}$. Shifting the momentum $k \rightarrow k - P$ in $\mathcal{I}_n^{\mu\nu}$ leads to

$$\begin{aligned} \mathcal{I}_n^{\mu\nu} &= P^\mu P^\nu \mu^{4-d} \int \frac{d^d k}{(2\pi)^d} \frac{1}{[k^2 - C^2]^n} + \mu^{4-d} \int \frac{d^d k}{(2\pi)^d} \frac{k^\mu k^\nu}{[k^2 - C^2]^n} \\ &= P^\mu P^\nu I_n + N' g^{\mu\nu} I_{n,1}, \end{aligned} \quad (\text{A.9})$$

where we used the fact, that the second integral on the right hand side of the first line vanishes for $\mu \neq \nu$ due to symmetry reasons, such that its tensor structure can only be

proportional to the metric. We still have to determine the normalization factor N' using the identity

$$I_{n,1} = [g_{\mu\nu} \mathcal{I}_n^{\mu\nu}]_{P=0} = N' g_{\mu\nu} g^{\mu\nu} I_{n,1} = N' dI_{n,1}. \quad (\text{A.10})$$

Proceeding analogously with the other integrals in Eq. (A.6) will result in the relations of Eq. (A.8).

We chose the decomposition into the master integrals $I_{n,m}$ as the integration can be performed analytically. After Wick rotating the integration contour from the real axis to the imaginary axis, the resulting integral is evaluated using d -dimensional spherical coordinates. After rescaling the radial part, the final radial integration can be expressed in terms of the Euler β -function. A detailed derivation can be found in many textbooks on QFT, e.g. in Ref. [12]. The expression of the master integral reads

$$I_{n,m} = (-1)^{m-n} \frac{i}{16\pi^2} (4\pi\mu^2)^{\frac{4-d}{2}} \frac{\Gamma(m + \frac{d}{2}) \Gamma(n - m - \frac{d}{2})}{\Gamma(\frac{d}{2}) \Gamma(n)} (C^2)^{m-n+\frac{d}{2}}, \quad (\text{A.11})$$

where $\Gamma(z)$ is the Euler Γ -function, which serves as analytical continuation of the factorial and is defined by

$$\Gamma(z) = \int_0^\infty t^{z-1} e^{-t} dt. \quad (\text{A.12})$$

The main property of the Γ -function is therefore $\Gamma(z+1) = z\Gamma(z)$ and it has simple poles at $z = 0, -1, -2, \dots$, which may lead to factors of $\frac{1}{\epsilon}$ when evaluated at $d \rightarrow 4 - 2\epsilon$, e.g.

$$\Gamma\left(\frac{4-d}{2}\right) \rightarrow \Gamma(\epsilon) = \frac{1}{\epsilon} - \gamma_E + \mathcal{O}(\epsilon), \quad (\text{A.13})$$

with the Euler-Mascheroni constant γ_E . The factors $\frac{1}{\epsilon}$ appearing in the limit to the physical four space-time dimensions resemble the possible ultraviolet (UV) divergences of loop diagrams, but they are now parametrized such that we are able to renormalize the theory, as presented in Section 4.2.

In principal, inserting Eqs. (A.11) and (A.8) into Eq. (A.3) provides an analytic expression, but the Feynman parameter integration still needs to be performed, what usually is difficult analytically. Fortunately, we are only interested in the approximate expression for the low energy phase-space region of the external momenta. Thus, recalling Eq. (A.5)

$$C^2 = M^2 + P^2 - x_1 r_1^2 - \dots - x_{n-1} r_{n-1}^2 =: M^2 \left(1 + \frac{P'^2}{M^2}\right), \quad (\text{A.14})$$

where P'^2 is just a linear combination of products of external momenta, we can expand Eq. (A.11) in powers of $\frac{P'^2}{M^2}$, such that

$$I_{n,m} = (-1)^{m-n} \frac{i}{16\pi^2} (4\pi\mu^2)^{\frac{4-d}{2}} \frac{\Gamma(m + \frac{d}{2}) \Gamma(n - m - \frac{d}{2})}{\Gamma(\frac{d}{2}) \Gamma(n)} (M^2)^{m-n+\frac{d}{2}} \sum_{k=0}^{\infty} \frac{1}{k!} \frac{\Gamma(m - n + \frac{d}{2} + 1)}{\Gamma(m - n + \frac{d}{2} + 1 - k)} \left(\frac{P'^2}{M^2}\right)^k. \quad (\text{A.15})$$

In the above expression, we used the Taylor expansion

$$(1+x)^a = \sum_{k=0}^{\infty} \frac{1}{k!} \frac{\Gamma(a+1)}{\Gamma(a+1-k)} x^k \quad \text{for } a \notin \mathbb{N}_0. \quad (\text{A.16})$$

For our one-loop matching up to EFT dimension 8 operators in Section 4.3 we only take into account a finite sum up to the overall order of $\mathcal{O}\left(\frac{1}{M^4}\right)$ and, hence, the Feynman parameter integration of Eq. (A.3) will be easily performed, as the approximation of $I_{n,m}$ together with the momenta P^{μ_i} in Eq. (A.8) only amounts to a polynomial in the Feynman parameters.

A.1.2. Passarino-Veltman decomposition

Starting with a general tensor integral¹

$$N^{\mu_1 \dots \mu_p} = \frac{(2\pi\mu)^{4-d}}{i\pi^2} \int d^d k \frac{k^{\mu_1} \dots k^{\mu_p}}{D_0 D_1 \dots D_{n-1}}, \quad (\text{A.17})$$

the basic idea of the PV decomposition, as mentioned in Section 2.3, is to directly project the tensorial dependence onto products of the available external momenta and/or the metric. Contracting the external Lorentz coefficients with the metric and external momenta, the remaining PV coefficient functions can be in principal determined in terms of the basic functions through solving a linear equation system. Those basic functions are given by²

$$A_0(m^2) = \frac{(2\pi\mu)^{4-d}}{i\pi^2} \int d^d k \frac{1}{k^2 - m^2}, \quad (\text{A.18a})$$

$$B_0(p^2, m_0^2, m_1^2) = \frac{(2\pi\mu)^{4-d}}{i\pi^2} \int d^d k \frac{1}{(k^2 - m_0^2) ((k+p)^2 - m_1^2)}, \quad (\text{A.18b})$$

$$C_0(\{r_{ij}^2\}, \{m_i^2\}) = \frac{(2\pi\mu)^{4-d}}{i\pi^2} \int d^d k \frac{1}{(k^2 - m_0^2) ((k+r_1)^2 - m_1^2) ((k+r_2)^2 - m_2^2)}, \quad (\text{A.18c})$$

$$D_0(\{r_{ij}^2\}, \{m_i^2\}) = \frac{(2\pi\mu)^{4-d}}{i\pi^2} \int d^d k \frac{1}{(k^2 - m_0^2) ((k+r_1)^2 - m_1^2) ((k+r_2)^2 - m_2^2) ((k+r_3)^2 - m_3^2)}, \quad (\text{A.18d})$$

with $r_{ij} = r_i - r_j$ for all possible combinations of external momenta, including $r_{i0} = r_i$. Of course, there is usually no need to explicitly solve the system of linear equations, as there are more efficient algorithms for a direct numerical calculation of each coefficient function on the market, e.g. LoopTools [17]. Nevertheless, we want to further demonstrate the procedure for the specific case of a three-point tensor function.

¹Note, that the normalization of the tensor integral differs from Eq. (A.1). This way, the $\frac{i}{16\pi^2}$ factor appearing in Eq. (A.11) is already included, when substituting this integral definition into a one-loop calculation.

²It is common nomenclature, to denote tadpole functions with A , two-point functions B , three-point functions C and four-point functions D .

Let us define the tensor function

$$\begin{aligned}
C^{\mu\nu\rho} &= \frac{(2\pi\mu)^{4-d}}{i\pi^2} \int d^d k \frac{k^\mu k^\nu k^\rho}{(k^2 - m_0^2) ((k + r_1)^2 - m_1^2) ((k + r_2)^2 - m_2^2)} \\
&= \frac{(2\pi\mu)^{4-d}}{i\pi^2} \int d^d k \frac{k^\mu k^\nu k^\rho}{D_0 D_1 D_2}.
\end{aligned} \tag{A.19}$$

We note, that it is a function of the external momenta r_1 and r_2 , and of the masses of the loop particles m_0^2 , m_1^2 and m_2^2 . We now decompose the tensor function $C^{\mu\nu\rho}$ into coefficient functions of all possible combinations of momenta and metric tensors, resulting in

$$C^{\mu\nu\rho} = \sum_{i,j,k=1}^2 r_i^\mu r_j^\nu r_k^\rho C_{ijk} + \sum_{i=1}^2 (g^{\mu\nu} r_i^\rho + g^{\nu\rho} r_i^\mu + g^{\rho\mu} r_i^\nu) C_{00i}. \tag{A.20}$$

In order to find all equations needed for the determination of C_{ijk} and C_{00i} we would subsequently contract both sides of the previous equation with the metric and the momenta r_1 and r_2 . Using the identities in the integrand

$$k^2 = D_0 - m_0^2 \tag{A.21a}$$

$$r_1 \cdot k = \frac{1}{2} (D_1 - D_0 - (r_1^2 - m_1^2 + m_0^2)) \tag{A.21b}$$

$$r_2 \cdot k = \frac{1}{2} (D_2 - D_1 - (r_2^2 - m_2^2 - (r_1^2 - m_1^2))) , \tag{A.21c}$$

we are able to express the full contractions of $C^{\mu\nu\rho}$ on the left-hand side of Eq. (A.20) in terms of A_0 , B_0 and C_0 and, hence, get the equations for the determination of C_{ijk} and C_{00i} .

We end this section with a summary of the divergent parts of the PV functions that appear in our one-loop calculation presented in Section 4.1. Such a list is useful for the extraction of the divergent part in vertex corrections, in order to determine the counter terms needed for the renormalization of the theory, as is performed in Section 4.2.

PV function	UV divergent part
$A_0(m_0^2)$	$\Delta_\epsilon m_0^2$
$B_0(p^2, m_0^2, m_1^2)$	Δ_ϵ
$B_1(p^2, m_0^2, m_1^2)$	$-\frac{1}{2}\Delta_\epsilon$
$B_{00}(p^2, m_0^2, m_1^2)$	$\frac{1}{12}\Delta_\epsilon (3m_0^2 - 3m_1^2 - p^2)$
$B_{11}(p^2, m_0^2, m_1^2)$	$\frac{1}{3}\Delta_\epsilon$
$C_{00}(\{r_{ij}^2\}, \{m_i^2\})$	$\frac{1}{4}\Delta_\epsilon$
$C_{001}(\{r_{ij}^2\}, \{m_i^2\})$	$-\frac{1}{12}\Delta_\epsilon$
$C_{002}(\{r_{ij}^2\}, \{m_i^2\})$	$-\frac{1}{12}\Delta_\epsilon$
$D_{0000}(\{r_{ij}^2\}, \{m_i^2\})$	$\frac{1}{24}\Delta_\epsilon$

Table A.1.: Divergent part of the PV coefficient functions, as found in Ref. [36].

A.2. Feynman rules

The Feynman rules of the SM and our new-physics (NP) model are provided in this section. The relevant Feynman propagators read:

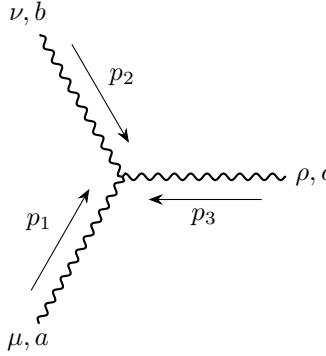
$$\mu, a \text{ ~~~~~ } \nu, b \quad = \frac{-i}{k^2 - m_W^2} \left(g^{\mu\nu} - \frac{k^\mu k^\nu}{m_W^2} \right) \delta^{ba}, \quad (\text{A.22a})$$

$$\text{-----} \overset{H}{\text{-----}} \quad = \frac{i}{k^2 - m_H^2}, \quad (\text{A.22b})$$

$$i \text{ --- } \blacktriangleright \text{ --- } j \quad = \frac{i (\gamma^\mu p_\mu + M_F)}{p^2 - M_F^2} \delta^{ji}, \quad (\text{A.22c})$$

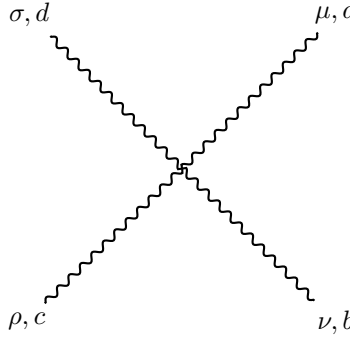
$$i \text{ - - - } \blacktriangleright \text{ - - - } j \quad = \frac{i}{p^2 - M_S^2} \delta^{ji}. \quad (\text{A.22d})$$

Vertices involving only SM particles are given by:



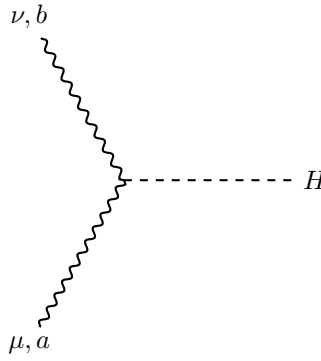
$$= g\epsilon^{abc} [g^{\mu\nu} (p1 - p2)^\rho + g^{\nu\rho} (p2 - p3)^\mu + g^{\rho\mu} (p3 - p1)^\nu] ,$$

(A.23a)



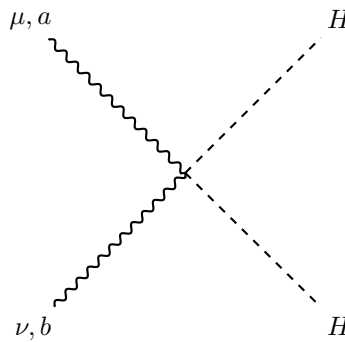
$$= ig^2 \begin{cases} \epsilon^{abn} \epsilon^{cdn} (g^{\mu\rho} g^{\nu\sigma} - g^{\mu\sigma} g^{\nu\rho}) \\ + \epsilon^{acn} \epsilon^{bdn} (g^{\mu\nu} g^{\rho\sigma} - g^{\mu\sigma} g^{\nu\rho}) , \\ + \epsilon^{adn} \epsilon^{bcn} (g^{\mu\nu} g^{\rho\sigma} - g^{\mu\rho} g^{\nu\sigma}) \end{cases} ,$$

(A.23b)



$$= \frac{i2m_W^2}{v} g^{\mu\nu} \delta^{ab} ,$$

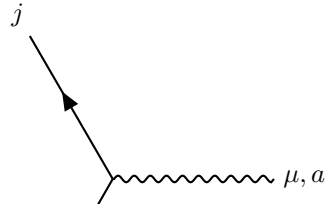
(A.23c)



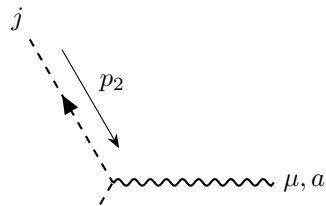
$$= \frac{i2m_W^2}{v} g^{\mu\nu} \delta^{ab} .$$

(A.23d)

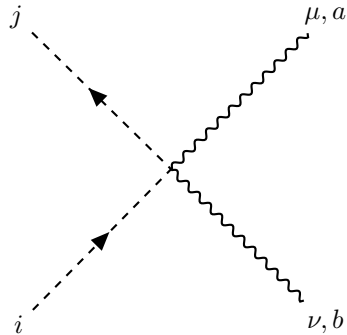
Lastly, our model induces the following new interactions:



$$= ig\gamma^\mu T_{Fji}^a, \quad (\text{A.24a})$$



$$= ig(p_1 - p_2)^\mu T_{Sji}^a, \quad (\text{A.24b})$$



$$= ig^2 g^{\mu\nu} \{T_S^a, T_S^b\}_{ji}. \quad (\text{A.24c})$$

The NP multiplets carry $SU(2)_L$ charge and, hence, their propagators have a specific direction of charge transport which is resembled by the propagator arrows. The rule for a closed loop of those multiplets will result in a trace in the isospin space of the representation, where the product order of generators inside the trace is given by going in opposite direction as indicated by the arrows.

A.3. Identities for the $\mathfrak{su}(2)_L$ algebra

In this section we want to derive all the $\mathfrak{su}(2)_L$ algebra rules, we need to apply for the construction of the EFT operators and their analysis presented in Section 3.1. Also we will evaluate the traces of up to four $SU(2)_L$ generators explicitly.

We start with general definitions, which will hold throughout the thesis. We denote a generator of the $SU(2)_L$ in a representation R with t_R^a . Hence, we have for a Lie-product of

two generators

$$[t_R^a, t_R^b] = i\epsilon^{abc}t_R^c, \quad (\text{A.25})$$

where the ϵ^{abc} -tensor is the structure constant of $\mathfrak{su}(2)_L$. Each representation R of $\mathfrak{su}(2)_L$ is classified by the isospin $J_R \in \{0, \frac{1}{2}, 1, \frac{3}{2}, \dots\}$ and has the dimension $2J_R + 1$. The generators in the defining representation are just given by $\frac{\tau^a}{2}$, where τ^a stand for the usual Pauli matrices. The covariant derivative is given by

$$D_\mu = \partial_\mu - ig t_R^a W_\mu^a, \quad (\text{A.26})$$

but we will highlight it with a circumflex, if we are talking about the covariant derivative in the defining representation, so

$$\hat{D}_\mu = \partial_\mu - ig \frac{\tau^a}{2} W_\mu^a. \quad (\text{A.27})$$

Also we want to highlight all fields in the adjoint representation which are contracted with the generators in the defining representation with a circumflex, e.g. the field-strength tensor which is given with the commutator of two covariant derivatives

$$\hat{W}_{\mu\nu} = \frac{1}{-ig} [\hat{D}_\mu, \hat{D}_\nu] = \frac{\tau^a}{2} W_{\mu\nu}^a. \quad (\text{A.28})$$

We can write the covariant derivative of a field Φ^a in adjoint space with the use of the defining representation $\hat{\Phi} = \Phi^a \frac{\tau^a}{2}$ in the form

$$[\hat{D}_\mu, \hat{\Phi}] = \frac{\tau^a}{2} \left(\partial_\mu \delta^{ac} + g\epsilon^{abc} W_\mu^b \right) \Phi^c = \frac{\tau^a}{2} D_\mu^{ac} \Phi^c. \quad (\text{A.29})$$

Therefore $[\hat{D}_\mu, \hat{\Phi}]$ is again a field in the adjoint representation contracted with one single generator.

We are now ready to derive the relations relevant for the thesis. We begin, with the integration by parts for a covariant derivative on fields in the adjoint representation. Let $\Phi_1^a, \dots, \Phi_n^a$ be fields in the adjoint representation and $\hat{\Phi}_i = \Phi_i^a \frac{\tau^a}{2}$. The integration by parts then reads

$$\begin{aligned} \text{Tr} \left([\hat{D}_\alpha, \hat{\Phi}_1] \hat{\Phi}_2 \dots \hat{\Phi}_n \right) &= \text{Tr} \left([\hat{D}_\alpha, \hat{\Phi}_1 \hat{\Phi}_2 \dots \hat{\Phi}_n] \right) - \text{Tr} \left(\hat{\Phi}_1 [\hat{D}_\alpha, \hat{\Phi}_2 \dots \hat{\Phi}_n] \right) \\ &= \text{Tr} \left([\partial_\alpha, \hat{\Phi}_1 \dots \hat{\Phi}_n] \right) - ig W_\alpha^a \text{Tr} \left(\left[\frac{\tau^a}{2}, \hat{\Phi}_1 \dots \hat{\Phi}_n \right] \right) - \text{Tr} \left(\hat{\Phi}_1 [\hat{D}_\alpha, \hat{\Phi}_2 \dots \hat{\Phi}_n] \right) \\ &= \partial_\alpha \text{Tr} \left(\hat{\Phi}_1 \dots \hat{\Phi}_n \right) - \text{Tr} \left(\hat{\Phi}_1 [\hat{D}_\alpha, \hat{\Phi}_2 \dots \hat{\Phi}_n] \right), \end{aligned} \quad (\text{A.30})$$

where we used in the third equality the fact, that the trace of the commutator of a product of generators vanishes due to cyclicity.

The Jacobi identity for covariant derivatives on field-strength tensors is easily proven, since

$$\begin{aligned} &[\hat{D}_\alpha, \hat{W}_{\beta\gamma}] + [\hat{D}_\beta, \hat{W}_{\gamma\alpha}] + [\hat{D}_\gamma, \hat{W}_{\alpha\beta}] \\ &= \frac{1}{-ig} \left([\hat{D}_\alpha, [\hat{D}_\beta, \hat{D}_\gamma]] + [\hat{D}_\beta, [\hat{D}_\gamma, \hat{D}_\alpha]] + [\hat{D}_\gamma, [\hat{D}_\alpha, \hat{D}_\beta]] \right) = 0. \end{aligned} \quad (\text{A.31})$$

For the relation of two antisymmetrized covariant derivatives in the adjoint representation, we start with the explicit form of two covariant derivatives acting on the field Φ^a , which results in

$$\begin{aligned} [\hat{D}_\alpha, [\hat{D}_\beta, \hat{\Phi}]] &= \frac{\tau^a}{2} D_\alpha{}^{ac} D_\beta{}^{ce} \Phi^e \\ &= \frac{\tau^a}{2} (\partial_\alpha \partial_\beta \delta^{ae} + g \epsilon^{abe} (\partial_\alpha W_\beta^b + W_\beta^b \partial_\alpha + W_\alpha^b \partial_\beta) + g^2 \epsilon^{abc} \epsilon^{cde} W_\alpha^b W_\beta^c) \Phi^e. \end{aligned} \quad (\text{A.32})$$

Antisymmetrizing Eq. (A.32) for $\alpha \leftrightarrow \beta$, we obtain

$$\begin{aligned} [\hat{D}_{[\alpha}, [\hat{D}_{\beta]}, \hat{\Phi}]] &= \frac{\tau^a}{2} g (\epsilon^{abe} (\partial_\alpha W_\beta^b - \partial_\beta W_\alpha^b) + g (\epsilon^{abc} \epsilon^{cde} - \epsilon^{adc} \epsilon^{cbe}) W_\alpha^b W_\beta^d) \Phi^e \\ &= g \epsilon^{abc} T^a W_{\alpha\beta}^b \Phi^c. \end{aligned} \quad (\text{A.33})$$

In the rest of this section we deal with the explicit evaluation of traces of generators in a representation R of the $SU(2)_L$.

The trace of two generators is given by

$$\text{Tr}(t_R^{a,b}) = T_R \delta^{ab}, \quad (\text{A.34})$$

which serves as the definition of the index T_R of a representation. For the $SU(2)_L$ generators in the common normalization the index is given by

$$T_R = \frac{J_R(J_R + 1)(2J_R + 1)}{3}, \quad (\text{A.35})$$

such that $T_{\text{def}} = \frac{1}{2}$ for the defining representation. The trace of three generators is given by

$$\text{Tr}(t_R^a t_R^b t_R^c) = \frac{1}{2} \left(\text{Tr}(t_R^a [t_R^b, t_R^c]) + \text{Tr}(t_R^a \{t_R^b, t_R^c\}) \right) = \frac{i}{2} T_R \epsilon^{abc}. \quad (\text{A.36})$$

Here, we used the fact, that there are no structure constants of the $\mathfrak{su}(2)_L$ other than δ^{ab} and ϵ^{abc} . Thus, each trace of three fields will be antisymmetric in the exchange of two fields, meaning

$$\text{Tr}(\hat{\Phi}_1 \hat{\Phi}_2 \hat{\Phi}_3) = -\text{Tr}(\hat{\Phi}_1 \hat{\Phi}_3 \hat{\Phi}_2). \quad (\text{A.37})$$

The subsection A.3.1 is dedicated to the general evaluation of traces of four generators of an arbitrary $\mathfrak{su}(n)$ algebra, which will result in Eq. (A.47). Here, we will only state the result for the $\mathfrak{su}(2)_L$ using the above mentioned argument on the $\mathfrak{su}(2)_L$ structure constants, hence

$$\begin{aligned} \text{Tr}(t_R^a t_R^b t_R^c t_R^d) &= \frac{1}{15} T_R (3C_{2,R} - 1) (\delta^{ab} \delta^{cd} + \delta^{ac} \delta^{bd} + \delta^{ad} \delta^{bc}) + \frac{1}{6} T_R (\epsilon^{adn} \epsilon^{bcn} - \epsilon^{abn} \epsilon^{cdn}) \\ &= \frac{1}{15} T_R (3C_{2,R} - 1) (\delta^{ab} \delta^{cd} + \delta^{ac} \delta^{bd} + \delta^{ad} \delta^{bc}) \\ &\quad + \frac{1}{6} T_R (\delta^{ab} \delta^{cd} - 2\delta^{ac} \delta^{bd} + \delta^{ad} \delta^{bc}), \end{aligned} \quad (\text{A.38})$$

where we separated out the symmetric part of the adjoint indices. The quadratic casimir $C_{2,R}$ of a representation R is given by $C_{2,R} = J_R(J_R + 1)$.

A.3.1. Calculation of traces with four $\mathfrak{su}(n)$ generators

In this subsection we follow the strategy for calculating representation factors from traces over $\mathfrak{su}(n)$ generators presented in Ref. [37]. We denote the generators of a representation r of $SU(n)$ by t_r^a and the structure constants are given by $[t_r^a, t_r^b] = if^{abc}t_r^c$. The index of the representation r is defined with $\text{Tr}(t_r^a t_r^b) = T_r \delta^{ab}$. Our aim is a general decomposition of the trace $\text{Tr}(t_r^a t_r^b t_r^c t_r^d)$. We begin with the definition of a fully symmetrized product of n generators as

$$\{t_r^{a_1} t_r^{a_2} \dots t_r^{a_n}\} = \frac{1}{n!} \left(\sum_{\sigma \in \text{Per}(n)} t_r^{a_{\sigma(1)}} t_r^{a_{\sigma(2)}} \dots t_r^{a_{\sigma(n)}} \right). \quad (\text{A.39})$$

Using this symmetrised product we may write a symmetric trace of generators as

$$d_r^{a_1 \dots a_n} = \text{Tr}(t_r^{a_1} \{t_r^{a_2} \dots t_r^{a_n}\}). \quad (\text{A.40})$$

In a $\mathfrak{su}(n)$ algebra the $n-1$ smallest symmetric traces form independent structure constants in the adjoint space, e.g. in $\mathfrak{su}(3)$ there exists an independent symmetric structure constant d_r^{abc} . The Kronecker delta δ^{ab} in the adjoint space always belongs to this structure constants, as it follows from the (symmetric) trace of two generators. If the structure constant is not independent, it can either be decomposed into lower dimensional constants or it vanishes.

If we want to calculate the trace of four generators we need the symmetrised product of three generators given by

$$\{t_r^a t_r^b t_r^c\} = \frac{1}{6} (t_r^a t_r^b t_r^c + t_r^b t_r^c t_r^a + t_r^c t_r^a t_r^b + t_r^a t_r^c t_r^b + t_r^b t_r^a t_r^c + t_r^c t_r^b t_r^a). \quad (\text{A.41})$$

Now we start commuting each generator product on the right hand side of Eq. (A.41) such that we arrive at $t_r^a t_r^b t_r^c$ plus combinations of structure constants times products of two generators. Thus, we get

$$t_r^b t_r^a t_r^c = t_r^a t_r^b t_r^c + if^{ban} t_r^n t_r^c, \quad (\text{A.42a})$$

$$t_r^a t_r^c t_r^b = t_r^a t_r^b t_r^c + if^{cbn} t_r^n t_r^a, \quad (\text{A.42b})$$

$$t_r^b t_r^c t_r^a = t_r^a t_r^b t_r^c + if^{can} t_r^n t_r^b + if^{ban} t_r^n t_r^c, \quad (\text{A.42c})$$

$$t_r^c t_r^a t_r^b = t_r^a t_r^b t_r^c + if^{can} t_r^n t_r^a + if^{cbn} t_r^n t_r^b, \quad (\text{A.42d})$$

$$t_r^c t_r^b t_r^a = t_r^a t_r^b t_r^c + if^{ban} t_r^n t_r^c + if^{can} t_r^n t_r^a + if^{cbn} t_r^n t_r^b. \quad (\text{A.42e})$$

Inserting these relations in Eq. (A.41) results into

$$\{t_r^a t_r^b t_r^c\} = t_r^a t_r^b t_r^c + \frac{1}{6} \left(if^{ban} (\{t_r^n, t_r^c\} + t_r^n t_r^c) i + f^{can} (\{t_r^n, t_r^b\} + t_r^n t_r^b) + 3if^{cbn} t_r^n t_r^a \right). \quad (\text{A.43})$$

Now we can insert the relation in Eq. (A.43) into the trace we want to evaluate, namely $\text{Tr}(t_r^a t_r^b t_r^c t_r^d)$. We obtain

$$\begin{aligned} \text{Tr}(t_r^a t_r^b t_r^c t_r^d) &= \text{Tr}(\{t_r^a t_r^b t_r^c\} t_r^d) - \frac{i}{6} \left(f^{ban} \text{Tr}(\{t_r^n, t_r^c\} + t_r^n t_r^c) t_r^d \right. \\ &\quad \left. + f^{can} \text{Tr}(\{t_r^n, t_r^b\} + t_r^n t_r^b) t_r^d + 3i f^{cbn} \text{Tr}(t_r^a t_r^n t_r^d) \right) \\ &= d_r^{abcd} - \frac{i}{2} (d_r^{cdn} f^{ban} + d_r^{dan} f^{cbn} + d_r^{bdn} f^{can}) \\ &\quad + \frac{1}{12} \text{Tr}(f^{ban} f^{cdn} + 3f^{cbn} f^{dan} + f^{can} f^{bdn}), \end{aligned} \quad (\text{A.44})$$

where we used the short hand notation for the symmetric traces

$$d_r^{abcd} = \text{Tr}(\{t_r^a t_r^b t_r^c\} t_r^d), \quad (\text{A.45a})$$

$$d_r^{abc} = \frac{1}{2} \text{Tr}(\{t_r^a, t_r^b\} t_r^c). \quad (\text{A.45b})$$

With the use of the Jacobi identities of the structure constants

$$f^{abn} f^{cdn} + f^{bcn} f^{adn} + f^{can} f^{bdn} = 0, \quad (\text{A.46a})$$

$$d_r^{abn} f^{cdn} + d_r^{bcn} f^{adn} + d_r^{can} f^{bdn} = 0, \quad (\text{A.46b})$$

this results in the desired relation

$$\text{Tr}(t_r^a t_r^b t_r^c t_r^d) = d_r^{abcd} + \frac{i}{2} (d_r^{adn} f^{bcn} - d_r^{bcn} f^{adn}) + \frac{1}{6} \text{Tr}(f^{adn} f^{bcn} - f^{abn} f^{cdn}). \quad (\text{A.47})$$

A.4. Definitions for helicity eigenvectors

In this section, we provide more information about the construction of polarization vectors representing helicity eigenstates of external vector bosons. Massive vector bosons (with spin $s = 1$) have three degrees of freedom, which should also be represented in three independent polarization vectors for external bosons. Therefore, following the definition in Ref. [38], we choose for an on-shell vector boson with momentum $k = (E, k_x, k_y, k_z)$ the rectangular polarization basis

$$\epsilon(k, 1) = \frac{1}{|\vec{k}| \sqrt{k_x^2 + k_y^2}} \left(0, k_x k_z, k_y k_z, -k_x^2 - k_y^2 \right), \quad (\text{A.48a})$$

$$\epsilon(k, 2) = \frac{1}{\sqrt{k_x^2 + k_y^2}} \left(0, -k_y, k_x, 0 \right), \quad (\text{A.48b})$$

$$\epsilon(k, 3) = \frac{E}{m|\vec{k}|} \left(\frac{|\vec{k}|^2}{E}, k_x, k_y, k_z \right), \quad (\text{A.48c})$$

which is a valid choice for every Lorentz frame, as the conditions $k^\mu \epsilon_\mu(k, \lambda') = 0$ and $\epsilon^{*\mu}(k, \lambda') \epsilon_\mu(k, \lambda'') = -\delta_{\lambda' \lambda''}$ are ensured. The third polarization vector corresponds already to the longitudinal helicity eigenstate $\epsilon_0(k) = \epsilon(k, 3)$, as the spacial component is

aligned in the direction of spacial momenta. The transverse positive and negative helicity eigenvectors are constructed with

$$\epsilon_{\pm}(k) = \mp \frac{1}{\sqrt{2}} (\epsilon(k, 1) \pm i\epsilon(k, 2)) . \quad (\text{A.49})$$

In the COM frame for two antiparallel bosons with momenta in the xz -plane $k_1^\mu = \frac{\sqrt{s}}{2} (1, \beta \sin \theta, 0, \beta \cos \theta)$ and $k_2^\mu = \frac{\sqrt{s}}{2} (1, -\beta \sin \theta, 0, -\beta \cos \theta)$ for $\theta \in [0, \pi)$ we thus have

$$\begin{aligned} \epsilon(k_1, 1) &= (0, \cos \theta, 0, -\sin \theta) , & \epsilon(k_2, 1) &= (0, \cos \theta, 0, -\sin \theta) , \\ \epsilon(k_1, 2) &= (0, 0, 1, 0) , & \epsilon(k_2, 2) &= (0, 0, -1, 0) , \\ \epsilon(k_1, 3) &= \frac{\sqrt{s}}{2m_W} (\beta, \sin \theta, 0, \cos \theta) , & \epsilon(k_2, 3) &= \frac{\sqrt{s}}{2m_W} (\beta, -\sin \theta, 0, -\cos \theta) . \end{aligned} \quad (\text{A.50})$$

Now taking the momenta defined in Section 5.2, we find an ambiguity in the definition of the polarization vectors for the incoming momenta along the z -axis. We use for our calculation the convention

$$\epsilon(p_1, \lambda') = \lim_{\theta \rightarrow 0} \epsilon(k_1, \lambda') , \quad (\text{A.51a})$$

$$\epsilon(p_2, \lambda') = \lim_{\theta \rightarrow 0} \epsilon(k_2, \lambda') , \quad (\text{A.51b})$$

and finally get the full set of helicity eigenvectors:

$$\begin{aligned} \epsilon_{\pm}(p_1) &= -\frac{1}{\sqrt{2}} (0, 1, \pm i, 0) , & \epsilon_0(p_1) &= \frac{\sqrt{s}}{2m_W} (\beta, 0, 0, 1) , \\ \epsilon_{\pm}(p_2) &= -\frac{1}{\sqrt{2}} (0, 1, \mp i, 0) , & \epsilon_0(p_2) &= \frac{\sqrt{s}}{2m_W} (\beta, 0, 0, -1) , \\ \epsilon_{\pm}^*(q_1) &= -\frac{1}{\sqrt{2}} (0, \cos \theta, -\sin \theta \mp i, 0) , & \epsilon_0^*(q_1) &= \frac{\sqrt{s}}{2m_W} (\beta, \sin \theta, 0, \sin \theta) , \\ \epsilon_{\pm}^*(q_2) &= -\frac{1}{\sqrt{2}} (0, \cos \theta, -\sin \theta \pm i, 0) , & \epsilon_0^*(q_2) &= \frac{\sqrt{s}}{2m_W} (\beta, -\sin \theta, 0, -\cos \theta) . \end{aligned} \quad (\text{A.52})$$

Of course, as depicted here, we need to use the complex conjugate helicity eigenvectors for outgoing particles.

A.5. VeBoS program

VeBos is a program based on Fortran77 code that provides routines for different aspects of on-shell VBS, that were partly discussed in Chapter 5. The main program in VeBoS starts the input subroutine `slharun`³, basic variable declarations, the sub program `vebos_sub` that distributes the calculation and the output subroutine in `writeslha`. Depending on the settings, `vebos_sub` opens subroutines for constructing the differential cross section, the integrands for the projection of partial-wave (PW) coefficients as described in Eq. (3.37) (but

³The subroutines `slharun` and `writeslha` make use of the Robert Harlander's SLHARoutines for input and output, which is taken from Ref. [39].

without the normalization!) or directly the amplitude. Hereby, the calculation is always performed separately for the SM, the new-physics (NP) one-loop and/or EFT contribution. If an integration is needed, `vebos_sub` forwards the integrand to `integ_vebos`, where the VEGAS routine from the CUBA library [40] is used. The main work is included in the subroutines `calcampSM`, `calcampLoop` and `calcampEFT` that numerically construct the Feynman amplitudes.

The analytic one-loop vertex correction discussed in Section 4.1 are accessed in the subroutines `Prop1FeLoop`, `Tr1FeLoop` and `Box1FeLoop` for the fermion case and `Prop1ScLoop`, `Tr1ScLoop` and `Box1ScLoop` for the scalar case. The PV loop functions are evaluated with the help of `LoopTools` [17]. The expressions of the EFT vertices mentioned in Eqs. (3.22), (3.23) and (3.24) appear in `PropVertEff`, `TrVertEff` and `BoxVertEff`, respectively.

As it became clear, `VeBoS` needs to be linked to two external codes, the CUBA library and `LoopTools`.

A.5.1. Input settings

The input file, the default is called `vebos.in`, is separated into different blocks. The first number of each line is the variable identifier for the assignment and the second number is the given value. The text after the hashtag is only a comment for the variable identification of the user. We will go through the different blocks in the following and present an example setting.

The first block takes integer values and sets the general modus of the program. It has the following form:

```
Block INTEGER
 1  1    # XS
 2  0    # diff
 3  1    # varrep
 4  2    # eff
 5  2    # process
 6  0    # topology
 7  0    # Lexpand

 8  1    # nF
 9  1    # nS
10  1    # helI1
11  1    # helI2
12  1    # helF1
13  1    # helF2
```

The description of the variables is as follows:

XS 0: output in form of an amplitude/PW coefficient; 1: output in form of the (differential) cross section

diff 0: no angular integration, hence differential cross section or amplitude in the output;
1: angular integration is performed for total cross section or the PW coefficient output

varrep 0: calculation for fixed model parameters; 1: output values are different coefficients of powers of T_R and $T_R C_{2,R}$

eff 0: only loop calculation; 1: only EFT calculation; 2: both calculations

process 0: all VBS processes; 1-7: specific VBS assigned following Eq. (5.3)

topology 0: all diagrams; ± 1 : only/no propagator corrections (SM W -propagator diagram); ± 2 : only/no aTGC (SM Higgs-propagator diagram); ± 3 : only/no aQGC (SM $4W$ -vertex)

Lexpand 0: calculation of EFT expanded in g ; 1: calculation of EFT expanded in energy scale Λ (Up to now, combinations of Fe and Sc in one diagram are not accounted for!)

nF number of identical fermion multiplets (only if **varrep** = 0)

nS number of identical scalar multiplets (only if **varrep** = 0)

helI1/2 helicity of incoming vector boson 1/2

helF1/2 helicity of outgoing vector boson 1/2

Not all of the presented possible settings are compatible. The setting **varrep** = 1 forces a choice of **process** \neq 0 and also there is no possibility to calculate a (differential) cross section with **varrep** = 1 and **Lexpand** = 1.

The second input block takes the real values setting the NP model parameters and the physical environment. An example setting is shown in the following:

```

Block REAL
 1  2000.d0  # sqrt(s) [GeV]
 2   5.0d0  # angle [Degree]
 3   0.66d0  # g
 4  246.d0  # v [GeV]
 5  750.d0  # MF [GeV]
 6  750.d0  # MS [GeV]
 7  750.d0  # renscale
 8   5.d0  # jF
 9   8.d0  # jS
10   0.d0  # UVdiv

```

The variable **UVdiv**, which sets $\Delta = \frac{1}{\epsilon} - \gamma_E + \log(4\pi)$, can be taken nonzero if the cancellation of ultraviolet divergences should be checked. In that case, the EFT coefficient **fww** needs to be activated in the EFT calculation. Likewise, **renscale** sets the renormalization scale, which enters the EFT also in the **fww** coefficient, if the **renscale** value differs from the loop particle mass. **angle** sets the analyzed angle for the differential cross section

and the Feynman amplitude or the integration range for the cross section and the PW coefficient calculation.

The next block is only relevant if including an EFT calculation. Then it activates (value 1) or deactivates (value 0) specific Wilson coefficients and, hence, the contribution of the associated EFT operator.

```
Block WILSONCOEFF
 1  0  # activates fWW
 2  1  # activates fDW
 3  1  # activates fD2W
 4  1  # activates fWWW
 5  1  # activates fDWWW0
 6  1  # activates fDWWW1
 7  1  # activates fT0
 8  1  # activates fT1
 9  1  # activates fT2
10  1  # activates fT3
```

In the last block, some setting for the VEGAS integration can be changed. This is helpful for choosing the desired speed and accuracy of the integration.

```
Block VEGAS
 1  500  # nstart
 2  0    # nincrease
 3  500  # mineval
 4  2500 # maxeval
```

A.5.2. Output

The output file is structured in blocks like the input. The calculated values are presented in the blocks SM, LOOP and EFT. The size of the blocks varies depending on the input settings of VeBoS, but the comments after the hashtags are chosen, such that the output should be well understood by the user. For a crosscheck after the calculation, the output file also lists all input blocks.

In the subsequent lines, the beginning of an example output block will be shown:

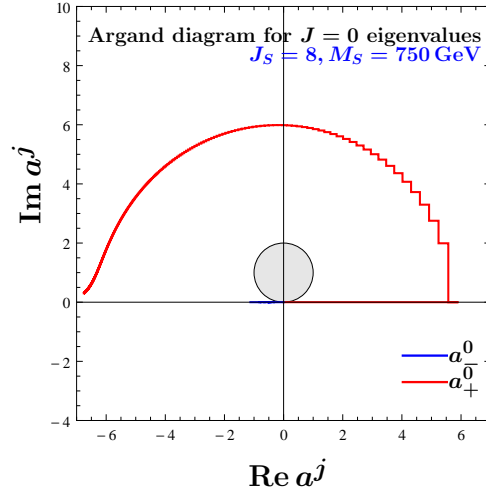
Block LOOP			
1	1.01613460E-02	# sigma(TF) [pb],	WpmWmp->ZZ
2	1.05764619E-04	# Error(TF) [pb],	WpmWmp->ZZ
3	3.07702393E-06	# sigma(CFTF) [pb],	WpmWmp->ZZ
4	3.14066510E-08	# Error(CFTF) [pb],	WpmWmp->ZZ
5	6.77915050E-07	# sigma(TF^2) [pb],	WpmWmp->ZZ
6	4.08536986E-09	# Error(TF^2) [pb],	WpmWmp->ZZ
7	4.11588966E-10	# sigma(CFTF^2) [pb],	WpmWmp->ZZ
8	2.53226248E-12	# Error(CFTF^2) [pb],	WpmWmp->ZZ
9	6.26962997E-14	# sigma(CF^2TF^2) [pb],	WpmWmp->ZZ
10	4.16989875E-16	# Error(CF^2TF^2) [pb],	WpmWmp->ZZ
⋮	⋮	⋮	⋮

Here, we used the input settings for calculating the cross section for the process $WW \rightarrow ZZ$ without specifying the model representation. Thus, in order to get the cross section, we have to multiply each value with the representation factor shown in the bracket and add up the contributions up to the order we want to consider (T_R corresponds to $O(g^6)$, and T_R^2 to $O(g^8)$). As we used numerical integration for the generation of those values, the error on each value estimated by VEGAS is presented.

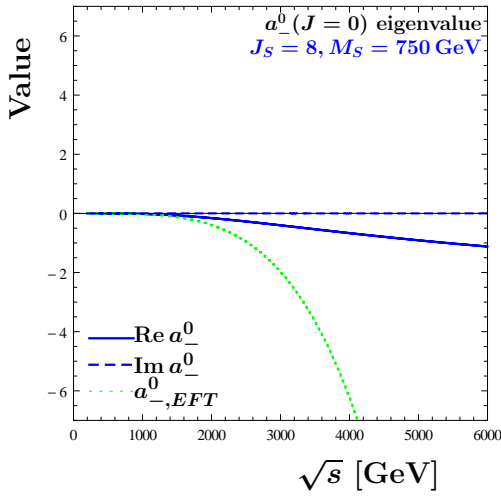
A.6. Partial-wave analysis of the concrete scalar model

In this section we demonstrate the partial-wave (PW) analysis of the model with one scalar multiplet with $J_S = 8$ and $M_S = 750$ GeV. The construction of the eigenvalues of the PW coefficients follows the procedure in Section 5.6.

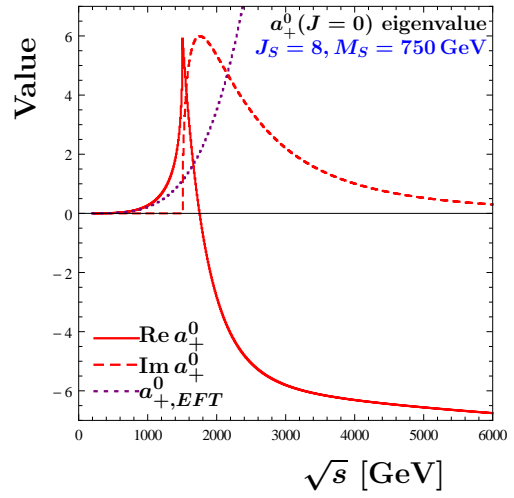
In Fig. A.1 we depict the dominant eigenvalue of the PW coefficients in the scalar case. We clearly see a large deviation from the unitarity bound of Eq. (3.40), which begins in the vicinity of the peak at $\sqrt{s} \sim 1500$ GeV. This behavior of the $a_+^0(J = 0)$ eigenvalue indicates, that the predictions of our scalar model at the one-loop level are beyond what is acceptable by unitarity considerations. This arises from the high representation of $J_S = 8$, as using a representation with $J_S = 6$ would result in a comparable situation to the fermion case. However, we need the large isospin to have a Wilson coefficient of O_{T_1} in the ballpark of experimental bounds[6]. Therefore, we continue using the scalar model with the given parameters in comparison with its derived EFT approximation and in contrast to the fermion model, keeping in mind that the predictions do not resemble a physical behavior.



(a)



(b)



(c)

Figure A.1.: Analysis of the isospin singlet PW coefficient eigenvalues a_{\pm}^0 ($J = 0$) in the scalar case. We show (a) the Argand diagram for both eigenvalues and the diagram showing the real part, imaginary part and the EFT eigenvalue (b) of a_{-}^0 ($J = 0$) and (c) of a_{+}^0 ($J = 0$) as a function of \sqrt{s} .

Bibliography

- [1] G. Aad et al. “Observation of a new particle in the search for the Standard Model Higgs boson with the ATLAS detector at the LHC”. In: *Physics Letters B* 716.1 (Sept. 2012), pp. 1–29. ISSN: 0370-2693. DOI: 10.1016/j.physletb.2012.08.020. URL: <http://dx.doi.org/10.1016/j.physletb.2012.08.020>.
- [2] S. Chatrchyan et al. “Observation of a new boson at a mass of 125 GeV with the CMS experiment at the LHC”. In: *Physics Letters B* 716.1 (Sept. 2012), pp. 30–61. ISSN: 0370-2693. DOI: 10.1016/j.physletb.2012.08.021. URL: <http://dx.doi.org/10.1016/j.physletb.2012.08.021>.
- [3] J. T. Boyd. “LHC Run-2 and Future Prospects”. In: *2019 European School of High-Energy Physics (ESHEP2019) Saint Petersburg, Russia, September 4-17, 2019*. 2020. arXiv: 2001.04370 [hep-ex].
- [4] Michael Rauch. *Vector-Boson Fusion and Vector-Boson Scattering*. 2016. arXiv: 1610.08420 [hep-ph].
- [5] Ballestrero Alessandro et al. “Vector boson scattering: Recent experimental and theory developments”. In: *Reviews in Physics* 3 (Nov. 2018), pp. 44–63. ISSN: 2405-4283. DOI: 10.1016/j.revip.2018.11.001. URL: <http://dx.doi.org/10.1016/j.revip.2018.11.001>.
- [6] A. M. Sirunyan et al. “Measurement of electroweak WZ boson production and search for new physics in WZ + two jets events in pp collisions at s=13TeV”. In: *Physics Letters B* 795 (Aug. 2019), pp. 281–307. ISSN: 0370-2693. DOI: 10.1016/j.physletb.2019.05.042. arXiv: 1901.04060 [hep-ex]. URL: <http://dx.doi.org/10.1016/j.physletb.2019.05.042>.
- [7] A. M. Sirunyan et al. “Measurement of vector boson scattering and constraints on anomalous quartic couplings from events with four leptons and two jets in proton–proton collisions at $\sqrt{s} = 13$ TeV”. In: *Phys. Lett.* B774 (2017), pp. 682–705. DOI: 10.1016/j.physletb.2017.10.020. arXiv: 1708.02812 [hep-ex].
- [8] K. Arnold et al. “Vbfnlo: A parton level Monte Carlo for processes with electroweak bosons”. In: *Computer Physics Communications* 180.9 (Sept. 2009), pp. 1661–1670. ISSN: 0010-4655. DOI: 10.1016/j.cpc.2009.03.006. URL: <http://dx.doi.org/10.1016/j.cpc.2009.03.006>.
- [9] J. Baglio et al. *VBFNLO: A parton level Monte Carlo for processes with electroweak bosons – Manual for Version 2.7.0*. 2011. arXiv: 1107.4038 [hep-ph].
- [10] J. Baglio et al. *Release Note - VBFNLO 2.7.0*. 2014. arXiv: 1404.3940 [hep-ph].

- [11] M. E. Peskin and D. V. Schroeder. *An Introduction to quantum field theory*. Reading, USA: Addison-Wesley, 1995. ISBN: 9780201503975, 0201503972. URL: <http://www.slac.stanford.edu/~mpeskin/QFT.html>.
- [12] M. D. Schwartz. *Quantum Field Theory and the Standard Model*. Cambridge University Press, 2014. ISBN: 1107034736, 9781107034730. URL: <http://www.cambridge.org/us/academic/subjects/physics/theoretical-physics-and-mathematical-physics/quantum-field-theory-and-standard-model>.
- [13] E. Byckling and K. Kajantie. *Particle Kinematics*. Jyvaskyla, Finland: University of Jyvaskyla, 1971. URL: [http://lss.fnal.gov/archive/other/Part.Kinematics-\(ChaptersI-VI,X\).pdf](http://lss.fnal.gov/archive/other/Part.Kinematics-(ChaptersI-VI,X).pdf).
- [14] J. P. Ellis. “TikZ-Feynman: Feynman diagrams with TikZ”. In: *Computer Physics Communications* 210 (Jan. 2017), pp. 103–123. ISSN: 0010-4655. DOI: 10.1016/j.cpc.2016.08.019. URL: <http://dx.doi.org/10.1016/j.cpc.2016.08.019>.
- [15] G. 't Hooft and M. Veltman. “Scalar one-loop integrals”. In: *Nuclear Physics B* 153 (1979), pp. 365–401. ISSN: 0550-3213. DOI: [https://doi.org/10.1016/0550-3213\(79\)90605-9](https://doi.org/10.1016/0550-3213(79)90605-9). URL: <http://www.sciencedirect.com/science/article/pii/0550321379906059>.
- [16] G. Passarino and M. Veltman. “One-loop corrections for e^+e^- annihilation into $\mu^+\mu^-$ in the Weinberg model”. In: *Nuclear Physics B* 160.1 (1979), pp. 151–207. ISSN: 0550-3213. DOI: [https://doi.org/10.1016/0550-3213\(79\)90234-7](https://doi.org/10.1016/0550-3213(79)90234-7). URL: <http://www.sciencedirect.com/science/article/pii/0550321379902347>.
- [17] T. Hahn and M. Pérez-Victoria. “Automated one-loop calculations in four and D dimensions”. In: *Computer Physics Communications* 118.2 (1999), pp. 153–165. ISSN: 0010-4655. DOI: [https://doi.org/10.1016/S0010-4655\(98\)00173-8](https://doi.org/10.1016/S0010-4655(98)00173-8). URL: <http://www.sciencedirect.com/science/article/pii/S0010465598001738>.
- [18] G. Perez, M. Sekulla, and D. Zeppenfeld. “Anomalous quartic gauge couplings and unitarization for the vector boson scattering process $pp \rightarrow W^+W^+jjX \rightarrow \ell^+v_\ell\ell^+v_\ell jjX$ ”. In: *The European Physical Journal C* 78.9 (Sept. 2018). ISSN: 1434-6052. DOI: 10.1140/epjc/s10052-018-6230-1. URL: <http://dx.doi.org/10.1140/epjc/s10052-018-6230-1>.
- [19] M. B. Einhorn and J. Wudka. “The bases of effective field theories”. In: *Nuclear Physics B* 876.2 (Nov. 2013), pp. 556–574. ISSN: 0550-3213. DOI: 10.1016/j.nuclphysb.2013.08.023. URL: <http://dx.doi.org/10.1016/j.nuclphysb.2013.08.023>.
- [20] K. Hagiwara et al. “Low-energy effects of new interactions in the electroweak boson sector”. In: *Phys. Rev. D* 48 (1993), pp. 2182–2203. DOI: 10.1103/PhysRevD.48.2182.
- [21] O. J. P. Éboli, M. C. Gonzalez-Garcia, and J. K. Mizukoshi. “ $pp \rightarrow jje^\pm\mu^\pm\nu\nu$ and $jje^\pm\mu^\mp\nu\nu$ at $O(\alpha_{\text{em}}^6)$ and $O(\alpha_{\text{em}}^4\alpha_s^2)$ for the study of the quartic electroweak gauge boson vertex at CERN LHC”. In: *Phys. Rev. D* 74 (7 Oct. 2006), p. 073005. DOI: 10.1103/PhysRevD.74.073005. URL: <https://link.aps.org/doi/10.1103/PhysRevD.74.073005>.

- [22] O. J. P. Éboli and M. C. Gonzalez–Garcia. “Classifying the bosonic quartic couplings”. In: *Physical Review D* 93.9 (May 2016). ISSN: 2470-0029. DOI: 10.1103/PhysRevD.93.093013. URL: <http://dx.doi.org/10.1103/PhysRevD.93.093013>.
- [23] M. Tanabashi et al. “Review of Particle Physics”. In: *Phys. Rev. D* 98 (3 Aug. 2018), p. 030001. DOI: 10.1103/PhysRevD.98.030001. URL: <https://link.aps.org/doi/10.1103/PhysRevD.98.030001>.
- [24] R. Mertig, M. Böhm, and A. Denner. “Feyn Calc - Computer-algebraic calculation of Feynman amplitudes”. In: *Computer Physics Communications* 64.3 (1991), pp. 345–359. ISSN: 0010-4655. DOI: [https://doi.org/10.1016/0010-4655\(91\)90130-D](https://doi.org/10.1016/0010-4655(91)90130-D). URL: <http://www.sciencedirect.com/science/article/pii/001046559190130D>.
- [25] V. Shtabovenko, R. Mertig, and F. Orellana. “New developments in FeynCalc 9.0”. In: *Computer Physics Communications* 207 (2016), pp. 432–444. ISSN: 0010-4655. DOI: <https://doi.org/10.1016/j.cpc.2016.06.008>. URL: <http://www.sciencedirect.com/science/article/pii/S0010465516301709>.
- [26] V. Shtabovenko, R. Mertig, and F. Orellana. *FeynCalc 9.3: New features and improvements*. 2020. arXiv: 2001.04407 [hep-ph].
- [27] C. Itzykson and J. B. Zuber. *Quantum Field Theory*. International Series In Pure and Applied Physics. New York: McGraw-Hill, 1980. ISBN: 9780486445687, 0486445682. URL: <http://dx.doi.org/10.1063/1.2916419>.
- [28] B. W. Lee, C. Quigg, and H. B. Thacker. “Weak Interactions at Very High-Energies: The Role of the Higgs Boson Mass”. In: *Phys. Rev. D* 16 (1977), p. 1519. DOI: 10.1103/PhysRevD.16.1519.
- [29] W. Kilian et al. “High-Energy Vector Boson Scattering after the Higgs Discovery”. In: *Phys. Rev. D* 91 (2015), p. 096007. DOI: 10.1103/PhysRevD.91.096007. arXiv: 1408.6207 [hep-ph].
- [30] W. Heisenberg and H. Euler. “Folgerungen aus der Diracschen Theorie des Positrons”. In: *Zeitschrift für Physik* 98.11-12 (Nov. 1936), pp. 714–732. DOI: 10.1007/BF01343663.
- [31] T. Plehn. “Lectures on LHC Physics”. In: *Lecture Notes in Physics* (2012). ISSN: 1616-6361. DOI: 10.1007/978-3-642-24040-9. URL: <http://dx.doi.org/10.1007/978-3-642-24040-9>.
- [32] Albert M Sirunyan et al. “Search for anomalous triple gauge couplings in WW and WZ production in lepton + jet events in proton-proton collisions at $\sqrt{s} = 13$ TeV”. In: *JHEP* 12 (2019), p. 062. DOI: 10.1007/JHEP12(2019)062. arXiv: 1907.08354 [hep-ex].
- [33] M. Löschner. “Unitarisation of Anomalous Couplings in Vector Boson Scattering”. MA thesis. Institute for Theoretical Physics, KIT, Nov. 2014. URL: https://www.itp.kit.edu/prep/diploma/PSFiles/Master_Max.pdf (visited on 03/04/2020).
- [34] L. A. Harland-Lang et al. “Parton distributions in the LHC era: MMHT 2014 PDFs”. In: *Eur. Phys. J. C* 75.5 (2015), p. 204. DOI: 10.1140/epjc/s10052-015-3397-6. arXiv: 1412.3989 [hep-ph].

- [35] A. Buckley et al. “LHAPDF6: parton density access in the LHC precision era”. In: *Eur. Phys. J. C* 75 (2015), p. 132. DOI: 10.1140/epjc/s10052-015-3318-8. arXiv: 1412.7420 [hep-ph].
- [36] J. C. Romão. *Modern Techniques for One-Loop Calculations*. 2019. URL: <https://porthos.tecnico.ulisboa.pt/OneLoop/one-loop.pdf> (visited on 03/04/2020).
- [37] T. van Ritbergen, A. N. Schellekens, and J. A. M. Vermaseren. “Group theory factors for Feynman diagrams”. In: *International Journal of Modern Physics A* 14.01 (Jan. 1999), pp. 41–96. ISSN: 1793-656X. DOI: 10.1142/S0217751X99000038. arXiv: hep-ph/9802376 [hep-ph]. URL: <http://dx.doi.org/10.1142/S0217751X99000038>.
- [38] K. Hagiwara and D. Zeppenfeld. “Amplitudes for multi-parton processes involving a current at e^+e^- , $e^\pm p$, and hadron colliders”. In: *Nuclear Physics B* 313.3 (1989), pp. 560–594. ISSN: 0550-3213. DOI: [https://doi.org/10.1016/0550-3213\(89\)90397-0](https://doi.org/10.1016/0550-3213(89)90397-0). URL: <http://www.sciencedirect.com/science/article/pii/0550321389903970>.
- [39] R. Harlander. *SLHARoutines*. 2013. URL: <https://web.physik.rwth-aachen.de/~harlander/software/slharoutines/> (visited on 03/02/2020).
- [40] T. Hahn. “Cuba—a library for multidimensional numerical integration”. In: *Computer Physics Communications* 168.2 (June 2005), pp. 78–95. ISSN: 0010-4655. DOI: 10.1016/j.cpc.2005.01.010. URL: <http://dx.doi.org/10.1016/j.cpc.2005.01.010>.

Acknowledgements

I would like to thank Prof. Dr. Dieter Zeppenfeld for giving me the opportunity to work on this exciting topic of theoretical particle physics and to take part in the scientific progress of his group. I am particularly grateful for his great supervision and for all the time he invested in the fruitful discussions we had.

My special thanks goes to Dr. Stefan Liebler, who has given me the best support throughout the time at the institute. I very much appreciate his advice, and his help in setting up the `VeBoS` code, in finding bugs and in providing the numerical results of the `VBFNLO` runs. I also wish to acknowledge his thorough proofreading of the thesis.

Moreover, I want to thank Heiko Schäfer-Siebert for providing the routines for the unitarization in `VBFNLO`, for giving me the necessary introduction into the relevant parts of the code, and for sharing his helpful ideas.

Last but not least, I want to express my gratitude to Prof. Dr. Milada M. Mühlleitner for accepting the job of being the second reviewer.